An Experimental and Numerical Investigation of Swirling Flows in a Rectangular Nozzle

Thesis by

Thomas Henry Sobota

In Partial Fulfillment of the Requirements

for the Degree of

Doctor of Philosophy

California Institute of Technology

Pasadena, California

1987

(Submitted April 10, 1987)

Acknowledgements

I would like to thank my advisor, Professor Frank E. Marble, for his continued support and encouragement through the years.

Many discussions with Dr. Harry F. Robey and Mr. Cliff Frieler were extremely helpful and stimulating and are greatly appreciated.

The support and advice from Dr. Dochan Kwak of the NASA-Ames Research center is greatly appreciated as is the assistance from Mr. Stuart Rogers.

Abstract

The high thrust to weight ratios now possible for military aircraft have made thrust vector pitch control more attractive and versatile than aerodynamic surface pitch control. Use of a rectangular nozzle is a natural consequence because articulation and sealing problems are less formidable than for conventional circular nozzles. The rectangular nozzle offers the additional possibility that the exhaust may mix rapidly with the ambient air and thereby reduce the radiative signature of the exhaust. Some previous investigations have suggested that a series of axial vortices may form in the nozzle, as a result of residual swirl from the gas turbine exhaust, and further enhance the mixing rate.

A detailed experimental investigation is described in this thesis which demonstrates that the formation of axial vortices in the nozzle is dependant on the vorticity distribution at the turbine exhaust. Further, three mechanisms which provide for the formation of axial vortices are identified.

A parallel computational investigation was carried out which not only confirmed the relationship between the turbine exhaust vorticity and the vortex patterns formed in the nozzle but also provided details of the flow field between the turbine discharge and the nozzle exit. On the basis of this more detailed understanding, it is now possible to "tailor" the vortex distribution at the nozzle exit by design of the turbine discharge and the intervening passage.

Table of Contents

List of Figures

Chapter 1

Introduction

Recent interest in the use of rectangular nozzles for aircraft application is the primary motivation for this investigation. The next generation of fighter aircraft will require increased maneuverability and STOL (short takeoff and landing) capability. One method for effecting this is through the use of vectored thrust. The rectangular nozzle provides a simple means to vector the thrust about a single axis. The rectangular geometry is being explored as a possibility for aircraft application because vectoring can be accomplished through the use of a relatively simple nozzle design that can also accommodate a variable area ratio convergent–divergent design if such a feature is desired. Figure 1.1, which first appeared in Reference [1], is a schematic representation for such a nozzle design in various modes of operation.

Consideration of the thermal characteristics of the exhaust plume is an important aspect of aircraft engine nozzle design. The vulnerability of the aircraft to detection by devices that are sensitive to infrared radiation is directly related to the temperature and extent of the aircraft exhaust plume. In addition to the capability of thrust vectoring, the rectangular nozzle has the second advantage of a reduced infrared radiation signature. The rectangular geometry of the resulting free jet enhances mixing between the jet fluid and the surrounding ambient fluid.

This enhanced mixing serves to dilute the hot combustion products in the exhaust plume with the cold surrounding air. The result is a shorter, cooler exhaust plume.

1.1 Technical Problems

The interest in the use of rectangular nozzles for aircraft application presents some interesting technical problems. The performance of the nozzle must be characterized in terms of nozzle efficiency, exhaust plume characteristics, and the effectiveness of the thrust vectoring.

The change from a round to rectangular nozzle introduces one more space variable. The flowfields associated with round nozzles are generally considered to be axi–symmetric and therefore two–dimensional in nature. The flowfield created in the rectangular nozzle is fully three–dimensional. Residual swirl from the turbomachinery in the aircraft engine serves to further complicate the problem. The swirl strength is measured as the angle between the axial and tangential components of the fluid velocity. In the region immediately behind the last turbine stage of an aircraft engine the residual swirl strength is commonly as high as fifteen degrees. As mentioned earlier, the rectangular nozzle design has beneficial effects on the near–field mixing between the exhaust plume and the surrounding fluid. The effect of this swirl and the resulting distribution of vorticity at the exit on the mixing has yet to be examined in detail. In the thrust–vectoring case, the effect of swirl on the resulting thrust vector is also a question of interest. Because the distribution of vorticity and pattern of streamwise vortices at the exit will vary greatly with different distributions of velocity at the exit of the engine turbine, there is a need to examine the development of the flowfield within

the nozzle for different inlet conditions.

1.2 Previous Work

Previous work in the area of rectangular nozzles and jets can be divided into two categories. The first category involves the design and testing of systems that are directly applicable to flight hardware. The second category involves investigations that are more basic in nature and that examine some aspect of the overall problem. The following, while not an exhaustive review of literature pertaining to rectangular nozzles, provides an idea of the nature of previous investigations and their relation to the current work and indicates the current state of research and development in this area.

In the first category there is much published work regarding the use of rectangular exhaust nozzles for aircraft application. There are at least two current projects aimed toward the development of flight hardware. The General Electric Company is involved with the design and development of the Augmented Deflector Exhaust Nozzle (ADEN), which is a rectangular vectoring nozzle with a thrust-vectoring flap deflection range of 10 degrees up to 20 degrees down. Reference [2] is a study of the feasibility of incorporating the ADEN system design on a YF-17 fighter. This reference covers, in detail, the ADEN system configuration and performance as well as the modifications to the airframe and flight control systems required to make the overall system operable. Later work by Wooten et al. [3] includes the testing of flight weight ADEN system hardware. Separately, the Pratt and Whitney Aircraft Engine Company has developed a rectangular vectoring nozzle with a thrust deflection range of 20 degrees in both directions. Reference [1] details the static testing of this configuration. The Pratt and Whitney nozzle

design is scheduled to be incorporated on an F–15 aircraft to produce a highly maneuverable STOL version of the F–15 as a technology demonstrator.

The second category involves investigations into more basic problems and details pertaining to rectangular nozzles. For the most part, these investigations pertain to the flowfield in the mixing region behind the nozzle. Relatively little work related to the nature of the flowfield within the nozzle has been performed.

Sforfa et al. [4] and Sforza and Stasi [5] characterized the mixing field of turbulent rectangular jets into three distinct regions. Near the jet exit is the potential core region characterized by little or no decay of the excess in velocity or temperature along the jet centerline. This is a wedge–shaped region immediately behind the jet exit. The potential core region ends where the two shear layers, which form along the wide edges of the jet, meet. The second region is called the region of characteristic decay because the decay of velocity and temperature along the jet centerline is dependent upon the nozzle geometry or characteristics. The third region is the region of axi–symmetric decay, where the jet characteristics are independent of initial geometry and assume characteristics of the farfield decay of axi–symmetric jets.

Decher [6] developed a simplified model to determine the effects of aspect ratio on the infrared emissions from heated rectangular jets. Emitted radiation from gases is strongly temperature–dependent and is often modeled as being proportional to T^n, where T is the gas temperature and the exponent n has a value in the range of 4 to 5. Because of this strong temperature dependence, the potential core region of the jet contributes most significantly to the thermal emissions from the exhaust plume. Decher's model predicts that the intensity of the emissions from the plume is dependent upon the orientation from which the

plume is viewed. He found a large decrease in the emitted radiation of the plume when viewed from the broad side and only a small increase in emitted radiation when the plume is viewed from the narrow side. In both of these investigations no account was made for the effect of swirl and the resulting axial vorticity in the flow.

Chu et al. [7] undertook an investigation to determine the effect of swirl on the potential core in rectangular ejector nozzles. His water–tunnel tests indicate a dramatic decrease in the length of the potential core region with only small amounts of swirl. A swirl strength of 7.5 degrees reduced the length of the potential core region by a factor of two over the length of the potential core with no swirl. A swirl strength of 22.5 degrees further reduced the length of the potential core by a factor of three over the no–swirl case. No effort was made to determine the detail of the flowfield due to swirl at the exit of the rectangular nozzle.

In a water channel flow visualization experiment, Der et al. [8] characterized the evolution of the swirling flow as it passed through a transition section that had a round inlet cross section and a rectangular exit cross section. There was no net change in the cross–sectional area from inlet to exit in the transition section used but it appears as though no effort was made to keep the cross–sectional area constant along the length of the transition section. The swirl was effected by the use of a pinwheel fixed at the inlet to the transition section. This was the first attempt to determine, in any detail, the secondary flow patterns at the nozzle exit due to swirl. Figure 1.2, which appeared in Reference [8], is a sketch of the vortex structure near the exit of a four–to–one aspect ratio nozzle. The apparent splitting of the main swirl into two co–rotating vortices is the most predominant

feature of this flowfield. Additionally, there are two smaller vortices of opposite sense to the main swirl, which form in diagonally opposed corners of the rectangular cross section. These are the result of the separation of the boundary layer, which forms on the wall into the main stream. It should be emphasized here that these observations are the result of dye streak flow visualization in water, using a simple water channel model. The investigators had difficulty in observing the flow patterns because of "large turbulent eddies in the nozzle." Chu et al. [9] [10] attempted to use the results of this investigation to model the infrared signature from a rectangular nozzle, taking into account the effects of swirl in the flowfield. Their findings indicate that while the effect of swirl increases mixing only slightly in the axi–symmetric case, the effect of swirl in lowering the plume temperature for a rectangular nozzle is dramatic. Their findings also prompted them to state that, despite the fact that the original intent of the use of rectangular nozzles was for increased aircraft performance, the enhanced mixing and subsequent reduction in infrared signature speak favorably, alone, for the use of rectangular nozzles in aircraft application.

1.3 Current Investigation

A knowledge of the development of the flowfield within the annular to rectangular transition section as well as the details of the flowfield at the exit would be extremely useful as an aid in designing and predicting the performance of rectangular nozzles. It is postulated that the distribution of axial or streamwise vorticity at the inlet to the transition section will influence, to a large degree, the distribution of vorticity and the formation of streamwise vortex patterns at the exit. This distribution of vortex patterns will significantly affect the nozzle

performance as well as the near–field mixing of the exhaust plume. It is therefore the goal of this investigation to determine which features of the inlet vorticity distribution are important in establishing vortex patterns at the exit as well as to examine the evolution of the flowfield as it passes through the transition section. The study of the development of the flowfield will enhance our understanding of the mechanisms by which the vorticity at the inlet is formed into the resulting flow patterns at the exit.

In an attempt to isolate the fluid dynamic phenomena that are important in the development of these flowfields, a controlled investigation was undertaken. A flow configuration that contained the basic characteristics of the original problem was used. These characteristics include an annular inlet cross section, a rectangular exit cross section and a net reduction in the cross–sectional area between the two cross sections. Eliminated from the problem were any features that would serve to unnecessarily complicate the flowfield or make measurement within the flowfield difficult. Features eliminated include any abrupt changes in the cross–sectional area or shape, the flow of hot gases and temperature variation due to combustion, and the effects of compressibility.

The resulting configuration was a low–speed, cold–flow test facility with a smooth variation in shape and cross–sectional area from the inlet to the exit of the transition section. The study of the flow in this facility was conducted in two parts.

For the experimental part of this investigation, a flow facility as described above was constructed. A hot–wire anemometry technique was used to measure the three components of the velocity vector on a rectangular mesh at the exit plane for various inlet conditions. The resulting maps of the exit velocity distribution

were used to determine the vortex patterns established at the exit plane.

Because measurement of the three components of the velocity within the duct would be a difficult and tedious task, an alternate method was desired to determine the development of the flowfield within the duct. Secondary flow analysis is typically used in the determination of cross–flow velocity patterns in situations where vorticity, important in establishing these flowfields, is convected through a three–dimensional flow section. Horlock and Lakshminarayana [11] provide a review of the current state of development of secondary flow analyis. A secondary flow is most often considered to be a cross–flow established by the twisting and stretching of vortex filaments that are initially normal to the primary flow direction. The primary flowfield is assumed to distort these vortex filaments as they are convected along. In the classical sense, the secondary flow approximation can be used when these vortex filaments are of small or infinitesimal strength, and therefore their effect on the primary flowfield can be considered negligible. Squire and Winter [12] as well as Hawthorne [13] provide a mathematical justification for this approximation and Lighthill [14] provides us with a clear physical explanation of this phenomenon. The real value, perhaps, of the secondary flow approximation is not to provide an accurate detailed representation of any given flowfield but to enable us, through the consideration of weak vortex filaments distributed within a flow, to qualitatively predict or physically explain the secondary flow patterns produced in any flow system. If this is the intent of the consideration of secondary flows, then it is often possible to relax the constraints that the secondary vorticity be infinitesimal and initially normal to the primary flow direction. Because the vorticity in swirling flows has a large streamwise component, the consideration of secondary flows in the classical sense will be useful

only as an aid in understanding, in a qualitative sense, certain aspects of the flowfield encountered.

With the usefulness of a secondary flow analysis as a tool to study the development of the flowfield eliminated, there is little other choice than to solve the equations of motion for the entire flowfield within the nozzle. This, of course, must be done numerically with the aid of a computer. Such analysis allows us a knowledge of the flow variables at many points within the nozzle and allows us to follow the development of the flowfield. Therefore, the second part of this investigation entails a detailed modeling of the flow configuration chosen for the experimental investigation. This modeling was performed using a three–dimensional incompressible laminar Navier–Stokes solver. The resulting information was displayed and analyzed through the use of velocity vector plots, vorticity contour maps, pressure contour maps, and streamline diagrams.

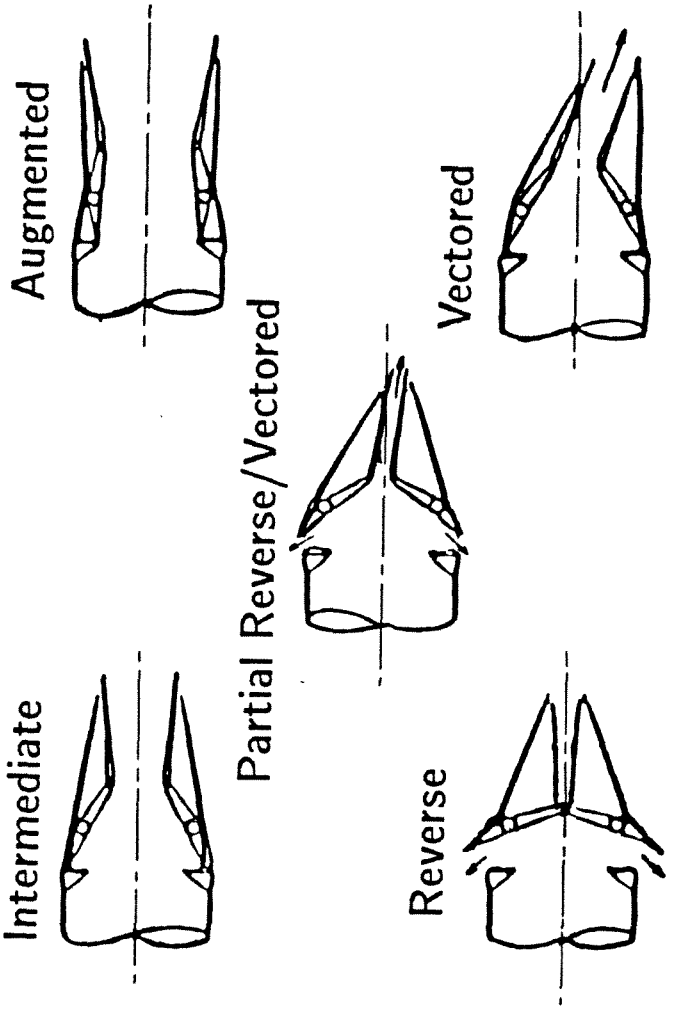

Figure 1.1: Diagram of Thrust–Vectoring Mechanism

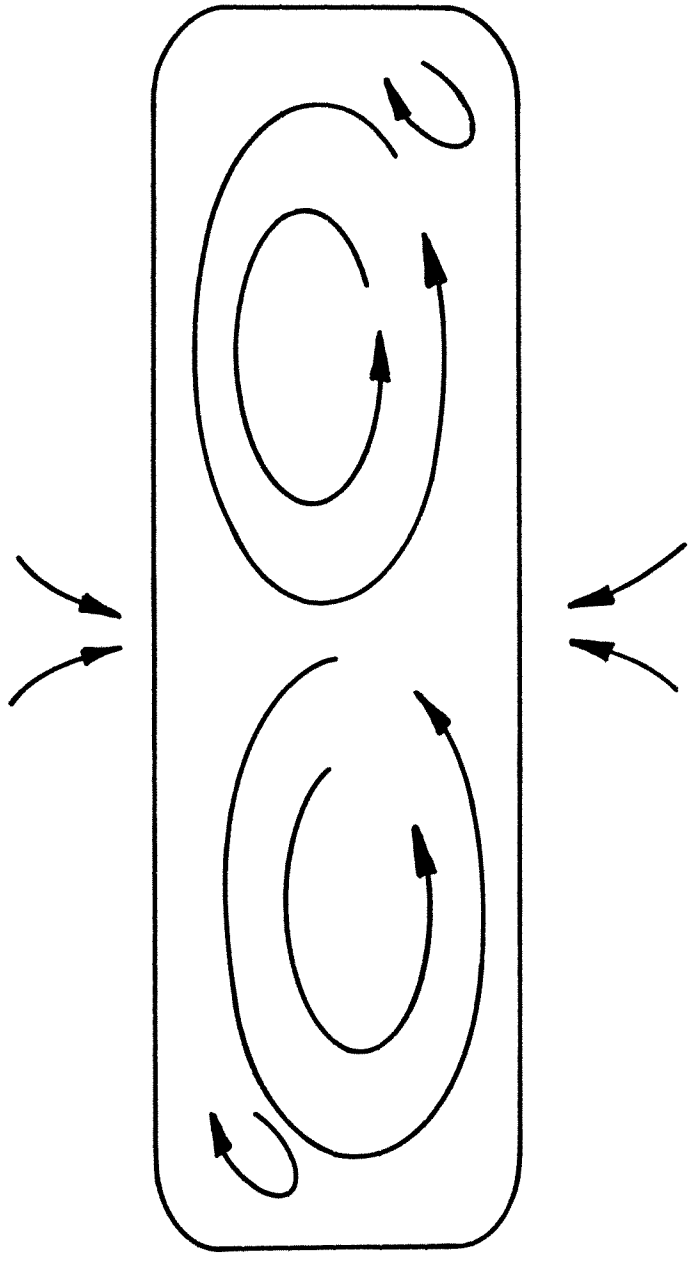

Figure 1.2: Vortex Pattern at Exit Due to Der

Chapter 2

Experimental Apparatus

The experimental phase of this investigation required the design and construction of a special facility. For the purpose of description, the components of the facility can be organized into two distinct categories. The first category, the flow system, consists of the equipment used to create the flowfield of interest. The second category, the instrumentation, consists of the probes, electronics, and the equipment used to position the probes in the flowfield so that the desired measurements could be made.

2.1 The Flow System

The experimental investigation of swirling flows in a rectangular nozzle required the construction of a nozzle with a transition from an annular to a rectangular cross section as well as the equipment necessary to provide a smooth flow of air through the nozzle. The flow system can be divided into four primary parts as follows:

1. Blower
2. Settling Chamber
3. Turning Vane Assembly

4. Contraction Section.

Figure 2.1 shows a schematic diagram of this system.

Blower

The blower used was a centrifugal blower of the backward curved blade type. It was powered by a 1.5 Hp 120 volt direct–current electric motor. Initially the motor speed was controlled with a solid–state motor controller. This controller, however, by nature of its design emitted large amounts of electromagnetic interference, which caused difficulty with the instrumentation. It was abandoned in favor of a simple variable transformer–bridge rectifier circuit. The blower was connected to the settling chamber by an eight–inch diameter flexible ventilation duct.

Settling Chamber

The settling chamber was constructed of three sections of large aluminum tubing. It was 18 inches in diameter and 48 inches in length. It contained fine mesh screens and aluminum honeycomb used to straighten and smooth the flow. On the downstream end of the settling chamber was a large flange to which the nozzle and the turning vane assembly were clamped.

Turning Vane Assembly

The purpose of the turning vane assembly was twofold. Primarily, it was used to impart a swirl on the flow. It was also used to support the centerbody. The blades were flat plate airfoils constructed of 22 gauge sheet metal with pivots attached at the quarter chord points at the root and tip of the blades. The pivots of the eighteen blades were clamped between two wooden rings at the tip and two wooden discs at the root. This arrangement permitted adjustment of the blade

angle from 0 degrees (no swirl) to 30 degrees. The solidity of the blades was 1.3 at the blade root and .8 at the blade tip. A second set of blades was constructed and was very similar in design to the first, except that the blades were separated at midspan in such a way that the blade angle for the inner half and outer half of the inlet annulus could be set independently.

Contraction Section

The contraction section (nozzle) consisted of two parts, the outer nozzle wall and the centerbody. The outer nozzle wall was made of fiberglass hand–laid on a wooden form. The upstream end of the Styrofoam centerbody was hemispherical and the downstream end an ellipsoid of revolution. The two ends were joined by a straight cylindrical section. The contraction section had an area ratio of 3.6 to 1. The aspect ratio of the rectangular exit was 5 to 1.

The nozzle (Figure 2.2) in combination with the centerbody was designed to have a smooth monotonically decreasing cross–sectional area. The cross sections of the nozzle are elliptical until the station where the nozzle is gradually faired from an elliptical to a rectangular cross section. This was done by first choosing the total cross–sectional area of the nozzle centerbody combination to be a smoothly varying function of axial location with zero slope near the inlet and outlet.

$$area_{total}(in^2) = \begin{cases} 159.50 & 0 < x < 6 \\ 57.25 \cos \pi \frac{x-6}{30} + 45 & 6 \leq x < 36 \\ 45 & 36 \leq x < 42 \end{cases}$$

Next, the shape of the centerbody was chosen to be an ellipsoid of revolution defined by;

$$radius_{centerbody}(in) = \begin{cases} 5.5 & 0 < x < 6 \\ 5.5\sqrt{1 - (\frac{x-6}{12})^2} & 6 \leq x < 18 \\ 0 & 18 \leq x < 42. \end{cases}$$

Finally, the length of the major axis of the elliptical cross section was defined by;

$$Y_{max}(in) = \begin{cases} 18 & 0 < x < 6 \\ 1.5(\cos \pi \frac{x-6}{30} + 1) + 15 & 6 \leq x < 36 \\ 15 & 36 \leq x < 42. \end{cases} \quad (2.1)$$

The length of the minor axis is then computed using the relation;

$$area_{total} - area_{centerbody} = area_{outerboundary} \quad (2.2)$$

The cross section of the outer boundary is elliptical from $x = 0$ to $x = 23.39in$ with the major axis defined by Y_{max} and the minor axis defined so that the area requirements are met.

The cross section at which $x = 23.39in$ is the last station into which a rectangle of the dimension of the desired exit cross section could be inscribed. From this station on, further reduction in area is accomplished by removing areas at the top, bottom and sides of the elliptical section as depicted in (Figure 2.3) where Y_{max} is given by Equation 2.1 and Z_{max} is still computed from Equation 2.2. The overall length of the nozzle is 42 inches. The first six inches at the inlet and the final six inches at the exit are of constant cross–sectional area.

2.2 Instrumentation

The object of the experimental phase of this investigation was to determine the three–dimensional velocity field at the rectangular exit of the contraction section

for varied inlet conditions. To characterize the velocity field, a large number of velocity measurements were taken by traversing a probe in the Y and Z directions at the exit plane. This, in order to get reliable data, was a very time–consuming process. The instrumentation and control system used in this effort can be organized into six primary subsystems as follows:

1. Micro–computer
2. Data Acquistion and Control Circuit
3. Traverse
4. Cross–wire Probe and Probe Holder
5. Hot–wire Anemometer System
6. Pitot Probe and Pressure Instrumentation.

Figure 2.4 shows a block diagram of this system.

Micro–Computer

An IBM PC compatible Compaq Deskpro micro–computer was used for data acquisition, control of the experiment, and data reduction. Peripheral devices used with the computer consisted of an 80 character–per–second dot impact printer and a Hewlett Packard 7470 two–pen digital plotter.

Data Acquisition and Control Circuit

A data acquisition and control circuit was designed and built for these experiments. The circuit consisted of two circuit cards. The main card (Figure 2.5) plugged directly into the IBM PC bus and contained the control logic as well as the timing circuitry. The circuit was constructed on an IBM PC prototype development board. The secondary card (Figure 2.6) was mounted in an enclosure separate from the main computer enclosure and was connected to the main

card via a ribbon cable. The secondary card contained an Analog Devices model AD 572 analog–to–digital converter. It had 12 bit resolution and by use of an Intel 8254 programmable timer could be programmed to sample at any rate up to 30,000 samples per second. The sixteen channels were time multiplexed into the AD572 with a CD4067 analog multiplexer. The control logic permitted the selection of channels from which to sample. Thus, through software, the user could select to sample from any single channel or to sample from any number of sequential channels starting with channel 0. The maximum sampling rate of 30,000 samples per second of the AD572 could be achieved only by sampling from one channel. If sampling was performed, for instance, with 10 channels, the maximum sampling rate of 30,000 samples per second would yield a sampling rate of 3000 samples per second per channel.

The circuit was designed to interface with the direct memory access (DMA) chip on the IBM PC System board so that the A/D converter circuit would operate independently of the computer system CPU, leaving the CPU free to perform other functions. Under normal operation, the CPU chip retains control of the system bus, and all signals within the computer are routed through the CPU. The system bus is the signal path in the computer over which all information is transferred. If, however, the DMA chip receives from a peripheral device (in this case the A/D converter) a request to transfer data directly to memory, the DMA chip in turn sends a signal to the system CPU. Upon receipt of this signal, the CPU relinquishes control of the system bus to the DMA chip to allow the requested data transfer to take place. Upon completion of the transfer, the CPU regains control of the bus and continues operation where it left off. The time for data transfer through the DMA chip is much less than the time required for the

CPU to execute the appropriate I/O–read and memory–write instructions which would perform the same function. Each transfer of data from the A/D subsystem involved the transfer of two bytes or 16 bits of information. The 12 bit data from the A/D converter was contained in the 12 most significant bits. The user could select, through software, to place either all zeros or the number of the channel from which the data were taken into the four remaining bits.

Control of the experiment required a series of TTL–level pulse trains sent to the stepping motor control circuitry as well as signals to control the probe orientation motor current and motor direction. To provide these signals the circuit also had eight digital input/output lines. An Intel 8255 Programmable Peripheral Interface (PPI) chip was interfaced to the system bus. The PPI is configured with three 8–bit parallel input/output data paths. One of these data paths was used for the control signals. The remainder were used for control of the A/D converter system.

A set of general purpose fortran language subroutines was written to interface the data acquisition and control system to a higher level programming language.

Traverse

The hot–wire probe and probe holder were mounted on a Y–Z traverse. Each of the axes of the traverse was connected by means of a flexible coupling to a stepping motor. Four–phase, permanent–magnet stepping motors with a resolution of 200 steps per revolution were used. The stepping motors were powered by motor drive circuits which were designed and built in house. Each motor drive circuit had separate inputs to control clockwise and counterclockwise motion. A series of pulses at either input would drive the motor, one step per pulse, in the

appropriate direction.

The horizontal, or Y–axis, traverse consisted of two linear motion ball bearings mounted on a platform. The platform rode on two 0.75 inch diameter 36 inch long steel rails. The position of the platform was controlled by means of a lead screw with a pitch of ten threads per inch. With a stepping motor resolution of 200 steps per revolution, the platform would travel 0.0005 inch per step. However, because of the quality of the lead screw and backlash between the lead screw and the lead screw nut, the position of the platform could be known only to within approximately 0.005 inch.

The vertical traverse was of a rack and pinion design. The pinion assembly with the stepping motor was mounted on the platform of the horizontal traverse. The rack extended vertically above the platform. The probe holder was mounted on the top end of the rack. The pinion had a pitch diameter such that one revolution of the pinion translated the rack vertically 20 mm. This gives a vertical displacement of approximately 0.004 inch per step of the motor.

Cross–Wire Probe and Probe Holder

A TSI model 1251–pi2.5 cross–wire probe was mounted in a specially designed probe holder (Figure 2.7). The probe holder permitted rotation of the probe about its axis. The probe holder was actuated by a small electric motor under computer control. In order to determine the average three–dimensional velocity vector at a point in the flowfield, two measurements were taken with the cross–wire probe. The first measurement was taken with the sensing elements of the probe in a horizontal position, the second with the elements in a vertical position. From these measurements all three components of the velocity could be computed. Rather than attempt to control the angular position of the shaft of

the probe motor to move the probe to each of these orientations, the probe motor was connected to the probe by means of a small, toothed belt and a slip clutch assembly. Rotation of the probe was limited by positive stops at 0 and 90 degrees. The probe motor was rotated counterclockwise until one of these stops was met and measurements were taken with the probe in this orientation. The motor was then rotated in the opposite direction until the other stop was met and measurements were taken again. Current to the probe motor was interrupted during the sampling period to prevent vibration and electrical noise from the motor from corrupting the measurements.

Hot–Wire Anemometer System

The hot–wire probes were used with a constant temperature bridge circuit (Figure 2.8) designed by Nosenchuck [15] for use with thin–film probes in water. The circuits were modified by the author for use with hot wire probes in air. For stability of the circuit, an increased frequency response in the feedback stage was required because of higher frequency turbulent fluctuations in air. This was accomplished by substituting the op–amp in the feedback loop with an op–amp of better performance characteristics. Also, the active current limiting originally designed into the anemometer bridge was replaced with a passive current–limiting circuit. This part of the circuit limited current through the probe to prevent accidental burnout of the sensing element. Prior to digitization, the analog signals were passed through a simple signal conditioning circuit. The signal conditioner consisted of a low–pass filter, an offset–and–gain stage, and clipping circuit. The low–pass filters used were first–order passive R–C filters with a cutoff frequency of 700 Hz. The offset–and–gain stage was employed to adjust the signal level so that the entire range of the analog–to–digital converter was utilized. The level

of offset to the signal and the gain were both adjustable from the front panel of the instrument enclosure by means of precision ten–turn potentiometers. To prevent potentially damaging over–voltages from reaching the analog–to–digital converter, a clipping circuit was incorporated into the signal conditioner. The clipping circuit limited the output of the signal conditioner to voltages between -0.7 volts and 10 volts.

Pitot Probe and Pressure Instrumentation

A pitot static probe was used to monitor the flow velocity at a reference point in the flow and for calibration of the hot–wire anemometers. The pitot static probes are of the Rayleigh probe design. The probe body was constructed from 1/8 inch diameter brass tubing. The pressure was measured with a Barocel Pressure Sensor Type 581D–100T and Barocel Electronic Manometer Type 1014A. Velocity measurements obtained with the pitot–static probe, at a reference point in the flowfield, were used to correct the hot–wire data for long–term drift and variation in the blower–motor speed.

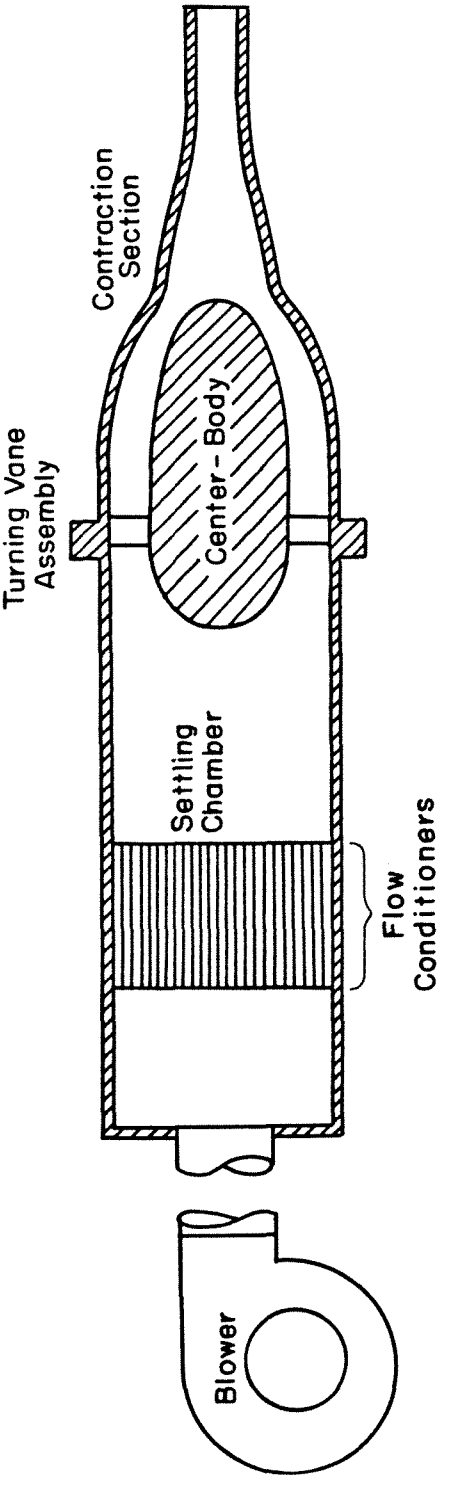

Figure 2.1: Schematic Diagram of the Flow System

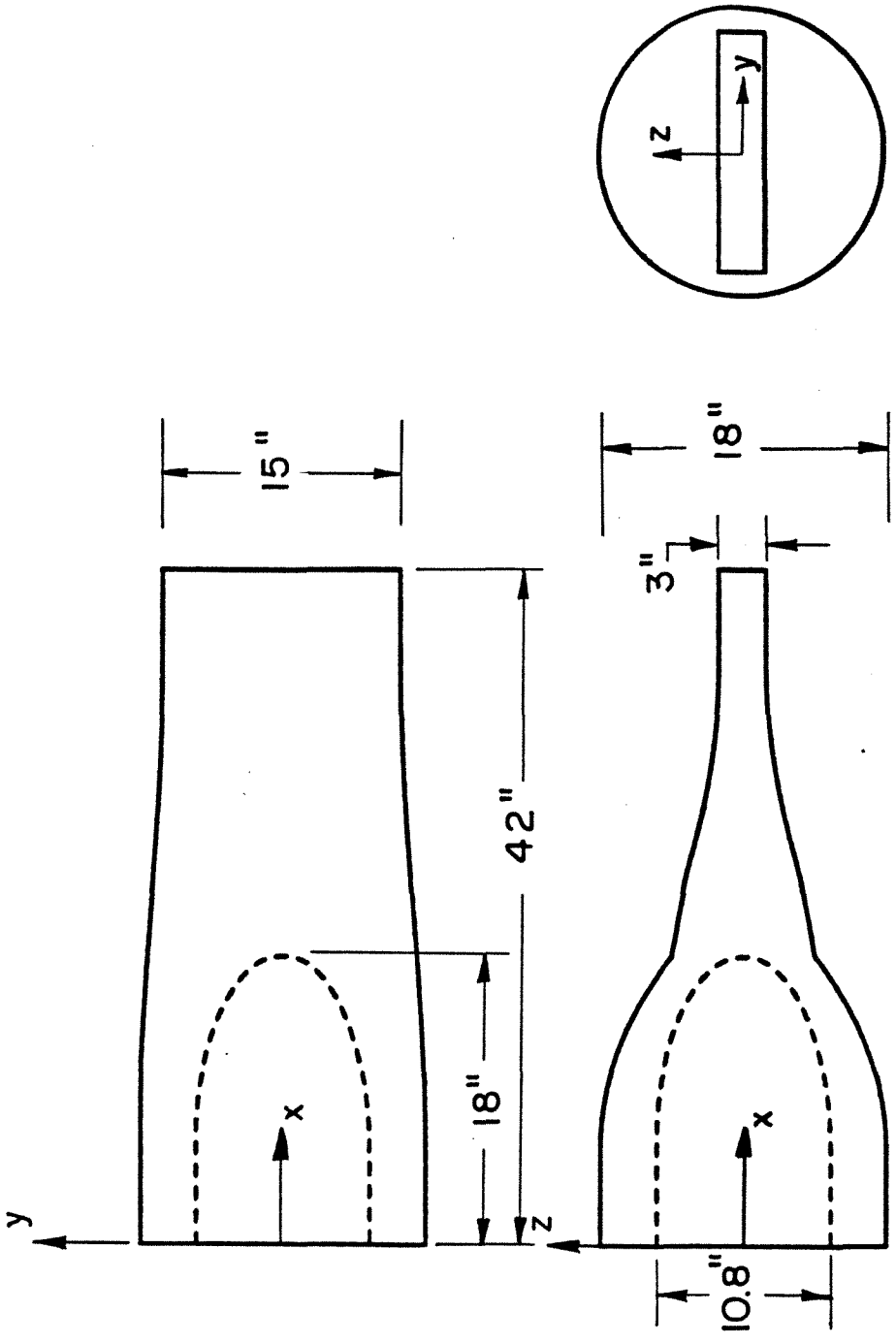

Figure 2.2: Contraction Section

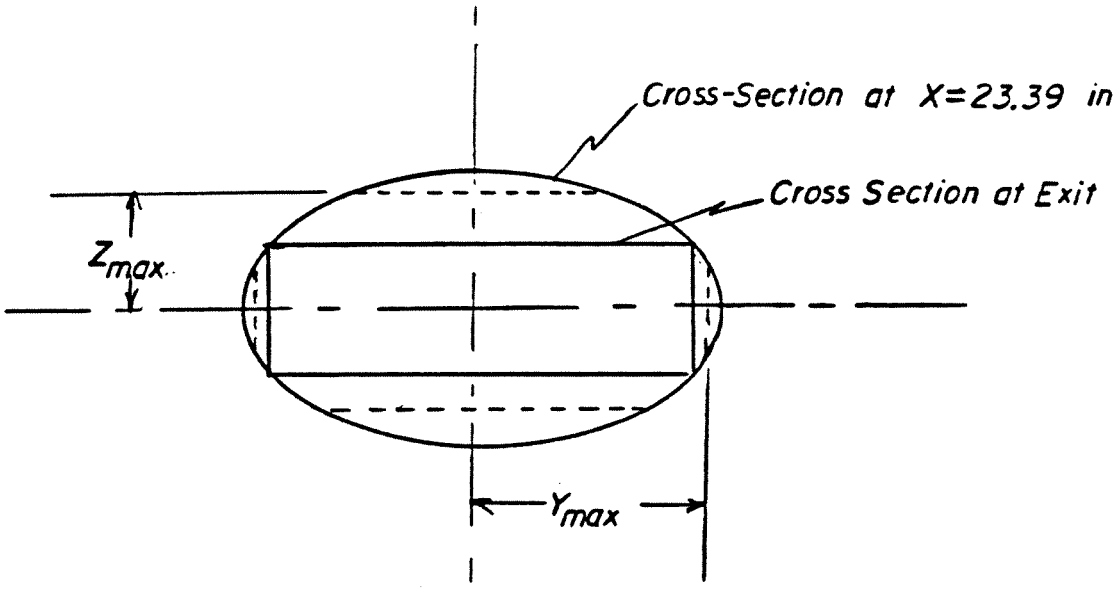

Figure 2.3: Cross Section at the End of the Nozzle

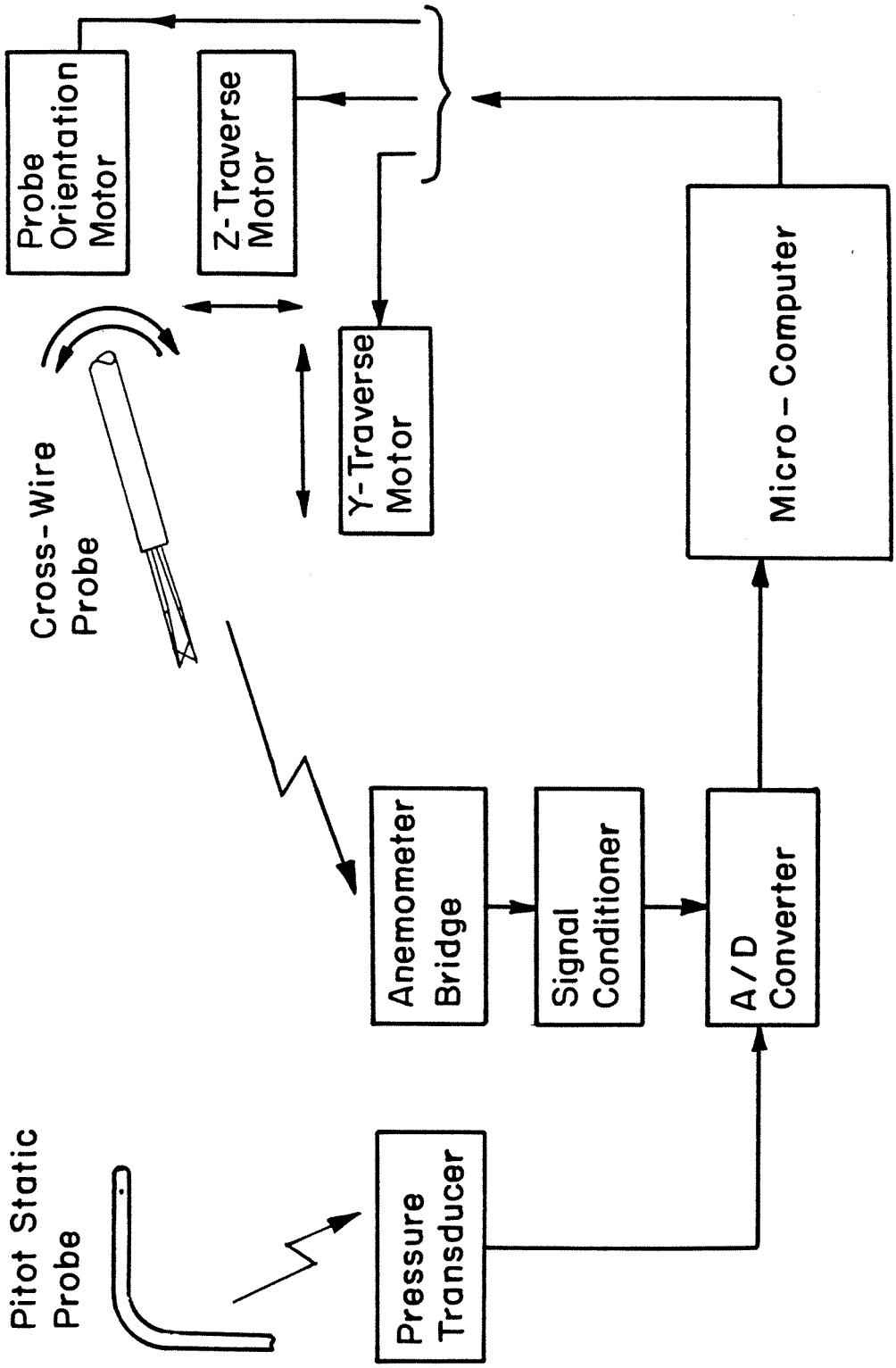

Figure 2.4: Block Diagram of the Instrumentation and Control System

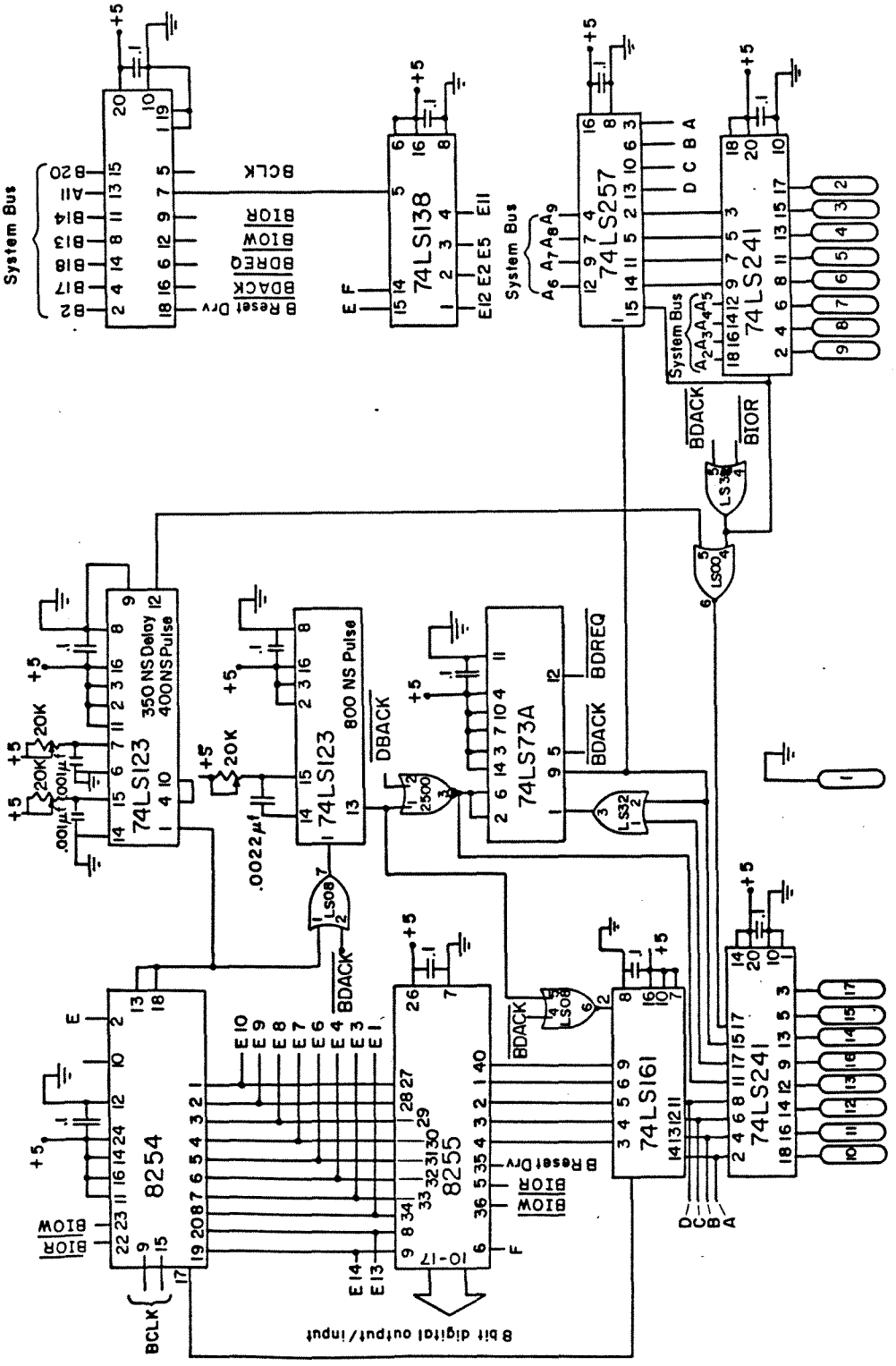

Figure 2.5: Schematic Diagram of the A/D Converter Main Card

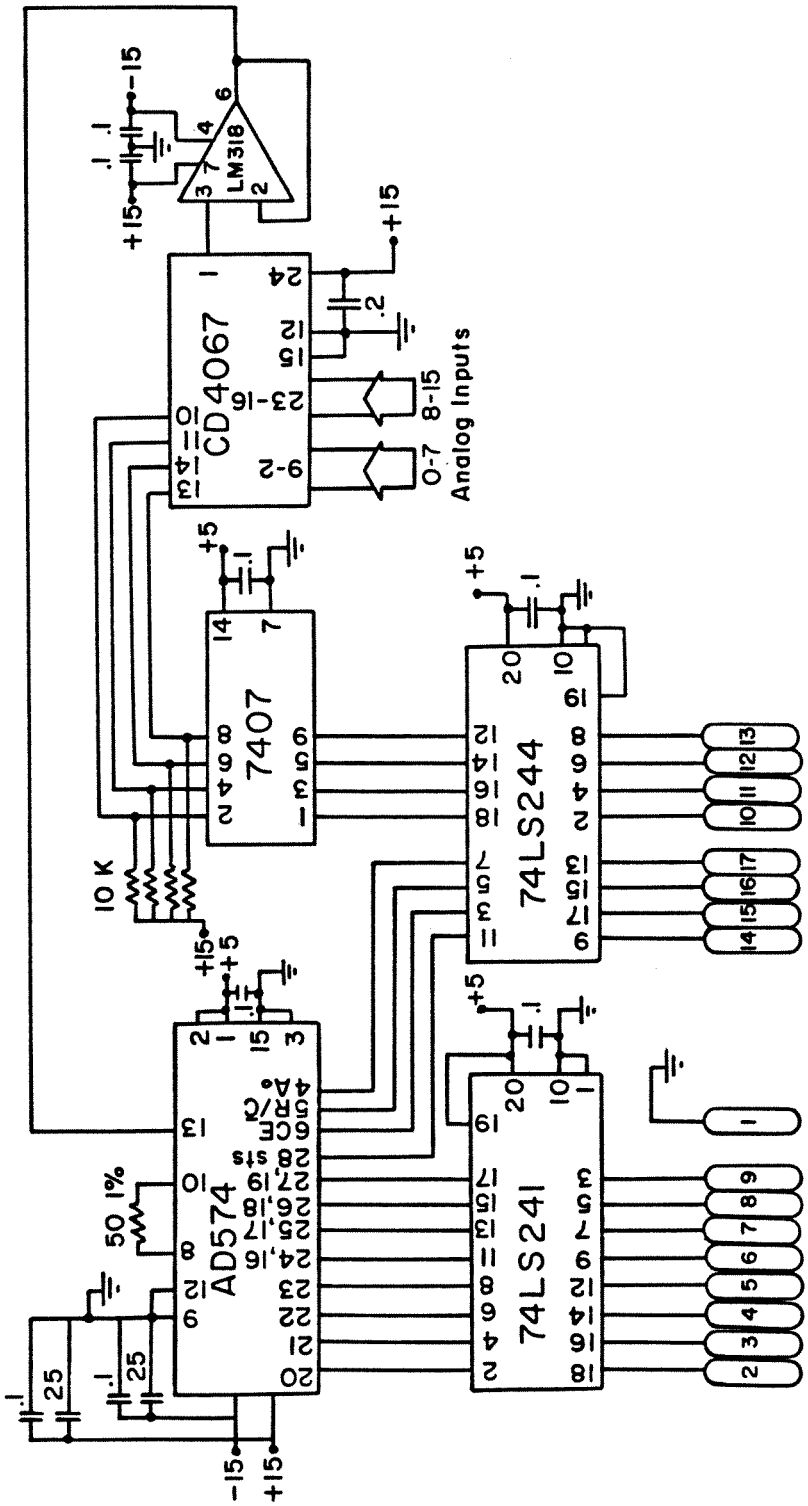

Figure 2.6: Schematic Diagram of the A/D Converter Secondary Card

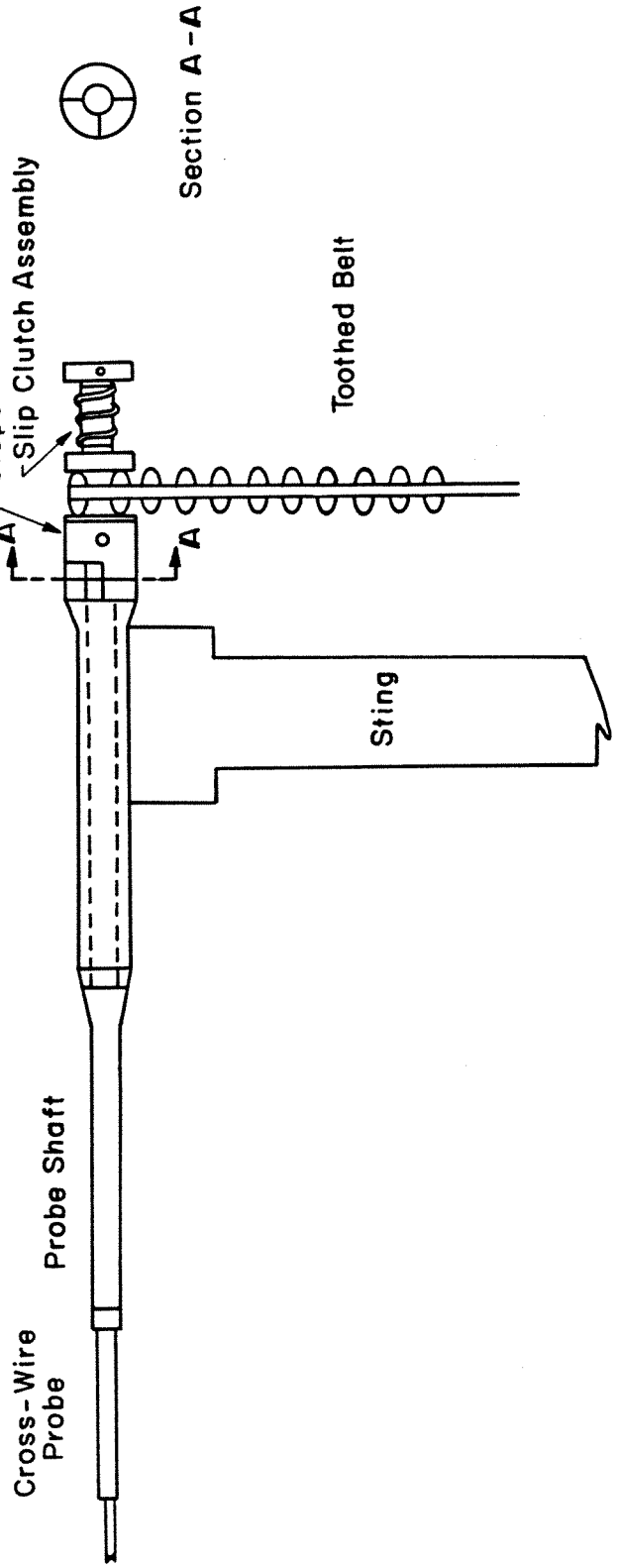

Figure 2.7: Cross–Wire Probe Holder

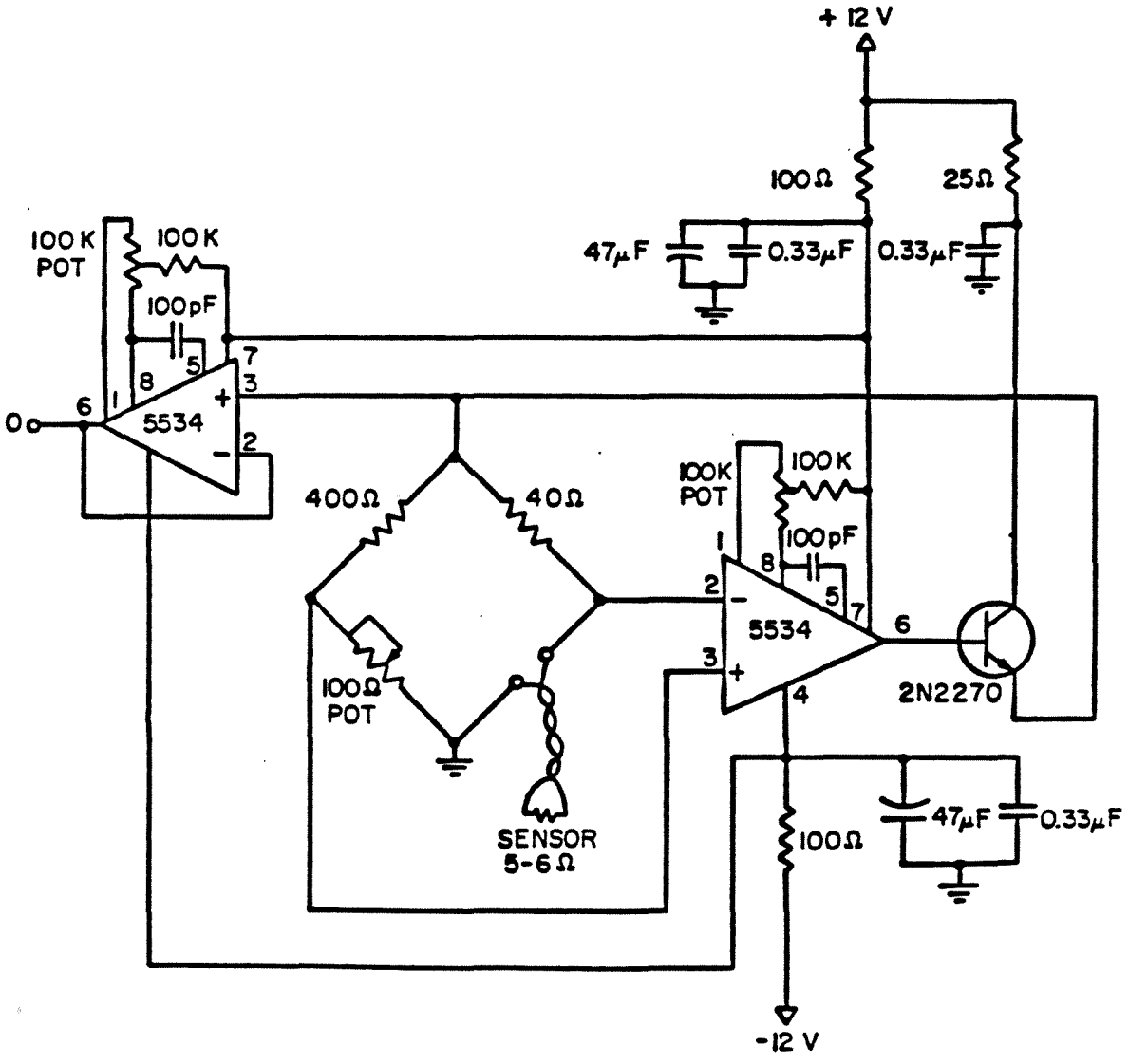

Figure 2.8: Constant Temperature Anemometer Circuit

Chapter 3

Experimental Procedure and Results

3.1 Experimental Procedure and Data Reduction

As stated earlier, the objective of the experimental phase of this investigation was to provide a survey of the velocity vector at the exit plane of the contraction section for different conditions at the inlet to the contraction section. To determine the velocity vector at the exit, a hot–wire anemometer technique was employed. The hot–wire probe used was of the cross–wire or x–wire design. It had two sensing elements that were normal to each other and each made an angle of 45 degrees with the probe body.

For each point at the exit, a set of measurements was taken. Each set consisted of a number of samples with the sensing elements in both the horizontal and the vertical positions. From these samples the time–averaged velocity vector, as well as an indication of the local turbulence level, could be determined.

Hot–Wire Probe Calibration

There have been many proposed relations for the response of a hot–wire anemometer, most notably the empirical relation commonly referred to as King's [16] law;

$$Nu = a + bRe^{n},$$

where η is approximately 0.5 . For a hot–wire probe operated in the constant temperature mode, the Nusselt number (Nu) is proportional to the square of the probe voltage (E), where the constant of proportionality is a function of the probe geometry, the material properties of the sensing element, the operating temperature of the probe and the physical properties of air. The Reynolds number (Re) is based on the probe geometry. Rearranging and squaring King's law gives;

$$V = cE^4 + dE^2 + e. \tag{3.1}$$

There is some discussion in the literature (Perry [17]) as to the adequacy of King's law for the purpose of hot–wire probe calibration. However, in this investigation the hot–wire anemometer was viewed only as a tool, and an exact characterization of its response was not required. It was deemed necessary to provide a calibration curve for the probe that accurately represented its response only for the range in velocity over which it was used. Therefore, as suggested by Equation 3.1, the the hot–wire probe voltage was fit to a fourth order polynomial curve using the least–squares technique.

In order to determine the velocity levels from the hot–wire probe output, it was necessary to calibrate the hot–wire probes in a stream of known velocity. A calibration duct, which was similar in design to the flow system, was used. Instead of an annular–to–rectangular contraction section, it had a contraction section with a circular cross section. Typically, hot–wire probes are calibrated by placing the probes in the calibration stream at a fixed velocity and sampling for a long enough period to obtain a statistically meaningful average. This is then repeated for a number of different velocities and the results are then fit to the chosen functional form. This is a time–consuming process and an effort was made to find a faster, simpler method to calibrate the probes. The hot–wire

probes were placed at the exit of the contraction section along with a pitot–static probe. The blower motor was operated at full speed and switched off. During the coast–down of the blower, 350 samples of the hot–wire probe voltage and the pitot–static probe pressure transducer output were recorded by the analog–to–digital converter. Figure 3.1 shows a typical calibration curve, where the response of the hot–wire probe is plotted against the velocity as determined by use of a pitot–static probe. It should be noted that the apparent scatter in the data points, used to determine the calibration, is due to the fact that the time response of the hot–wire anemometer is much faster than the time response of the pitot–static probe. Therefore, the hot–wire anemometer was able to detect fluctuations in the velocity that were not discernible with the pitot–static probe. A comparison of the two calibration techniques was performed. Two separate calibration curves were determined by using each of the techniques described above. Figure 3.2 shows the normalized difference between these two calibration curves for the velocity range of interest. It can be seen that the difference is less than 1.4 percent and, contrary to what may be expected because of the apparent scatter in Figure 3.1, the difference is greater for the smaller velocities. Furthermore, because the coast–down technique provides many calibration points in the lower velocity range, there is reason to believe that this technique provides a better calibration in that range. In order to verify the repeatability of the coast–down technique, two calibrations of the same probe were performed. Figure 3.3 shows that the normalized difference between these two calibration curves is less than one percent.

Velocity Surveys

Measurements were taken at the exit plane on a mesh with a spacing

of 0.25 inch in both the horizontal (Y) direction and the vertical (Z) direction. Each survey consisted of 11 passes in the horizontal direction with 59 sets of measurements taken each pass. The survey plane is depicted in Figure 3.4. The instrumentation was recalibrated for each pass. Because of drift in the hot–wire probe response, it was desired to minimize the amount of time required for each pass. To do this, data were taken only for a long enough period to obtain a consistent average. The computer was programmed to obtain two blocks of data containing 2000 samples each. The samples in these two blocks were averaged and if the the averages did not agree within 2 percent, the program would obtain 4000 additional samples. The average of the two 4000 sample blocks of data would again be compared. This process would repeat itself, doubling the number of additional samples obtained, until a consistent set of averages was found. For the greater part of the flowfield sampled, only the initial sampling was required. For the regions in the flowfield that had large velocity fluctuations, the sampling process was repeated no more than four times to obtain a consistent average.

Because of disk storage limitations, the data were partially reduced during the run of the experiment. For each point surveyed, every sample was converted to a velocity by means of a look–up table. Only the mean of the velocity and the RMS of the fluctuating part of the velocity were recorded for each sensing element.

Velocity Decomposition

The use of a cross–wire probe for determination of the three components of the velocity vector required that measurements be taken with the sensing elements of the probe positioned at the same point in the flow at two different orientations. From any three of the resulting four measurements, the velocity

vector could be determined. For the purpose of this investigation the hot-wire probe was assumed to be sensitive only to the component of the velocity normal to the sensing element;

$$V_n = \left\|\vec{U}\right\| \sin \gamma_n, \tag{3.2}$$

where V_n is the velocity measured by the n^{th} sensing element and γ_n is the angle between the velocity vector $\vec{U}$ and the sensing element. The angle γ_n can be easily defined in terms of the dot product;

$$\vec{U} \cdot \vec{P}_n = \left\|\vec{U}\right\| \cos \gamma_n, \tag{3.3}$$

where $\vec{P}_n$ is a unit vector describing the orientation of the sensing element. Equation 3.2 can be rewritten using Equation 3.3;

$$V_n^2 = \left\|\vec{U}\right\|^2 - (up_{1,n} + vp_{2,n} + wp_{3,n})^2. \tag{3.4}$$

This gives a nonlinear system of three equations for $\vec{U}$, where;

$$p_{1,n} = \cos \alpha_n \cos \beta_n$$

$$p_{2,n} = \cos \alpha_n \sin \beta_n$$

$$p_{3,n} = \cos \alpha_n.$$

The angle α is measured between the X–Y plane and the sensing element, and β is the angle between the positive X–axis and the projection of the sensing element in the X–Y plane. This system was solved numerically, using Newton's method. For the purpose of velocity decomposition the flow was assumed to be steady. The effect of velocity fluctuations and the resulting uncertainty in the experimental results are discussed in Appendix A.

The final part of the calculation of the velocity vector was a correction to the probe orientation. During the setup of the equipment the hot-wire probe

was visually aligned with the central axis of the duct. Any misalignment was recognized as a possible cause for a distorted picture of the cross–flow velocity vectors, particularly in cases where the cross–flow velocities were small compared with the axial velocities. To correct for this misalignment, the coordinate system from which the velocity vectors were viewed was chosen such that there was no net component to the momentum flux from the cross flow. Typically, the correction showed that the probe alignment was in error less than one degree in both pitch and yaw.

3.2 Experimental Results

To characterize the nature of the flowfield, the velocity at the exit of the contraction was surveyed for four different settings of the inlet turning vanes.

1. 0 degree blade angle
2. 15 degree blade angle
3. 30 degree blade angle
4. split blades, 0 degree inner blade angle, 30 degree outer blade angle

For the purpose of this discussion, the four test cases have been divided into three groups, which will be examined separately.

Case 1: No Swirl

The case of no swirl was run to establish a baseline set of measurements for the purpose of comparison with the more interesting cases run, as well as to characterize the nature of the flow system, which was constructed for this investigation. Nevertheless, this case yielded some interesting results, which were due to the wake shed by the centerbody.

The cross–flow velocity survey for the no swirl test case is shown in Figure 3.5. The most notable feature in the velocity survey is the formation of four axial vortices near the center of the contraction section. It is postulated that this axial vorticity and the resulting cross flow is a result of a ring–like vortex wake shed from the separation region that forms on the center body.

It should be noted that the components of velocity shown in this vector plot are on the order of a few percent of the axial velocity (velocity normal to the page). As a result, there is a large degree of inaccuracy associated with this measurement because the data reduction in this case, in essence, required the subtraction of two nearly equal numbers. One should also note the apparent degradation in accuracy as one moves from left to right in the vector plot. Each pass of the velocity survey began at the left side of the plot, and approximately one hour was required to complete the pass. The drift in the calibration of the hot–wire probe with time was responsible for this inaccuracy. Finally, it should also be mentioned that this was the case most affected by probe misalignment because the cross–flow velocity was small compared with the axial velocity. Figure 3.6 illustrates the velocity vector plot before the final stage of data reduction, as mentioned above, was performed.

Case 2: 15 Degree Blade Angle and Case 3: 30 Degree Blade Angle

In this section the two test cases that will be discussed are the result of the same test configuration, only with varying degrees of swirl. The resulting flowfields from these two cases are very similar in some aspects and therefore will be discussed together. There are some differences in the flowfield that do merit discussion and these will be addressed later. The vector plots of the cross–flow velocity vectors tangent to the exit plane are shown in Figure 3.7 for the 15 degree

swirl case and in Figure 3.8 for the 30 degree swirl case. The most notable feature here is the strong, concentrated vortex that forms, as expected, along the central axis of the duct. The formation of this vortex can be viewed in any number of ways, the simplest of which is by consideration of the conservation of angular momentum. Due to a conservation of angular momentum, the swirl velocity in the neighborhood of the centerbody is increased as the radius of the centerbody decreases. As a result, a strong concentrated vortex is formed along the central axis of the duct.

Perhaps a more informative way to look at this vortex formation is through vorticity considerations. The axial vorticity in the boundary layer along the centerbody is affected in two ways. First, this vorticity is convected downstream along the centerbody so as to form one vortex tube along the central axis of the duct. Second, because the flow is accelerated by contraction of the channel, the vortex strength increases through vortex stretching.

The second predominant feature of these two cases is the two vortices which are formed anti-symmetrically about the central vortex. While these vortices are present for both the low and high swirl cases, they are much stronger and more developed in the high swirl case. These vortices are of opposite sense to the swirl introduced at the inlet. At the inlet, a boundary layer forms on the outer wall which contains vorticity of this opposite sense. The vorticity in these vortices can be attributed to these boundary layers, which are shed from the wall and then entrained into the main stream.

Figure 3.9 also shows a deficit in axial velocity within the vortices. This retardation results because the fluid in these vortices has its origin in the boundary layers and has lower total pressure than that of the main stream. There is also a

surplus of axial velocity in the central vortex.

Figure 3.10 is a contour plot of the axial component of velocity. Contrary to the results obtained for low swirl, this case exhibits a deficit in velocity along the central axis.

Figure 3.11 and Figure 3.12 are velocity fluctuation level maps for the high and low swirl cases, respectively. The turbulence level in the neighborhood of the vortices is higher than in the remainder of the flow. This, perhaps, is for two reasons. First, the fluid in these regions has its origin in the boundary layers on the centerbody and outer wall. Second, these higher levels indicate that perhaps the entire vortex structure is drifting about within the duct. One can see that the turbulence levels are much lower for the 15 degree swirl case than for the 30 degree swirl case.

Case 4: Half–Height Blades

Earlier work by Der et al. [8] indicates the formation of two co–rotating streamwise vortices at the exit of a similar flow configuration. It became apparent that, because these flows are convection–dominated, in order to get vorticity in the center of the stream it would be necessary to introduce vorticity somewhere midspan at the inlet section. This was effected by using turning vanes at the inlet, which were constructed in such a way that the blade angle for the inner and outer half of the annular inlet section could be set independently. Using these blades, one experimental case was examined. For this set of measurements the blade angle for the inner half of the annulus was set to 0 degrees and the blade angle for the outer half was set to 30 degrees.

Figure 3.13 is the cross–flow velocity vector plot measured at the exit plane. One can see the formation of two streamwise vortices. The vortex sheet formed

midspan at the inlet is convected downstream to the exit plane. The resulting distribution of vorticity is such that the induced cross–flow velocities give rise to two regions of swirling fluid.

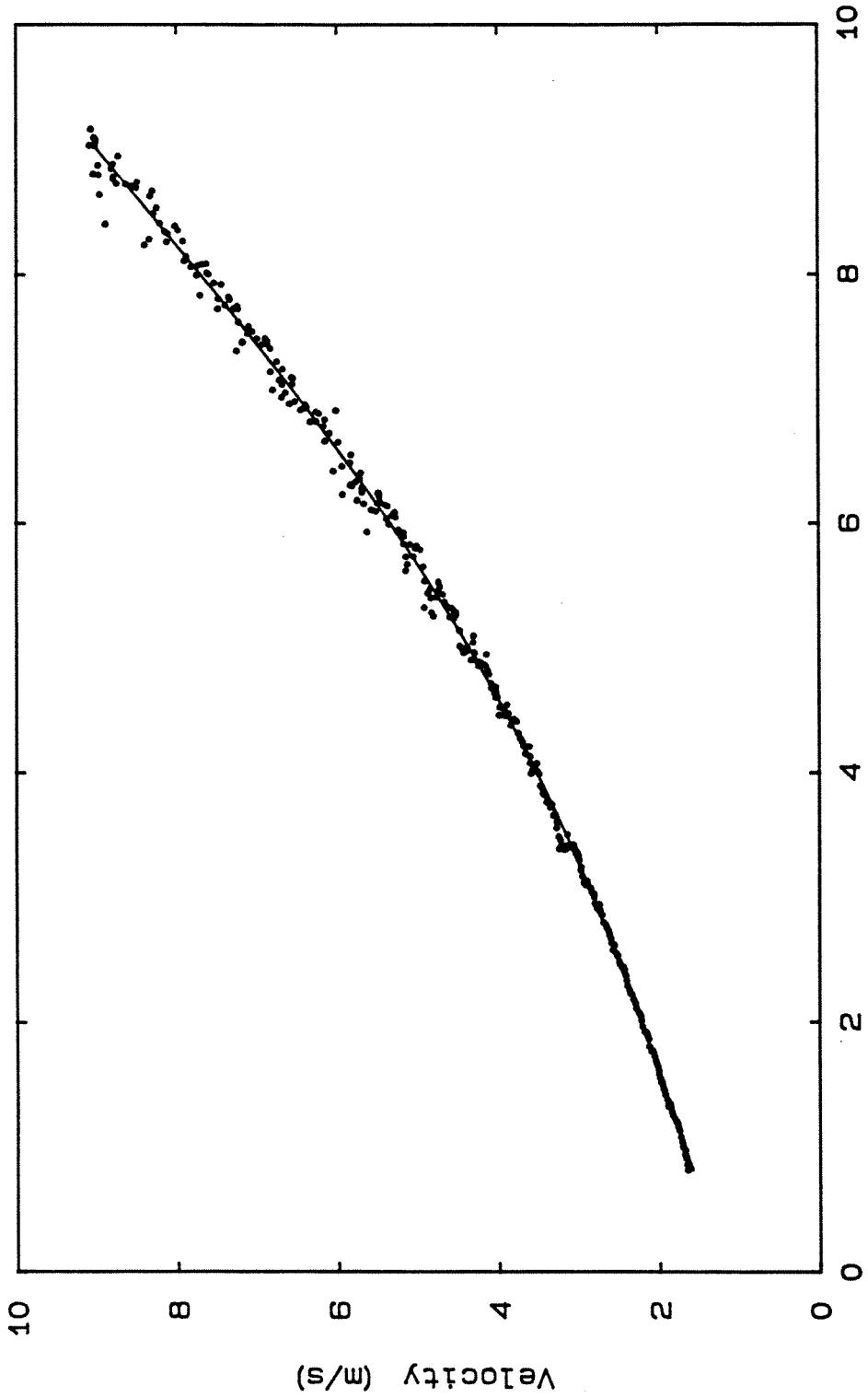

Figure 3.1: Typical Calibration Curve Fit

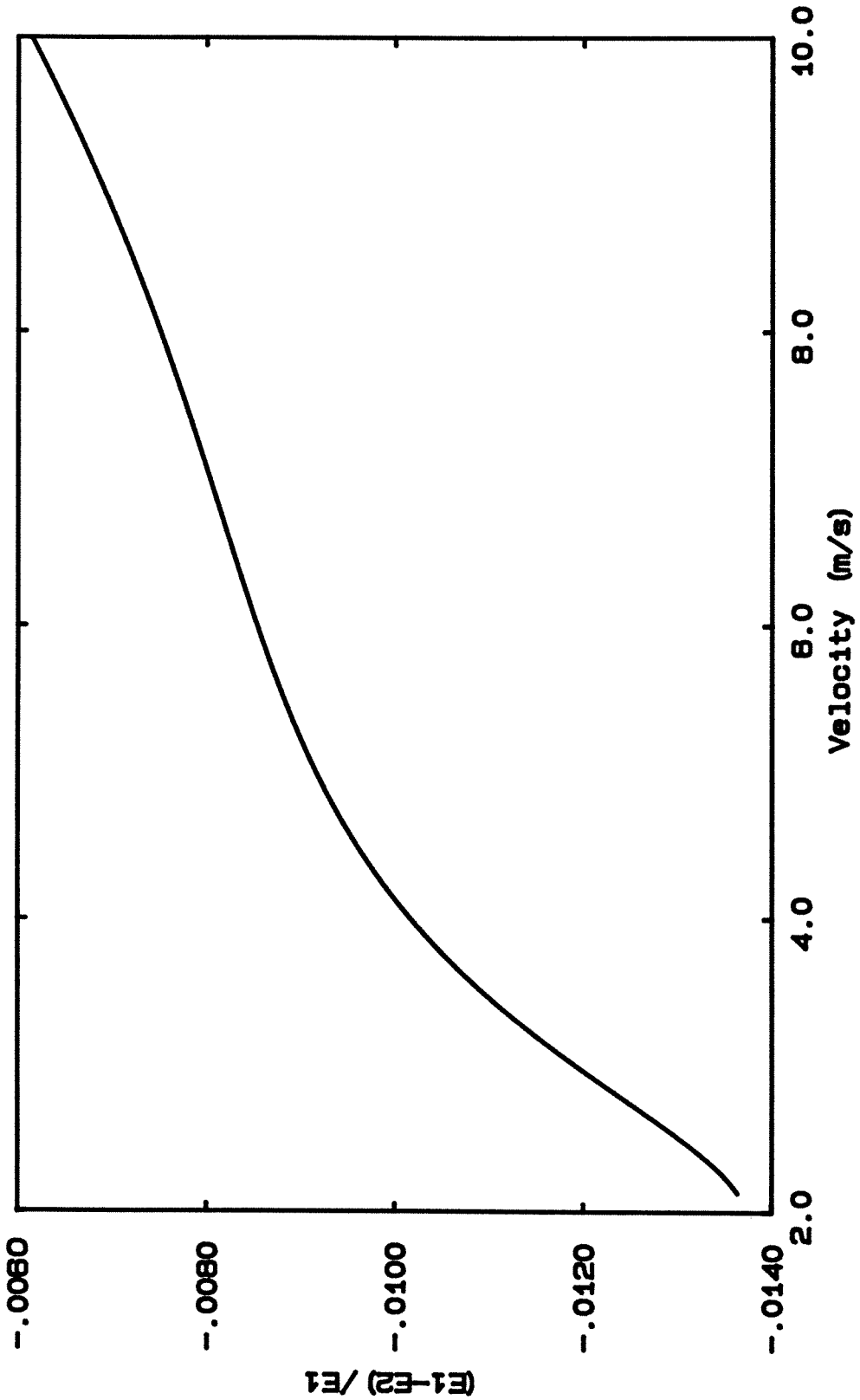

Figure 3.2: Comparison of Calibration Techniques

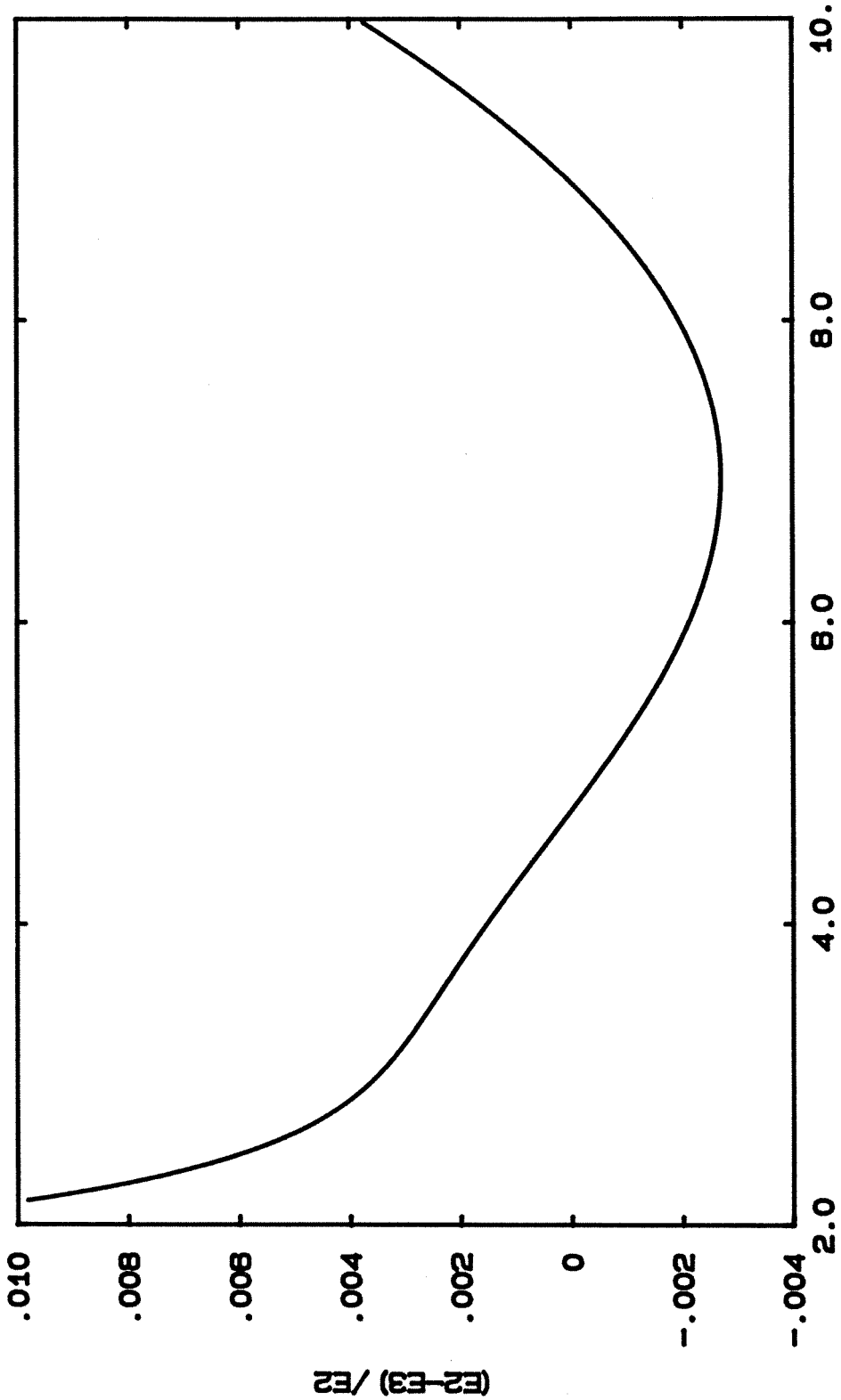

Figure 3.3: Repeatability of Calibration Techniques

Figure 3.4: Survey Mesh at Exit

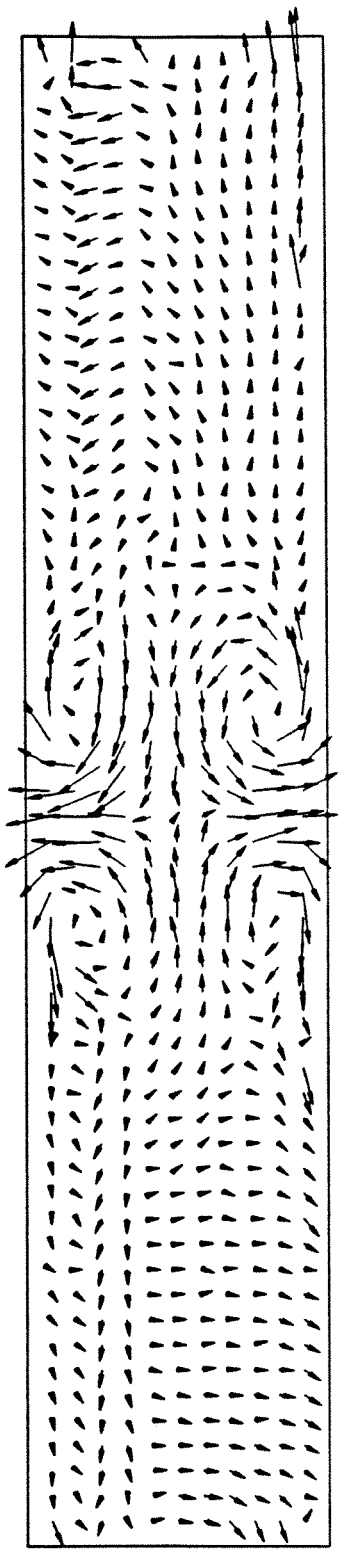

Figure 3.5: Cross–Flow Velocity Vector Plot, No Swirl

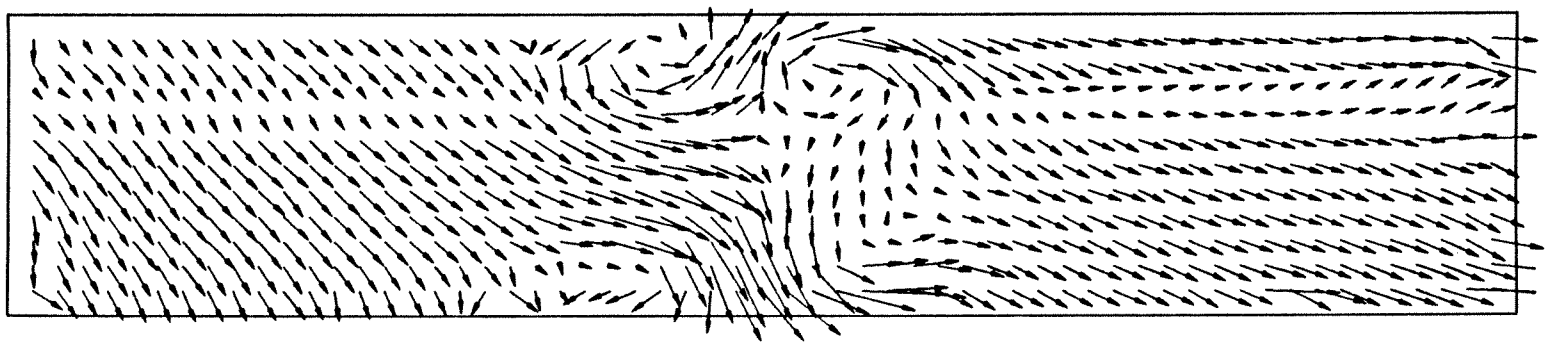

Figure 3.6: Cross-Flow Velocity Vector Plot Without Probe Alignment Correction, No Swirl

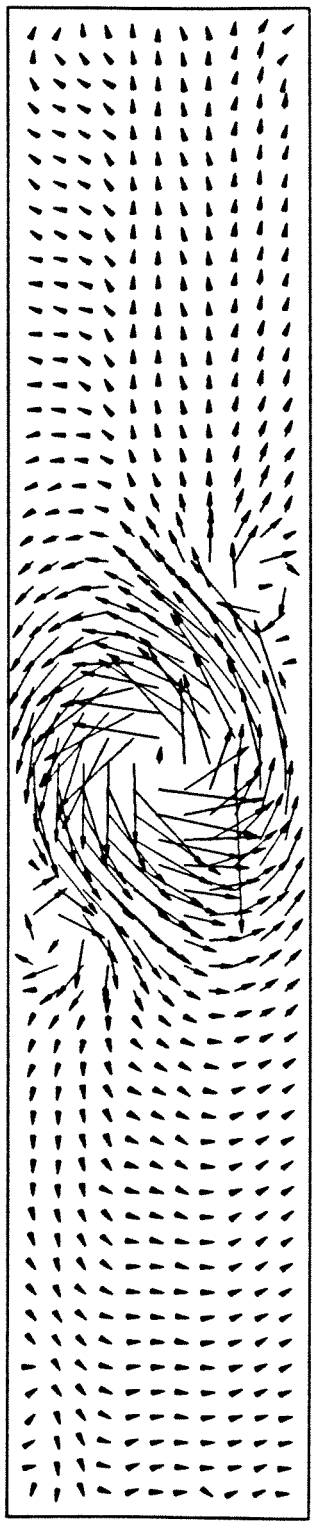

Figure 3.7: Cross–Flow Velocity Vector Plot, 15 Degree Blade Angle

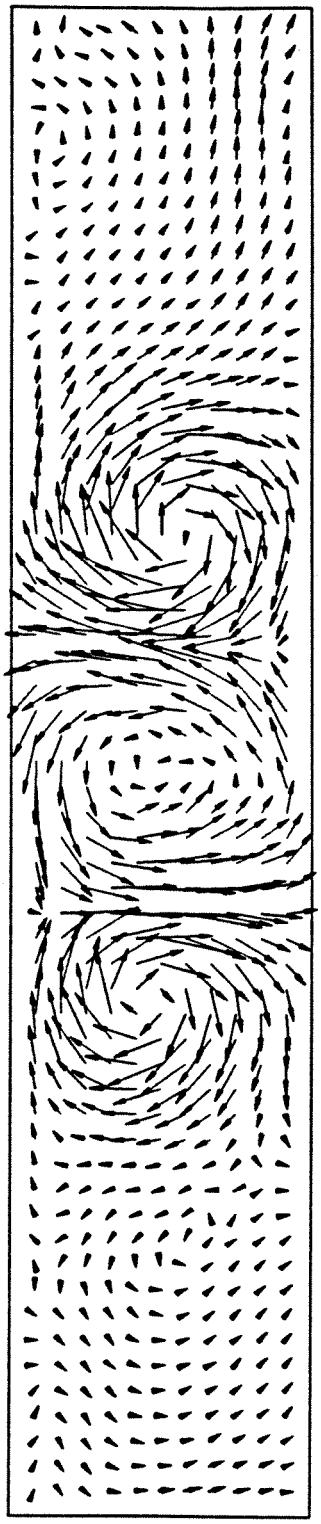

Figure 3.8: Cross–Flow Velocity Vector Plot, 30 Degree Blade Angle

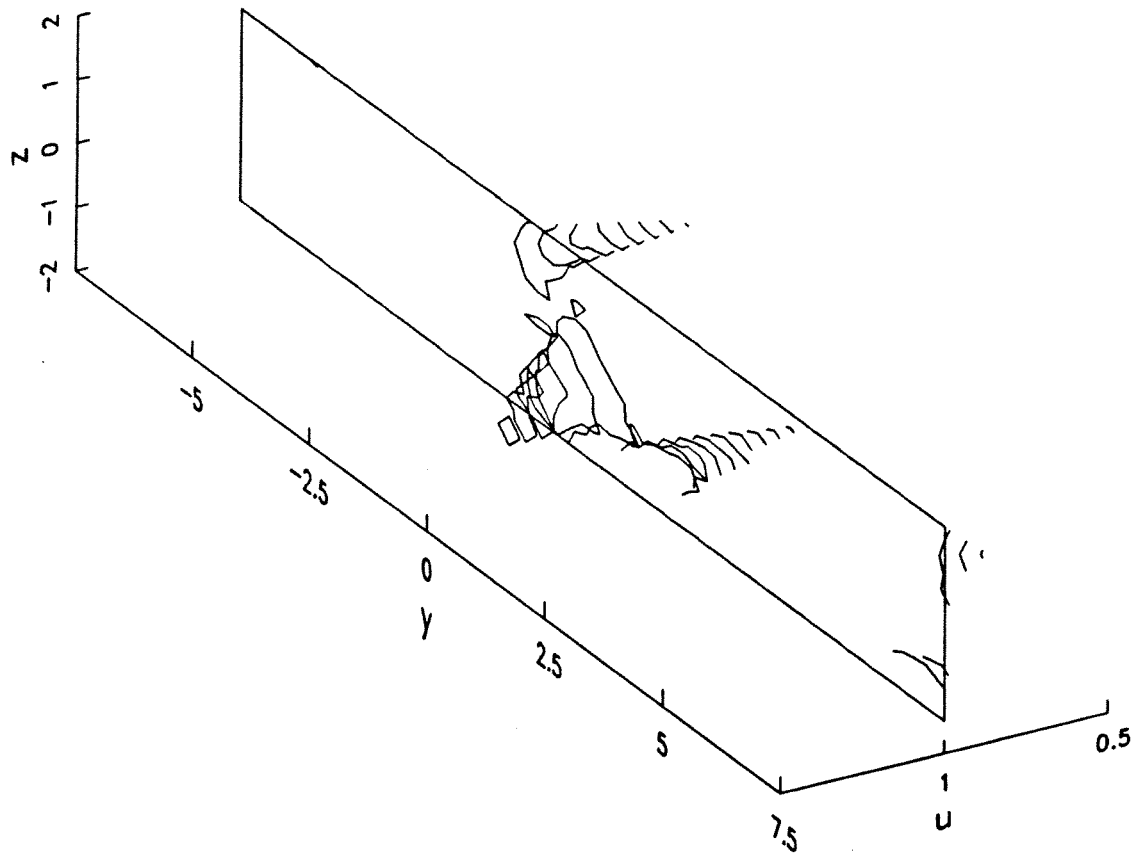

Figure 3.9: Axial Velocity Contour Plot, 15 Degree Blade Angle

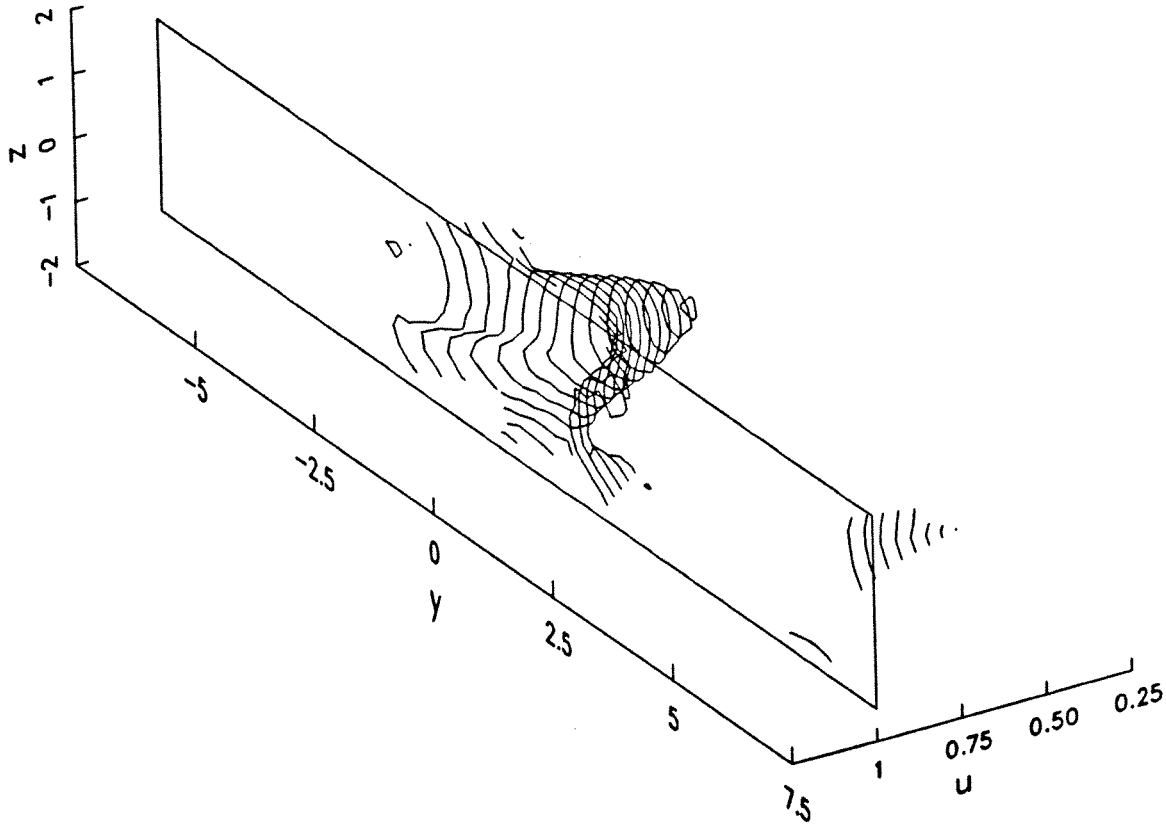

Figure 3.10: Axial Velocity Contour Plot, 30 Degree Blade Angle

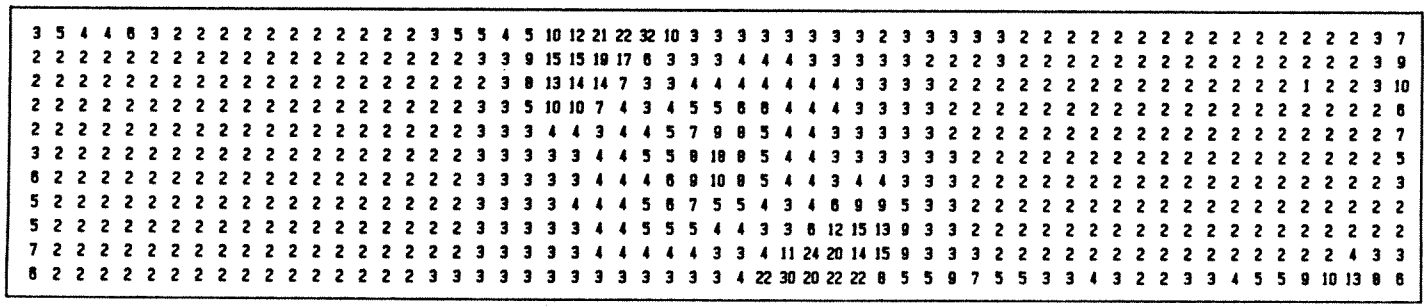

Figure 3.11: Velocity Fluctuation Level Map, 15 Degree Blade Angle

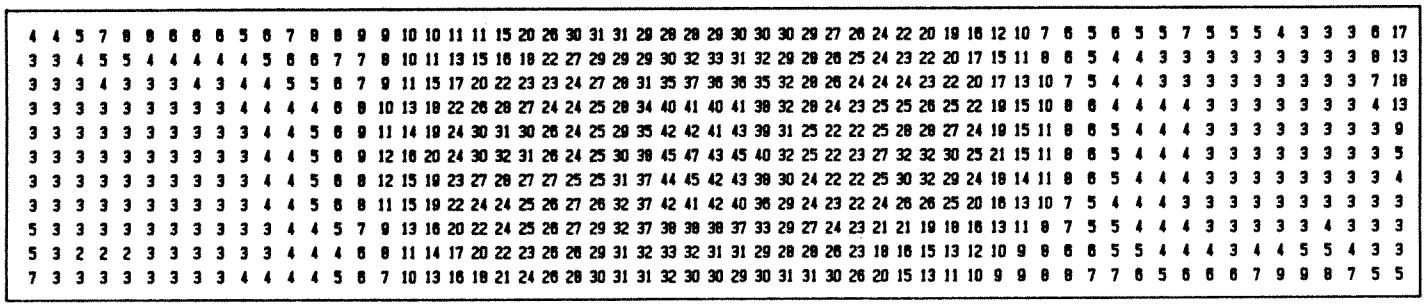

Figure 3.12: Velocity Fluctuation Level Map, 30 Degree Blade Angle

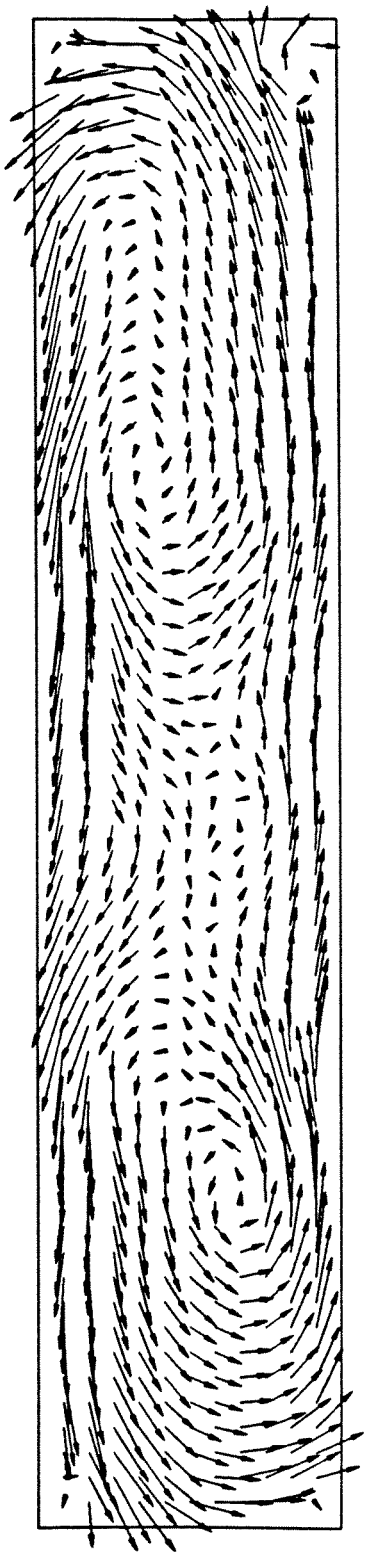

Figure 3.13: Cross-Flow Velocity Vector Plot, Split Blades, 30 Degree Outer Blade Angle, 0 Degree Inner Blade Angle

Chapter 4

Numerical Simulation and Results

The numerical analysis was performed for two distinct purposes. First, it allowed examination of the detailed development of the flowfield between the blade row discharge and the nozzle discharge. These details were not generally available for measurement. Second, once confidence is developed in accuracy of the computational result, it provides a means to examine the discharge flows resulting from more complex blade row configurations. In this chapter we will discuss the numerical approach used to examine this flowfield and then examine the results of some of the numerical cases run.

4.1 Numerical Model

The flowfield was computed using the INS3D computer code developed by Kwak et al. [18]. The algorithm used was an implicit finite difference code, which solves the incompressible Navier–Stokes equations in a generalized curvilinear coordinate system. The method of pseudocompressibility originally proposed by Chorin [19] was used to facilitate the solution to the pressure field. The resulting equations were approximately factored using the technique proposed by Beam and Warming [20]. A brief explanation of the governing equations and of the numerical algorithm will be provided here. For more detailed information that might be

required for use of the program, reference should be made to [18][21][22][23].

The continuity equation with the pseudocompressibility term is:

$$\frac{1}{\beta}\frac{\partial p}{\partial t} + \frac{\partial u}{\partial x} + \frac{\partial v}{\partial y} + \frac{\partial w}{\partial z} = 0. \tag{4.1}$$

The conservation of momentum equation is:

$$\frac{\partial \hat{D}}{\partial \tau} + \frac{\partial}{\partial \xi}(\hat{E} - \hat{E}_\nu) + \frac{\partial}{\partial \eta}(\hat{F} - \hat{F}_\nu) + \frac{\partial}{\partial \zeta}(\hat{G} - \hat{G}_\nu) = 0, \tag{4.2}$$

where:

$$\hat{D} = \frac{1}{J}\begin{bmatrix} p \\ u \\ v \\ w \end{bmatrix}, \tag{4.3}$$

$$\hat{E} = \tfrac{1}{J}\begin{bmatrix} \beta U + \xi_t(p-\beta) \\ uU + \xi_x p \\ vU + \xi_y p \\ wU + \xi_z p \end{bmatrix}, \quad \hat{F} = \tfrac{1}{J}\begin{bmatrix} \beta V + \eta_t(p-\beta) \\ uV + \eta_x p \\ vV + \eta_y p \\ wV + \eta_z p \end{bmatrix},$$

$$\hat{G} = \frac{1}{J}\begin{bmatrix} \beta W + \zeta_t(p-\beta) \\ uW + \zeta_x p \\ vW + \zeta_y p \\ wW + \zeta_z p \end{bmatrix} \tag{4.4}$$

$$\hat{E}_\nu = \tfrac{1}{J}\begin{bmatrix} 0 \\ \tau_{xx} \\ \tau_{xy} \\ \tau_{xz} \end{bmatrix}, \quad \hat{F}_\nu = \tfrac{1}{J}\begin{bmatrix} 0 \\ \tau_{yx} \\ \tau_{yy} \\ \tau_{yz} \end{bmatrix}, \quad \hat{G}_\nu = \tfrac{1}{J}\begin{bmatrix} 0 \\ \tau_{zx} \\ \tau_{zy} \\ \tau_{zz} \end{bmatrix}.$$

The coordinate transformation is given by:

$$\begin{aligned} \tau &= t \\ \xi &= \xi(x,y,z,t) \\ \eta &= \eta(x,y,z,t) \\ \varsigma &= \varsigma(x,y,z,t) \end{aligned} \tag{4.5}$$

Jacobian:

$$J = \begin{vmatrix} \xi_x & \xi_y & \xi_z \\ \eta_x & \eta_y & \eta_z \\ \varsigma_x & \varsigma_y & \varsigma_z \end{vmatrix} \tag{4.6}$$

Contravariant Velocities:

$$\begin{aligned} U &= \xi_t + \xi_x u + \xi_y v + \xi_z w \\ V &= \eta_t + \eta_x u + \eta_y v + \eta_z w \\ W &= \varsigma_t + \varsigma_x u + \varsigma_y v + \varsigma_z w \end{aligned} \tag{4.7}$$

$$D = \begin{bmatrix} p \\ u \\ v \\ w \end{bmatrix} \tag{4.8}$$

Laminar viscous flux terms for an orthogonal grid:

$$\begin{aligned} \hat{E}_\nu &= \frac{\nu}{J}(\xi_x^2 + \xi_y^2 + \xi_z^2) I_m \frac{\partial D}{\partial \xi} \\ \hat{F}_\nu &= \frac{\nu}{J}(\eta_x^2 + \eta_y^2 + \eta_z^2) I_m \frac{\partial D}{\partial \eta} \\ \hat{G}_\nu &= \frac{\nu}{J}(\varsigma_x^2 + \varsigma_y^2 + \varsigma_z^2) I_m \frac{\partial D}{\partial \varsigma} \end{aligned} \tag{4.9}$$

$$I_m = \begin{bmatrix} 0 & 0 & 0 & 0 \\ 0 & 1 & 0 & 0 \\ 0 & 0 & 1 & 0 \\ 0 & 0 & 0 & 1 \end{bmatrix}. \tag{4.10}$$

Numerical Algorithm

The implicit finite-difference, approximate factorization scheme used yields the following set of finite difference equations:

$$\mathcal{L}_\xi \mathcal{L}_\eta \mathcal{L}_\varsigma (Q^{n+1} - Q^n) = f^n, \tag{4.11}$$

where the operators $\mathcal{L}$ are given by:

$$\mathcal{L}_\xi = [I + \frac{\Delta\tau}{2} J^{n+1} \delta_\xi (\hat{A}_1^n - \gamma_1 I_m \delta_\xi) - \epsilon_i \delta_\xi^{(2)}]$$

$$\mathcal{L}_\eta = [I + \frac{\Delta\tau}{2} J^{n+1} \delta_\eta (\hat{A}_2^n - \gamma_2 I_m \delta_\eta) - \epsilon_i \delta_\eta^{(2)}]$$

$$\mathcal{L}_\varsigma = [I + \frac{\Delta\tau}{2} J^{n+1} \delta_\varsigma (\hat{A}_3^n - \gamma_3 I_m \delta_\varsigma) - \epsilon_i \delta_\varsigma^{(2)}].$$

The $\hat{A}_i$ are coefficient matrices of the local linearizations:

$$\hat{A}_i = \begin{bmatrix} L_{i0} & (L_{i1}\beta) & (L_{i2}\beta) & (L_{i3}\beta) \\ L_{i1} & (U_i + L_{i1}u) & L_{i2}u & L_{i3}u \\ L_{i2} & L_{i1}v & (U_i + L_{i2}v) & L_{i3}v \\ L_{i3} & L_{i1}w & L_{i2}w & (U_i + L_{i3}w) \end{bmatrix}, \tag{4.12}$$

where the L are the metrics of the transformation and the right-hand side f^n is given by:

$$f^n = -\Delta\tau J^{n+1}[\delta_\xi(\hat{E}^n - \hat{E}_\nu^n) + \delta_\eta(\hat{F}^n - \hat{F}_\nu^n) + \delta_\varsigma(\hat{G}^n - \hat{G}_\nu^n)] -$$

$$[I - \frac{J^{n+1}}{J^n}]Q^n + \epsilon_e[\delta_\xi^{(4)} + \delta_\eta^{(4)} + \delta_\varsigma^{(4)}]Q^n$$

and γ_i are the viscous terms on the left–hand side.

In applying this scheme, the addition of smoothing terms is necessary to suppress numerical instability and high–frequency oscillations in the solution. In this algorithm, second–order implicit and fourth–order explicit smoothing terms are added to the system of equations. The terms above containing ϵ_i and ϵ_e as smoothing coefficients are the second–order and fourth–order smoothing terms, respectively. In the current investigation it was convenient to adopt a coordinate system of the O–grid type because of the annular inlet region. The grid and grid generation will be discussed in greater detail in a subsequent section. It should be noted here, however, that in the region downstream of the centerbody there is an axis of the adopted coordinate system on which the coordinate transformation is singular. Along this axis the Jacobian and metrics of the transformation are very large. This resulted in numerical difficulties near this axis and high frequency oscillations occurred in this region. A simple order of magnitude estimate suggested that we scale the smoothing coefficients by the square root of the Jacobian of the coordinate tranformation ($\sqrt{J}$) throughout the field. This adjustment alleviated stability and oscillation problems. The boundary conditions were handled explicitly and the values at the boundaries were updated following each time step.

Boundary Conditions

Boundary conditions must be imposed on the pressure and velocity on all boundaries of the computational domain. This resulted in the application of four types of boundary conditions.

At the inflow, the velocity and pressure were simply specified to create the desired flow pattern at the inlet. The inlet section was an annular region of

circular cross section. The boundary conditions used were:

$$p = constant$$

$$U_{axial} = constant$$

$$U_{tangential} = U_{axial} \tan \alpha$$

$$U_{radial} = 0,$$

where α is the turning vane angle.

The solid boundary conditions applied were the usual no–slip condition and an approximation to the no normal pressure gradient to the surface.

$$u, v, w = 0$$

$$\frac{\partial p}{\partial n} = 0$$

The use of boundary fitted coordinates facilitates the application of these boundary conditions. Because the ξ coordinate direction is nearly normal to the solid boundaries and because the grid points were packed near the boundaries, it was deemed adequate to use, on the pressure, the condition that the gradient in the direction ξ is zero at the boundaries.

$$\frac{\partial p}{\partial \xi} = 0$$

This was accomplished by equating the pressure at the wall to the pressure one node away from the wall for each node on the boundary.

Because of the geometry of the flow system and the coordinate tranformation chosen, there is a boundary of the computational domain within the flowfield. This is the downstream extension of the solid boundary formed by the centerbody and can be considered to be a zero radius degenerate centerbody. This boundary

is an axis that extends from the downstream tip of the centerbody to the exit plane. Because this axis is an axis of anti-symmetry, the cross-flow components of the velocity were set to zero along this axis. The boundary condition used for both the axial velocity and the pressure was a second–order inward extrapolation in the ξ direction with the additional constraint that the derivatives of p and u with respect to ξ vanish.

$$\frac{\partial p, u}{\partial \xi} = 0$$

The outflow boundary condition used at the exit plane was the one prescribed by Chang et al. [21]. It consisted of a second–order upwind extrapolation of the velocity followed by a correction to insure global mass conservation. This was accomplished by scaling the extrapolated velocity by the ratio of the inlet mass flux to the outlet mass flux. The pressure at the outflow boundary was updated by using the extrapolated velocity and a simplified form of the momentum equation. The pressures were additionally modified by a factor S.

$$S = \frac{\int_{exit}(\text{momentum corrected pressure})dA}{\int_{exit}(\text{extrapolated pressure})dA}$$

The reader is referred to reference [21] for further detail on this boundary condition.

Computational Grid

The computer code INS3D requires a surface–conforming computational grid. At the current time, general three–dimensional grid generation programs are not readily available. The three–dimensional grid for the current investigation was generated by creating a set of two–dimesional grids for a number of subsequent axial locations and then stacking these grids to form the desired three–dimensional mesh. A uniform mesh spacing in the axial direction was used. For each planar

axial station, the grid was generated using the GRAPE computer code developed by Sorenson [24]. Figure 4.1 shows these grids for the inlet section, for the outlet section, and for two intermediate axial locations. The GRAPE computer code is an elliptic grid generation scheme using the Poisson equation. It contains a number of parameters that control the grid spacing near the boundaries and the angle with which the grid meets the boundary. These parameters were chosen to vary smoothly in the axial direction so that the planar grids, when stacked, would form a smooth three–dimensional mesh. Figure 4.2 shows one quarter of the outer boundary as well as the exit plane. Figure 4.3 shows a side view of the centerbody surface. It should be noted here that the shape of the centerbody was altered for the purpose of the numerical investigation. It was anticipated that the blunt end of the centerbody would cause numerical difficulty and was eliminated in favor of a conical tip on the downstream end of the centerbody. The shape of the outer boundary was also changed so that the cross–sectional area of the flow system would increase monotonically and vary smoothly. The surface shapes were computed in the same way as the shape for the experimental apparatus. This is described in detail in Chapter 2.

4.2 Computational Results

The computer code INS3D was used to model the flow in the experimental flow configuration for three different inlet conditions.

1. 0 degree blade angle
2. 15 degree blade angle
3. split blades, 0 degree inner blade angle, 30 degree outer blade angle

Turbulence modeling for high Reynolds number flows is the subject of much current investigation. Internal flows and regions of separation prove to be particularly difficult to model. Because of the difficulty of computing high Reynolds number flows, the laminar steady Navier–Stokes Equations were solved instead of attempting to solve the Reynolds averaged equations with the use of a turbulence model. The flows investigated numerically were computed with a Reynolds number of 4500 based on the height of the exit cross section. For the purpose of comparison, the Reynolds number for the experimentally determined flowfields was approximately 30,000. The use of the steady laminar Navier–Stokes equations in order to obtain a description of the flowfield, which compares well in a qualitative sense with the experimental results, is deemed adequate so long as the Reynolds number used to compute the flows is high enough so that the flow is momentum–dominated. If this is the case, the boundary layer growth is small and confined to a region near the walls and therefore the gross characteristics of the flowfield are independent of the Reynolds number. The Reynolds number of 4500 was chosen for the computation so that the boundary layer thickness at the exit for the computed flows was approximately the same as the exit boundary layer thickness measured in the experiment.

For the purpose of comparison with the experimental results, the results of the computation at the exit plane were interpolated from the the computational grid onto the mesh used in the experiment for the 15 degree swirl case and for the split blade case. The cross–flow velocity vector plots for these two cases are shown in Figures 4.4 and 4.5, respectively. The contour plot of the axial velocity for the 15 degree swirl case is given in Figure 4.6. A comparison of these plots with those presented in the previous chapter indicates good agreement between

the computational and experimental results.

The numerical results for the no swirl case differ from the experimental results. As mentioned earlier, the shape of the centerbody used for the computation was different from the shape used for the the experiment. The four axial vortices that are apparent at the exit plane in the experimental case are the result of the wake of the centerbody. Because the centerbody used for the computational result was not blunt, the separation of the flow from the centerbody occurred closer to the central axis. Figure 4.7 is a plot of the cross–flow velocity vectors at a station immediately downstream of the centerbody. A comparison of this plot with the result obtained from the experiment demonstrates a qualitative agreement.

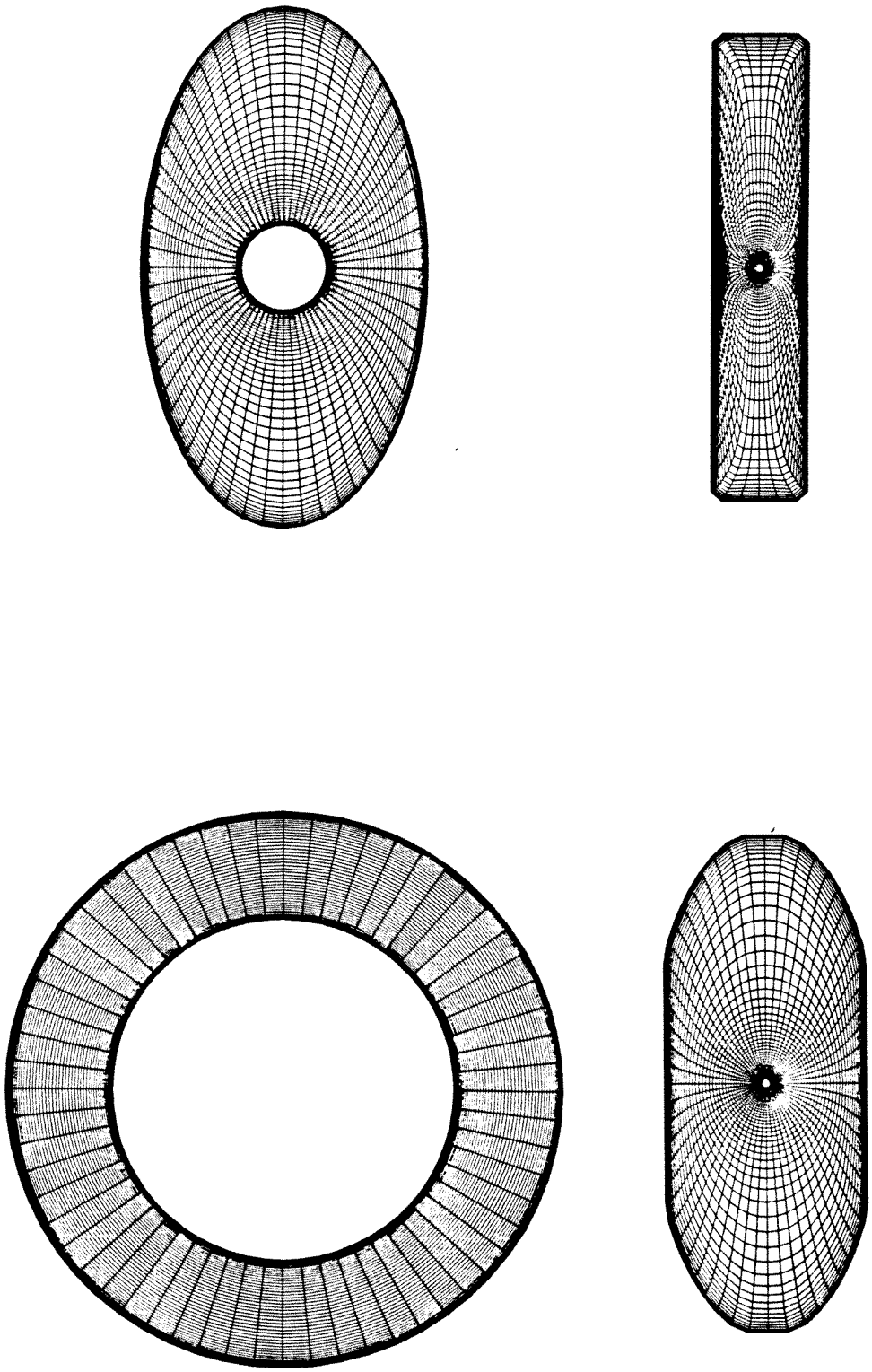

Figure 4.1: Planar Grid for Various Cross Sections

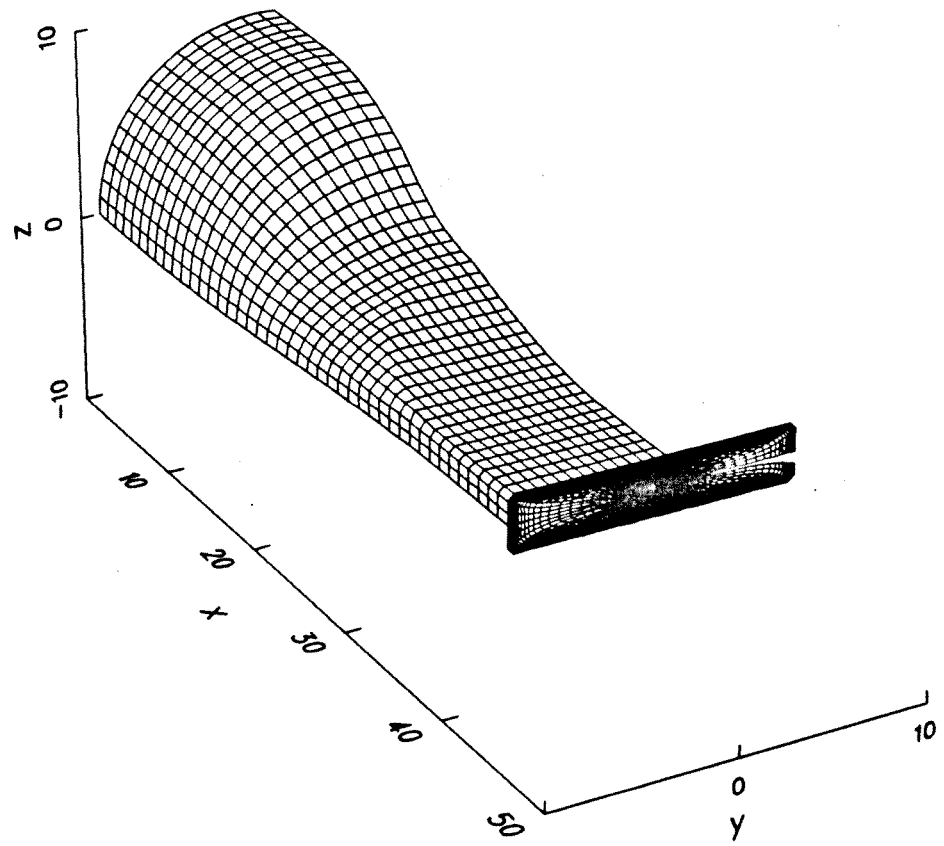

Figure 4.2: Outer Surface and Exit Plane of the Computational Grid

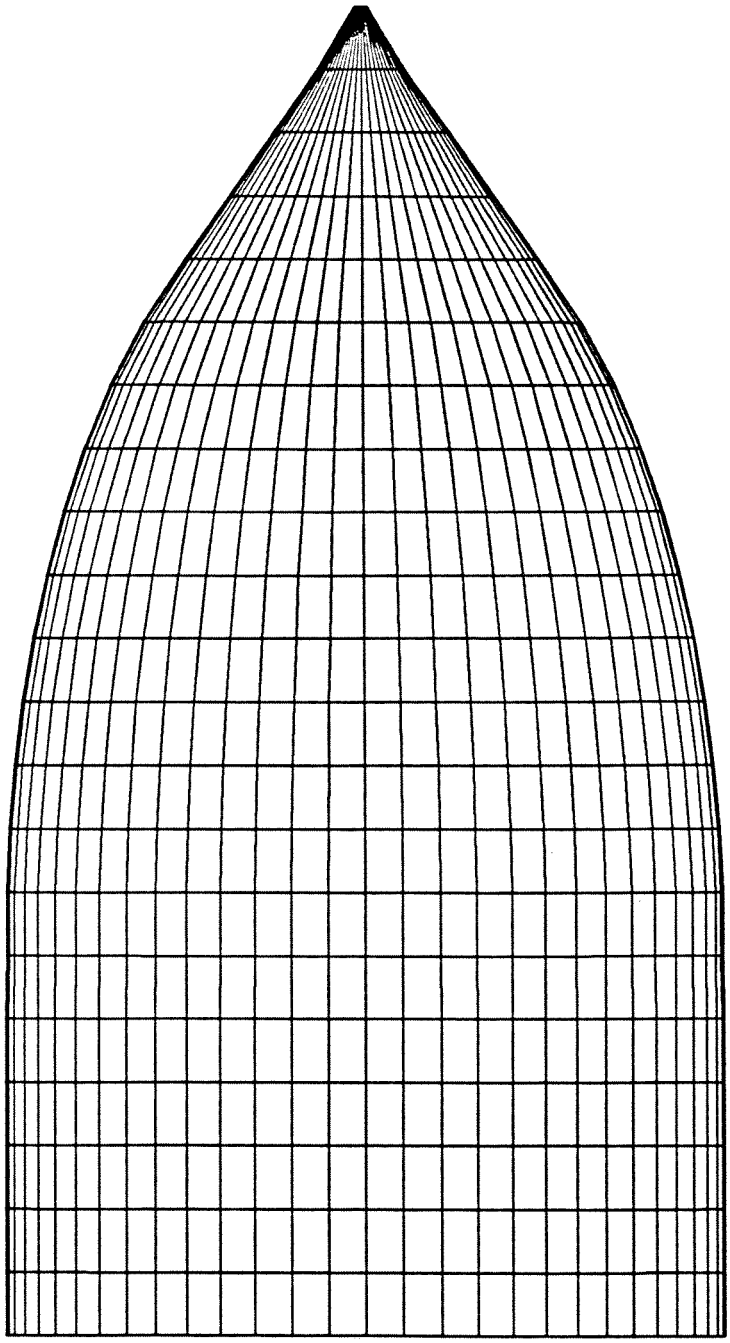

Figure 4.3: Computational Grid: Side View of the Center Body

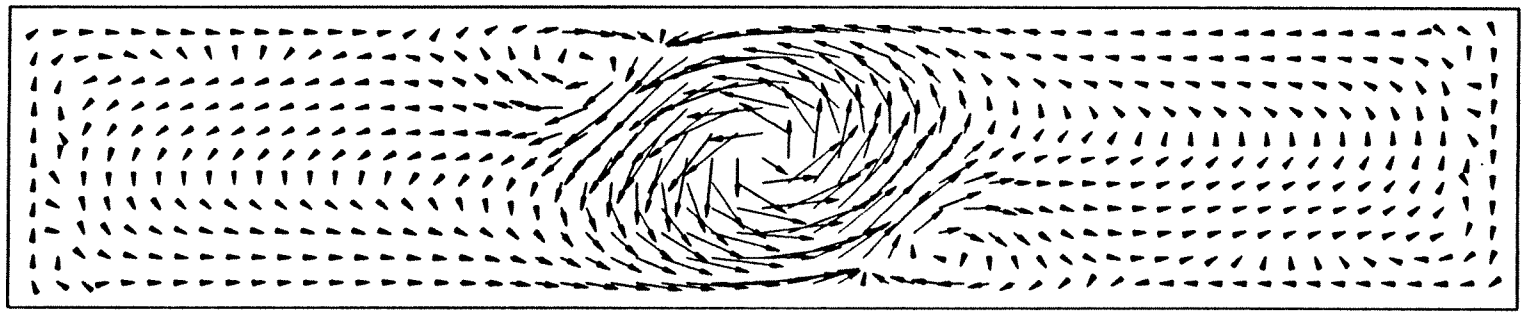

Figure 4.4: Cross-Flow Velocity Vector, 15 Degree Swirl

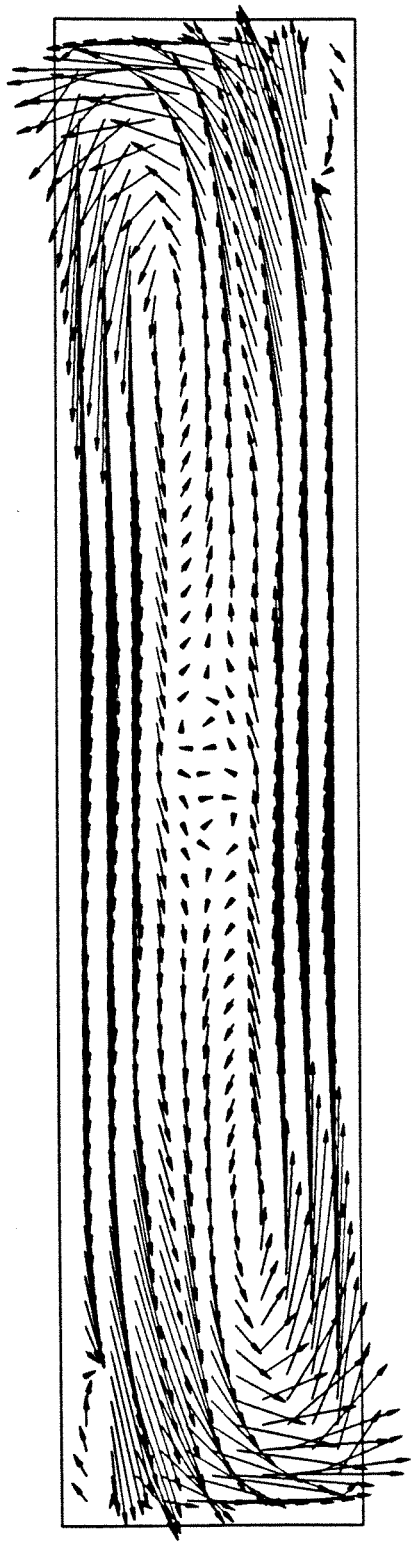

Figure 4.5: Cross–Flow Velocity Vector, Split Blade Case

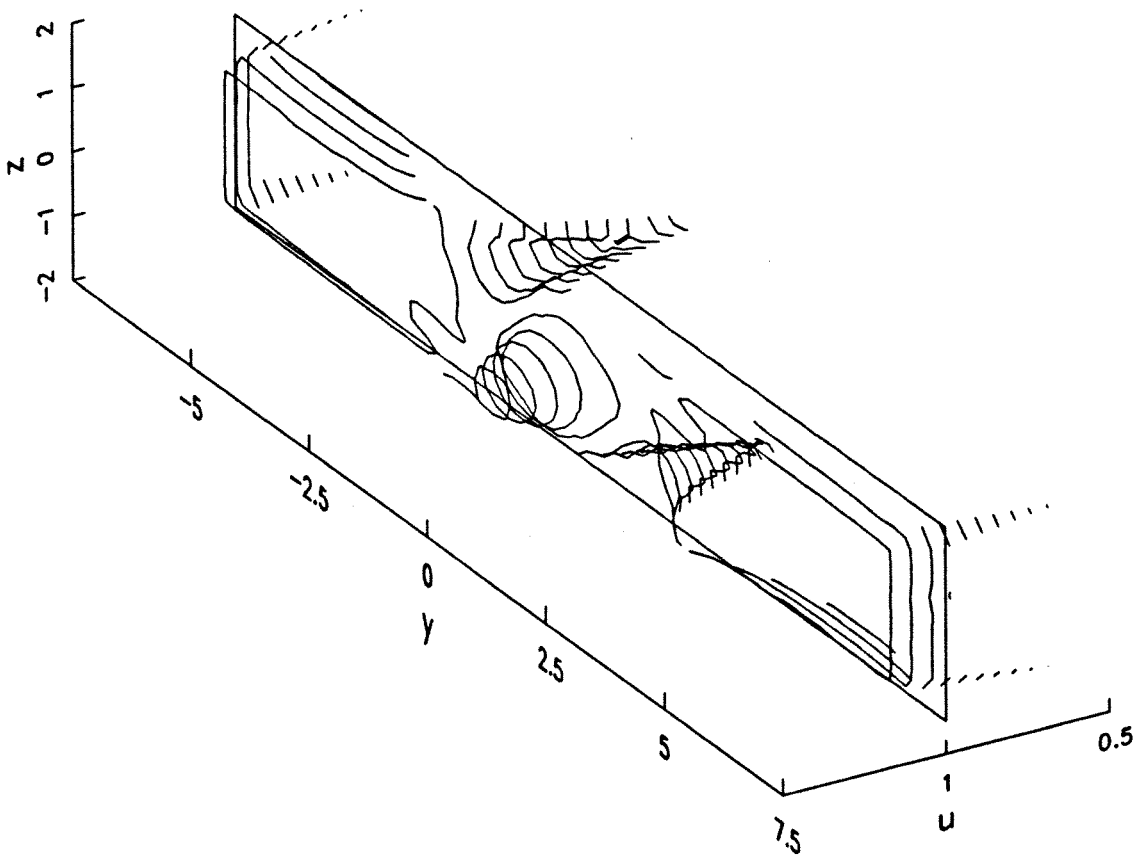

Figure 4.6: Axial Velocity Contour Plot, 15 Degree Swirl

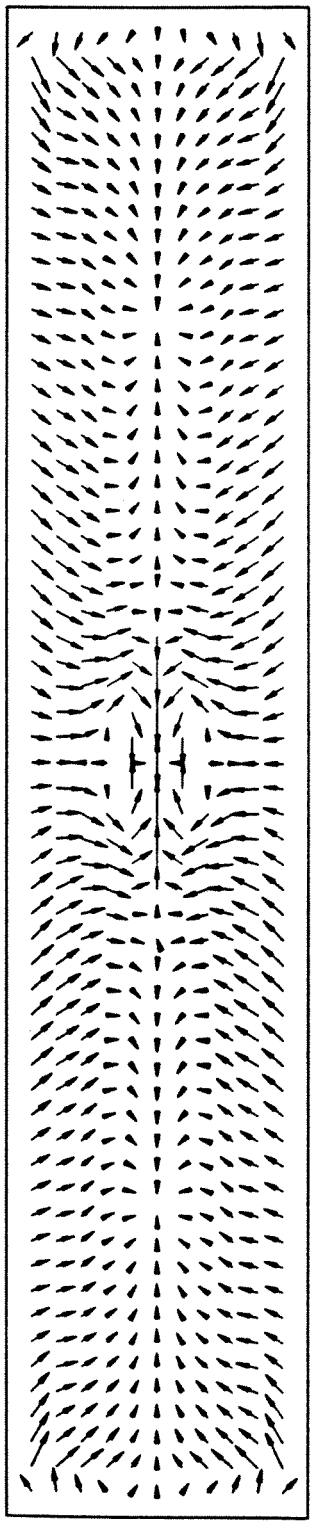

Figure 4.7: Cross–Flow Velocity Vector, No Swirl

Chapter 5

Discussion

In this chapter we will discuss the nature of the examined flowfields in light of both the experimental and numerical results. Again, for the purpose of discussion, the test cases will be divided into three categories. Before we do this, we will discuss some basic ideas regarding the individual fluid dynamic phenomena that are dominant in the flow.

5.1 Presentation of the Results

The presentation and discussion of the results is a complicated task because of the inherent difficulties of displaying and understanding physical quantities that vary in three spatial dimensions. To overcome these difficulties, the results of the computation will be displayed, graphically, in two ways. First, the results will be presented on planar cross–sectional cuts perpendicular to the axial direction, which is also the primary flow axis. Some of the features of the flowfield of current interest evolve slowly in the axial or streamwise direction. In this case, it is informative to view several successive cross–sectional cuts of the flowfield. Cross–flow velocity vector plots and vorticity contour maps will be presented in this way. The view will be in the upstream direction as in Section A–A on Figure 5.1. Because all of the flows to be discussed are antisymmetric about the

duct center, it is sufficient to display only one half of the cross–sectional cut. The half depicted in the plots to follow will be the half from just left of the center to the right edge. A station number will indicate the axial position of the cross section depicted. Figure 5.1 also provides the location of the station numbers. On the contour plots, contours of positive vorticity will be represented by solid lines, contours of negative vorticity will be represented by dashed lines, and the zero vorticity contours will be shown as dotted lines. Second, surface streamlines and surface pressure distributions will be presented as plan views of the lower duct surface. This view is section B–B in Figure 5.1 with the centerbody removed so that it does not obscure the view of the outer wall.

5.2 Vortices or Vortex–Like Patterns

In the following discussions, reference will be made to the formation and identification of streamwise vortices or vortex–like patterns. While it is generally understood that an ideal vortex in an ideal inviscid fluid is a point singularity in the vorticity which gives rise to an infinite velocity, in a real viscous fluid the identification, and even the meaning, of a vortex are not so clear. Because of viscosity the realization of an ideal vortex in a real fluid is not possible. Instead, we have come to call a vortex an identifiable amalgamation of vorticity whose net effect is to create a recirculating or swirling motion in the fluid. Given an amalgamation of vorticity in the fluid, the ability to identify, or perhaps by definition the existence of, a vortex or a vortex–like pattern assocoiated with the amalgamation is dependent upon the frame of reference from which the fluid is viewed. If the velocity with which the amalgamation of vorticity is convected is greater than the velocities induced by the amalgamation, then the amalgamation will not appear

as a vortex in the flow. In the event that the vortices are streamwise, they are more readily identifiable. Even in this case, however, there is some difficulty. The direction from which the amalgamation is viewed, the streamwise direction, must be defined in global or average terms. Because the effect of the vortex is to create a cross–flow component to the velocity, the local direction of the stream cannot be viewed as the streamwise direction. Instead, we choose a direction such that the average cross–flow component of the velocity over some area perpendicular to this direction is zero. For the current investigation it was convenient to choose the outer wall of the transition section as the boundary for this area. The result of this, because of the symmetry of the duct, was that the streamwise direction was parallel to the axial or X direction. Again, if in the cross section, the local cross–flow velocity, due to either the entire distribution of vorticity in the flow or due to the irrotational part of the flow, is large compared with the velocities induced by the local amalgamation, this amalgamation will not be visible as a streamwise vortex. For instance, where the duct is converging, there will be a large inward component to the cross–flow velocity. The velocities induced by an amalgamation may be obscured by this inward velocity. The amalgamations will be apparent in the axial or streamwise vorticity contour plots.

5.3 No Swirl Case

In the no swirl case, the formation of four streamwise vortices was evident at the exit plane. These vortices originate on the centerbody. Figures 5.2–5.4 are the cross–flow velocity vector plots for three cross sections upstream of the centerbody tip. The gradient of the cross–flow velocity, which is a result of the increasing aspect ratio of the outer wall, affects the vorticity distribution in the

boundary layers on both the centerbody and the outer wall. Vortex filaments in the boundary layer, which are initially parallel to the planes of constant X, are distorted by the velocity distribution. The result of this distortion is that the vortex filaments have a component in the axial direction. Figures 5.5–5.12 are contour plots of the axial vorticity, which trace this process from a station near the inlet to a station downstream of the centerbody tip.

In the vorticity contour maps at stations 21 through 24, the formation of additional vortices is apparent in a region near the centerbody tip. These are the result of a complicated three–dimensional separation that occurs on the aft tip of the centerbody. The computational mesh was not fine enough to study the separated region in detail. However, the separation patterns that do occur are similar to those investigated by Hornung and Perry [25][26]. These vortices occur in pairs of opposite sense. They seem to merge along the central axis of the duct. In both the numerical and experimental case, they are not apparent at the exit plane.

5.4 15 Degree Blade Angle and 30 Degree Blade Angle

Before we look at the flowfields that result from these configurations, it would be informative to know where and how vorticity is introduced into the flowfield. In order to determine which features of the inlet vorticity field are important in the formation of vortex patterns at the exit of the transition section, it is necessary to characterize the inlet flowfield produced by the turning vanes. Here we examine the flowfield some small distance downstream of the turning vane assembly, where we have an annular flow cross section formed by two concentric cylinders and therefore adopt a cylindrical coordinate system, as in Figure 5.13,

for the inlet. Recall from Chapter 2 that the turning vanes are flat plate airfoils with no twist. Assuming that the fluid leaves the turning vane assembly parallel to the blades, the tangential component (w) of the velocity is proportional to the axial component (u).

$$w = u \tan\theta, \tag{5.1}$$

where θ is the angle between the turning vane and the duct axis. We assume that any resulting radial component (v) is small and will be neglected for the purpose of this discussion. The assumption that the fluid leaves the turning vane assembly parallel to the blades was verified, using a simple tuft flow visualization. In this cylindrical coordinate system the three vorticity components, ς, ξ, and η in the axial (x), radial (r), and tangential (ϕ) directions, respectively, can be written:

$$\varsigma = \frac{\delta w}{\delta r} + \frac{w}{r} - \frac{1}{r}\frac{\delta v}{\delta \phi} \tag{5.2}$$

$$\eta = \frac{\delta v}{\delta x} - \frac{\delta u}{\delta r} \tag{5.3}$$

$$\xi = \frac{1}{r}\frac{\delta u}{\delta \phi} - \frac{\delta w}{\delta x}. \tag{5.4}$$

In the flowfield, away from the walls so that the effects of the boundary layers are not significant, the vorticity components reduce to:

$$\varsigma = \frac{u \tan\theta}{r}$$

$$\xi = 0$$

$$\eta = 0.$$

This vorticity shed from the turning blade is due to a variation in lift along the span of the blade. Therefore, it should be recognized that the above description of the flowfield is an idealization of the flowfield that actually develops. In the

actual flowfield, the vorticity is present only in the wake of the airfoils. In this description we have distributed the vorticity uniformly in the tangential direction. We will see later that this idealization has little effect on how we view the results.

Because of its importance in the downstream vortex patterns, it is also necessary to examine the axial vorticity that is contained in the boundary layers on the outer wall of the flow passage and on the centerbody. In fact, this vorticity dominates the flowfield. If we examine a cross-sectional cut of the inlet section in a plane perpendicular to the axial flow direction, we have a tangential velocity profile that is represented, approximately, in Figure 5.14. Here we assume that there is a region away from the wall that is unaffected by the formation of the boundary layers and behaves as described above. Because of the no-slip condition, which must be imposed at the walls, the flowfield near the walls must deviate from the uniform tangential velocity profile in order to accommodate zero velocity at the wall. The axial vorticity profile resulting from the velocity profile in Figure 5.14 is depicted in Figure 5.15.

From this figure it can be seen that the level of vorticity in the region away from the wall is small compared to the levels in the boundary layer, and for the purpose of this discussion, the flow away from the wall will be considered to be irrotational. It should be noted here that it is possible, through the use of a set of properly tailored turning vanes, to create a flowfield that is irrotational away from the walls as described above. This, however, is more easily said than done and the vorticity level in the region away from the wall is low enough with the flat blades, so that it can be neglected in initial attempts to characterize the flow. As in any high Reynolds number flow, the boundary layers formed remain thin and, in the absence of separation, these boundary layers and the vorticity associated

with them remain adjacent to the wall.

Finally, vorticity production at the solid walls downstream of the inlet is another source of vorticity in the flow. Given that the flow is irrotational in the region away from the wall, it follows from Kelvin's theorem that the net vorticity (vorticity integrated over the cross–sectional area) created at the walls downstream of the inlet is zero for both the outer wall and the centerbody separately.

As stated earlier, the predominant feature at the exit plane in the low swirl case is the formation of a strong, streamwise vortex along the central axis of the duct. Figure 5.15 shows the vorticity profile at the inlet just downstream of the turning vanes. In the neighborhood of the centerbody, at the blade root, the axial vorticity is high and positive in sense. This vorticity is convected toward the downstream tip of the centerbody and then along the central axis of the duct downstream of the centerbody. This convective process forms a core of axial vorticity along the central axis. This vorticity is subsequently stretched as the fluid is accelerated through the remainder of the contraction section and is apparent as a strong, streamwise vortex at the exit plane.

In the cross–flow velocity plots at the exit plane for the low swirl case, two streamwise vortices located antisymmetrically about the central vortex are visible. As stated earlier, these vortices are the result of the separation of the outer boundary layer into the main stream. The cross–flow velocity vector plots and the vorticity contour plots for a series of axial stations upstream of the exit plane are presented as Figures 5.16–5.22 and Figures 5.23–5.29, respectively. From these plots the growth of the separated region can be traced as it evolves in the axial direction.

The pressure distribution on the outer wall of the duct promotes the sep-

aration of the boundary layer that forms on this wall. Figure 5.30 is a contour plot of the pressure distribution on the lower wall as viewed from above (Section B–B in Figure 5.1). The plot shows a favorable pressure distribution in the axial direction, left to right in this diagram. At any axial station the pressure is lowest immediately under the large central vortex, because the velocity induced by this vortex is high in this region. The cross–flow velocity is affected by the component of the pressure gradient normal to axial direction. We call this component of the pressure gradient the cross–flow pressure gradient, just as we have called the component of the velocity normal to the axial direction the cross–flow velocity. At an axial station before the separation occurs, the direction of the cross–flow velocity immediately above the wall and outside the boundary layer is from bottom to top in Figure 5.1. A type of secondary flow occurs within the boundary layer because of this minimum in the pressure near the central vortex. The cross–flow velocity is affected by an adverse cross–flow pressure gradient. The fluid above the boundary layer has sufficient inertia to overcome the pressure gradient. Some of the fluid within the boundary layer cannot overcome this pressure gradient and therefore follows a path toward the low–pressure region. Figure 5.31 is a plot of the limiting or surface streamlines on the outer surface of the contraction section. A comparison of Figure 5.31 with Figure 5.30, the pressure contour plot, shows that the limiting streamlines are nearly normal to the iso–pressure contours. This indicates that the low–velocity particles near the wall are strongly influenced by, and tend to follow, the pressure gradient. The resulting surface streamlines converge to a single surface streamline, visible near the exit plane immediately above the centerline in Figure 5.31. The single surface streamline to which many surface streamlines converge is called an open negative streamsurface bifurcation by

Hornung and Perry [25] in their effort to qualitatively classify three–dimensional separated flows in terms of the surface streamline topology. This negative bifurcation is important because it is the mechanism by which boundary layer vorticity is carried away from the wall and into the main stream. Figure 5.32, adapted from Reference [25], depicts schematically, an open negative streamsurface bifurcation and the resulting free sheet of bifurcation. If there is any asymmetry in the streamsurface bifurcation, there is also a component of vorticity on the free sheet of bifurcation in the streamwise direction. If this is the case, then the free sheet of bifurcation rolls up to form a streamwise vortex. The strength of this vortex increases in the axial direction as more boundary layer fluid leaves the surface and rolls up with the vortex. This is apparent in the cross–flow velocity vector plots (Figures 5.16–5.22) and the corresponding vorticity contour maps (Figures 5.23–5.29).

In the experimental cross–flow velocity vector plots for the high swirl case, Figure 3.8, this pair of axial vortices is also apparent. Unfortunately, results of the numerical computation are not available for the high swirl case. However, in light of the results of the computation for the low swirl case and the experimental results for the high swirl case, the author has some confidence in his speculation on the differences between these two cases. In the high swirl case, the pair of axial vortices are much larger and move nearly to the center of the duct cross section. This occurs for two reasons.

First, because the cross–flow velocities are much larger and the resulting cross–flow pressure gradient much stronger in the high swirl case, the streamsurface bifurcation forms further upstream. The increased length of this bifurcation line allows for a separation of a greater percentage of the boundary layer fluid.

For the same reason the maximum angle between surface stream lines and the bifurcation line which they approach is greater for the high swirl case than for the low swirl case. Hornung and Perry [25] call this angle the strength of wall streamline convergence or the rate of convergence (see Figure 5.34). For a higher rate of convergence, a greater portion of the boundary layer fluid per unit length of bifurcation separates from the wall at the negative streamsurface bifurcation.

The second reason for the increased strength of the vortices shed from the wall is simply due to the fact that the net quantity of axial vorticity (axial vorticity integrated over the cross section of the boundary layer) is greater for the high swirl case than for the low swirl case. In fact, if we maintain that the fluid that originated at the inlet outside of the boundary layer is still irrotational at the exit, then the net vorticity in the boundary layer is equal in magnitude to the circulation around the central vortex.

The fact that the vorticity in the vortex pair that is shed from the wall must have its origin in the boundary layers on the outer wall shows that there is a maximum for the strength of these shed vortices. A measure of the strength of these vortices is the circulation taken on a contour in a plane of constant X, that surrounds the center of the vortex. The maximum strength of each of these vortices is then equal to one half of the circulation taken on a contour that surrounds only the central vortex.

The axial vorticity contour plots (Figures 5.23–5.29) show regions of axial vorticity near the wall of the sense opposite to the sense of the boundary layer vorticity introduced into the flow at the inlet. This region exists on the bottom wall to the right of the center and on the upper wall to the left of the center. The vorticity production at the wall (vorticity flux from the wall) is proportional to

the component of the local pressure gradient parallel to the wall (Lighthill [27]). It follows then that there are regions of both negative and positive vorticity production at the wall. As stated earlier, the net axial vorticity created at the wall is zero. Therefore, the vorticity production at the wall does not affect the maximum realizable strength of the shed vortices.

These qualitative observations may be given some substance by examining circulation integrals about certain regions at the exit plane. The circulation is defined as:

$$\Gamma = \oint \vec{V} \cdot \vec{dl} \tag{5.5}$$

and is normalized by the circulation introduced upstream by the blade row. For the high swirl case the nondimensional circulation along a contour that includes only the central vortex is approximately 0.75, whereas the circulation around a contour surrounding the entire flowfield is two orders of magnitude lower. The circulation about each of the two shed vortices is approximately -0.3. This indicates that most of the vorticity and hence most of the fluid initially in the boundary layer along the outer wall has been entrained into the main stream. The contours over which these circulation integrals were taken are depicted in Figure 5.33. In choosing these contours, some effort was made to maximize the result of the numerical integration.

Figures 3.9 and 3.10 are contour surface maps of the axial velocity component at the exit plane for the low and high swirl cases, respectively. In the low swirl case there is an excess of velocity in the central vortex, whereas in the high swirl case there is a deficit in the axial velocity. This difference in the nature of the flowfield may be accounted for by the interaction of two separate observed phenomena.

Batchelor [28] discusses the behavior of inviscid rotational axi–symmetric flows. There are two cases he discusses, which are of particular interest here. The flow configurations for these two cases are depicted in Figure 5.35. The condition that the fluid moves with uniform axial velocity and has uniform axial vorticity at some large distance upstream is imposed. This results in a flowfield upstream that is in solid body rotation about the axis and is convected along the axis. For this upstream boundary condition an expression for the axial and tangential velocities at some large distance downstream can be obtained.

For the flow configuration with vanishing inner radius, the downstream axial and tangential velocities become indefinitely large on the central axis. This creates a strong, rapidly swirling region of velocity surplus in the neighborhood of the central axis.

For the flow configuration with the axi–symmetric increase in outer radius, the same inlet conditions produce a deficit in the axial velocity along the central axis. This case is, in a rough sense, similar to a free jet issuing into a room. In both cases we get an increase in effective cross–sectional area. In a study of axi–symmetric swirling jets, Chigier and Chervinsky [29] detected a region of velocity deficit at the center, in the neighborhood of the jet origin. In fact, for high enough swirl, a region of back flow along the central axis was detected.

The axial velocity profiles observed at the exit plane in the experimental part of this investigation can be explained in light of these observations. The geometry of the contraction section was identical for both the high and the low swirl case; the only difference between the two cases is the degree of swirl. In both cases there was a transition section that has a vanishing centerbody and hence a mechanism to create a surplus of velocity along the central axis. The

area change at the exit provides a region where the flow can be decelerated. The question of which of these effects will dominate to create a surplus or deficit of velocity at the exit plane cannot be answered without a detailed description of the vorticity distribution at the inlet as well as the effect of viscosity in altering this distribution as it flows through the transition section.

Finally, it should be noted that the agreement in the axial velocity distribution between the computational result (Figure 4.6) and the experimental result (Figure 3.9), perhaps, is little more than coincidence. It is very difficult to simulate, numerically, the downstream boundary condition encountered in the experiment. Recall, from Chapter 4, that the downstream boundary condition used was a simple extrapolation procedure. In the high swirl case, where the downstream boundary condition has greater effect on the flowfield, this numerical boundary condition will not yield the proper results.

One final look at the pressure distribution on the outer wall for the low swirl case (Figure 5.30) shows that the pressure on the exit lip of the duct is not uniform. In the experimental case we expect the pressure on the exit lip to be uniform and equal to the ambient pressure in the room into which the jet issues. A more accurate model for the downstream boundary condition would provide for uniform wall pressure at the exit.

5.5 Half–Height Blades

As stated earlier, in previous work by Der et al. [8], using a similar flow configuration, the formation of two co–rotating streamwise vortices at the exit plane was apparent. These co–rotating vortices had the same sense as the swirl introduced at the inlet. In the cases discussed above we introduced swirl into the flow at

the inlet in such a way that the majority of the vorticity necessary to create this swirling flow was confined to a region near the blade root. It became apparent that, in order to get a vortex pair with the same sense as the swirl to form at the exit, it would be necessary to introduce vorticity with this sense, at the inlet, away from the blade root. To do this we used turning vanes that introduced swirl only into the outer half of the inlet annulus.

Again, to assess which characteristics of the inlet flowfield are important in the downstream vortex pattern formation, it is necessary to examine the inlet flowfield in some detail. An approximate representation of the tangential velocity just downstream of the inlet turning vanes is depicted in Figure 5.36. In this case, the tangential velocity is zero for the inner half of the annulus and, as in the case above, the tangential velocity for the outer half is $U \tan \theta$. The resulting vorticity profile is depicted in Figure 5.37. Here again, the vorticity shed along the span of the blade due to the variation in lift along the blade in the outer half of the inlet annulus is small compared to the vorticity in the boundary layer at the outer wall and the vorticity shed as tip vortices from the free end of the turning blades. Therefore, the effect of spanwise lift variation in the outer region will be neglected in this discussion. We have, in effect, introduced a cylindrical sheet of axial vorticity midspan in the inlet section. Again, it should be noted that to consider this to be a sheet of vorticity evenly distributed in the tangential direction is an idealization of the actual flow in which the vorticity is introduced midspan as a series of streamwise axial vortices, one shed from each of the tips of the turning vanes. It can be argued that these tip vortices are spread in the tangential direction by the radial gradient of the tangential velocity.

Again, in this case it is informative to trace the flowfield development by

examining the cross–flow velocity and the axial vorticity contours on a series of subsequent cross–sectional cuts of the flowfield. The cross–flow velocity vector plots in Figures 5.38–5.45 and the corresponding axial vorticity contours in Figures 5.38–5.45 trace the development of the flowfield from a cross section near the inlet to the exit plane. In the central region of the flowfield, where no tangential velocity was introduced, the development of the flowfield is very similar to the no swirl case which was discussed in a previous section.

The cross–sectional cut at the exit plane (Figure 5.45) shows the formation of a streamwise vortex or region of swirling flow. An examination of the corresponding vorticity contour plot (Figure 5.53) shows a large area of positive axial vorticity in this region, with no strong peak in the axial vorticity magnitude. By examining the evolution of this flowfield, starting with a circular vortex sheet at the entrance (Figure 5.46), one can trace the development of this sheet as it is convected downstream. The shape of this sheet is distorted as the shape of the inner and outer flow boundary change. The sheet tends to roll up, or at least, vorticity tends to accumulate in the region where the sheet is most distorted. This results in a swirling flow in this region. As mentioned earlier, there is no sharp peak in the axial vorticity magnitude in this region, but instead, a relatively large area that contains positive axial vorticity. The velocities induced by this region tend to re–entrain the rotational fluid originally in the shear layer as well as a portion of the irrotational fluid from the central region of the flow. As a result, we get a broad region of positive axial vorticity.

Also worth noting are the two small streamwise vortices, one of which forms in the lower right–hand corner of the rectangular exit cross section, and the other in the diagonally opposed corner. These are due to the separation of

the boundary layer that forms on the outer wall.

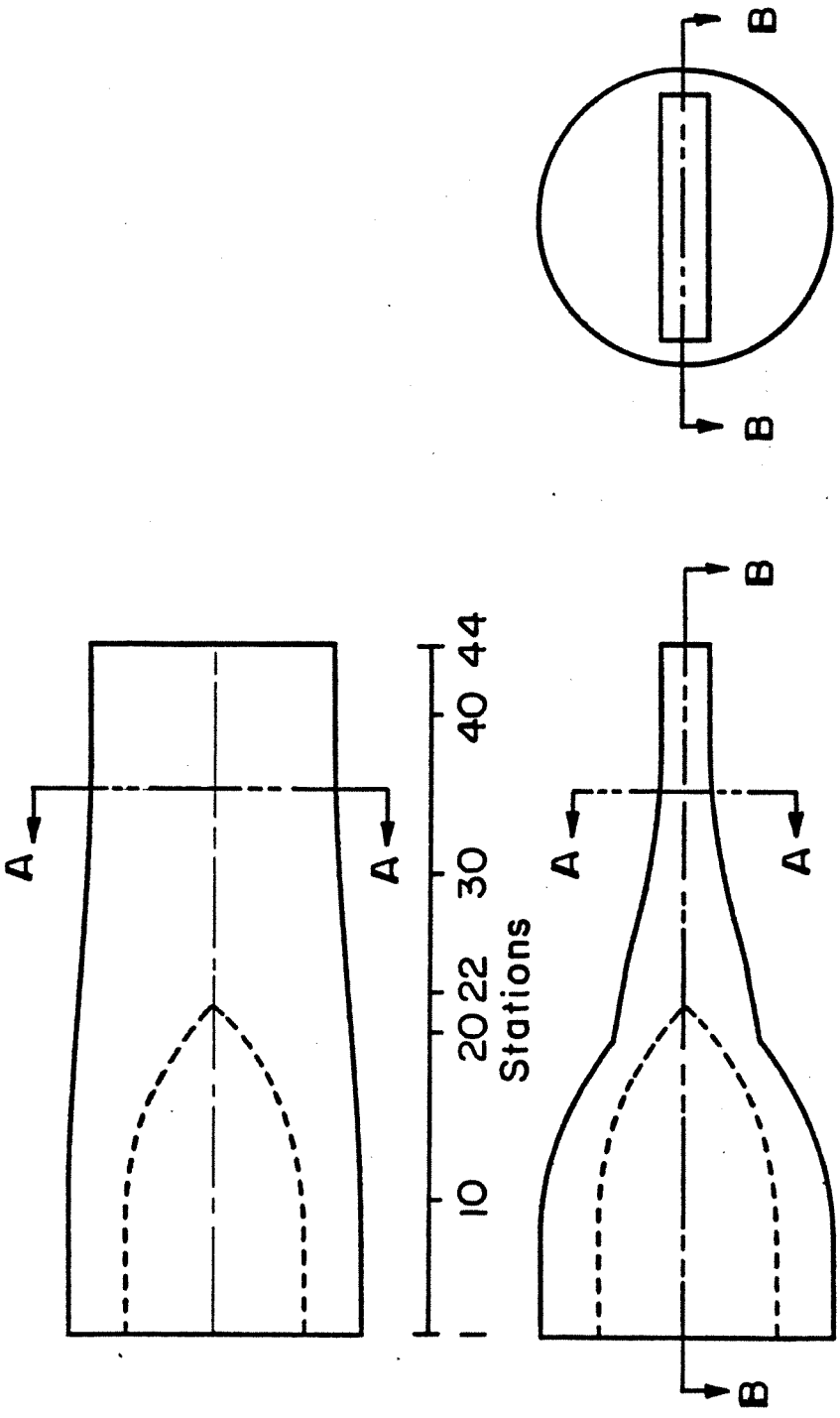

Figure 5.1: Sections and Stations

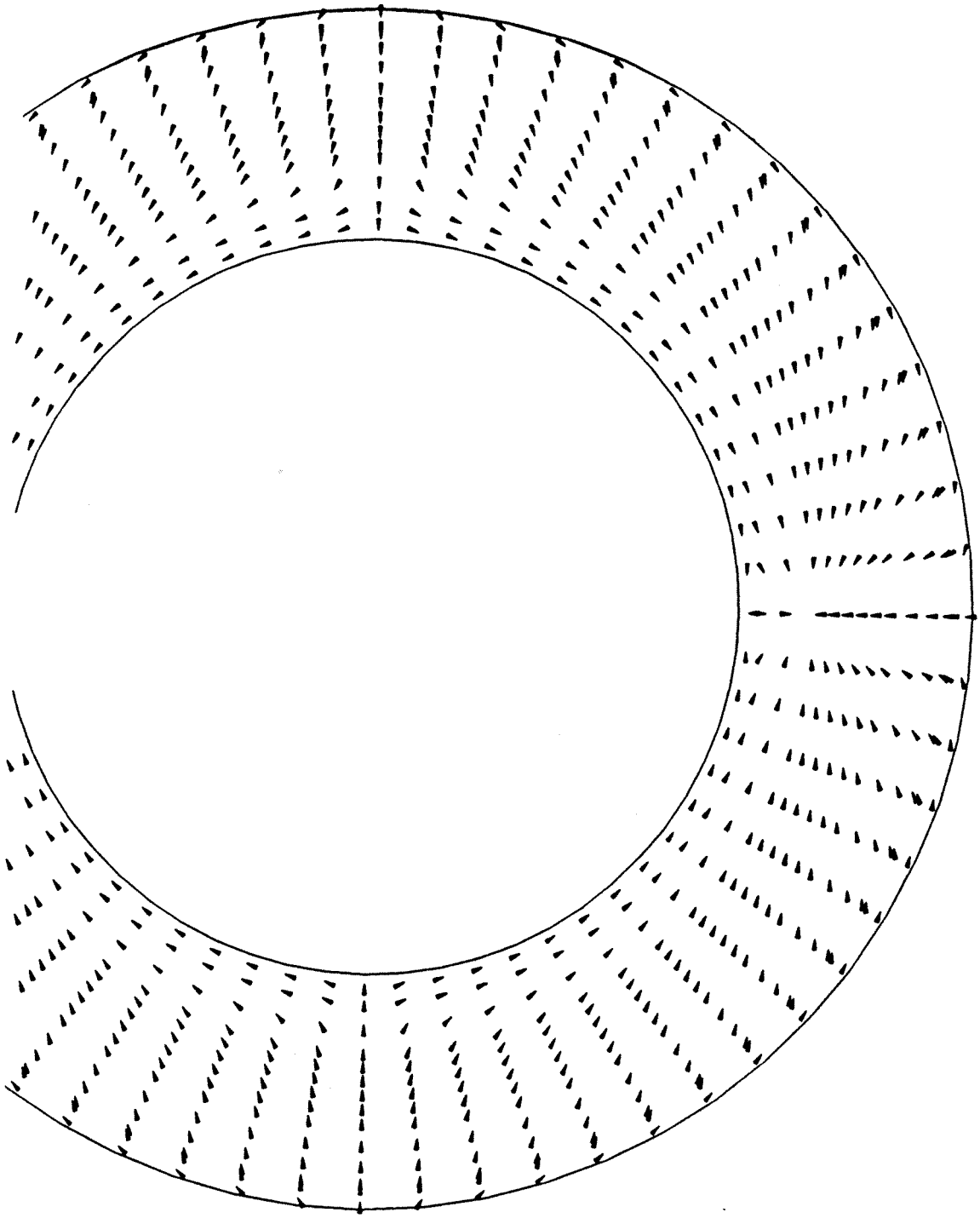

Figure 5.2: Cross–flow Velocity at Station 6, No Swirl Case

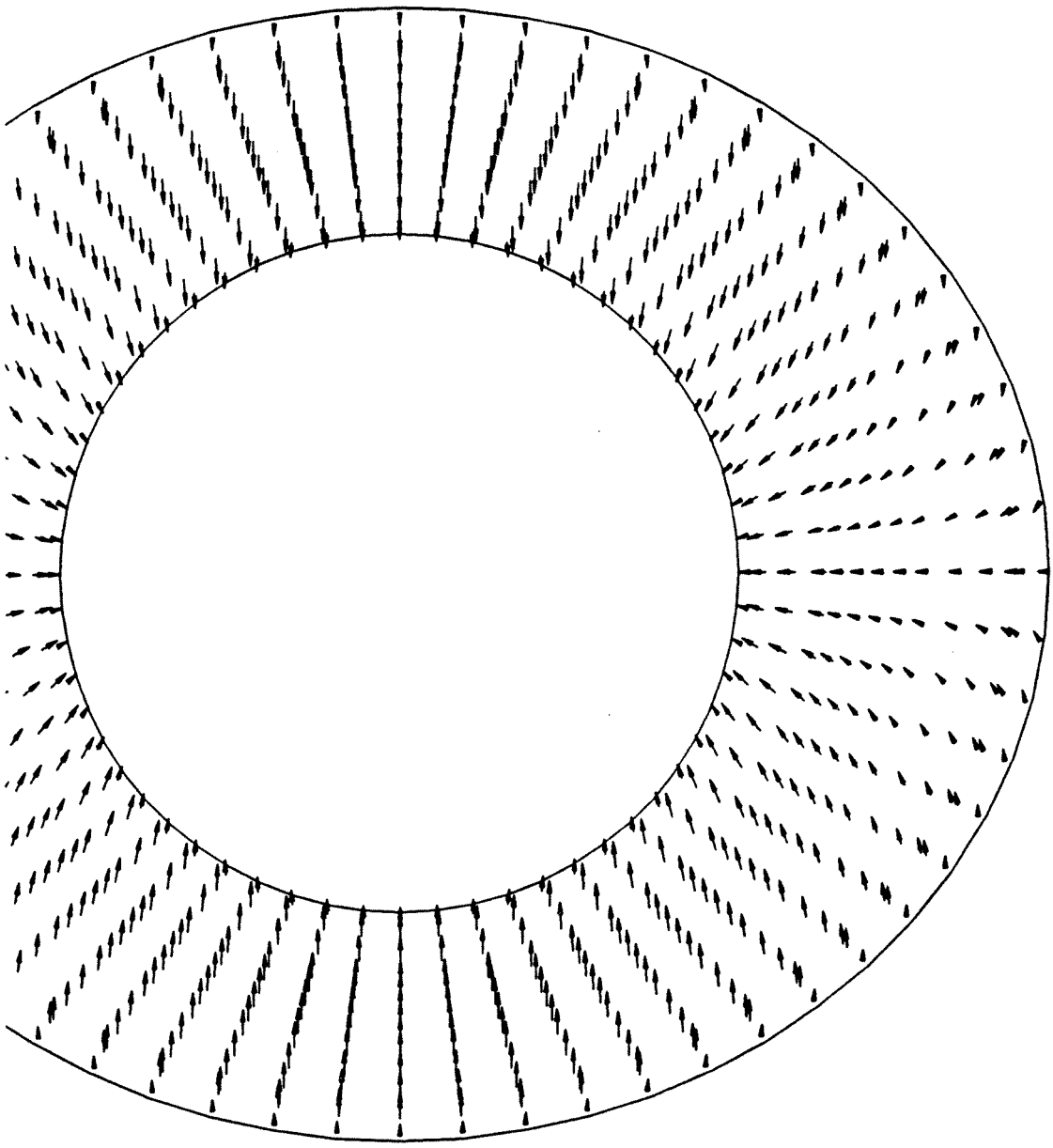

Figure 5.3: Cross-flow Velocity at Station 14, No Swirl Case

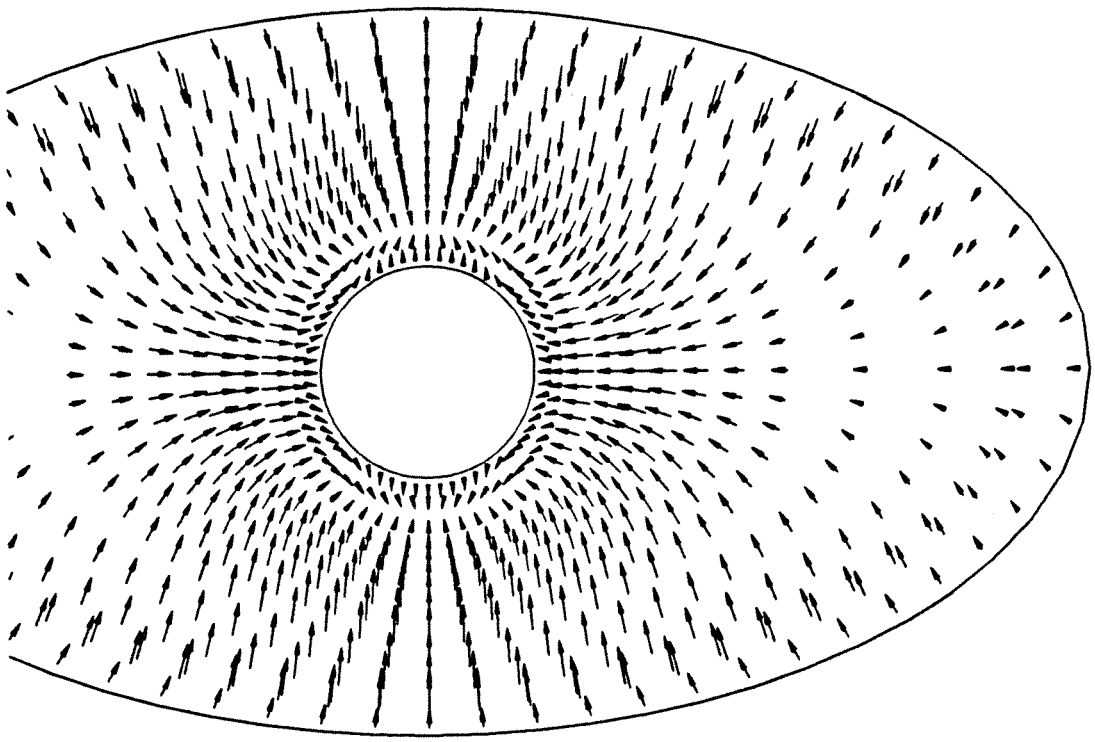

Figure 5.4: Cross-flow Velocity at Station 20, No Swirl Case

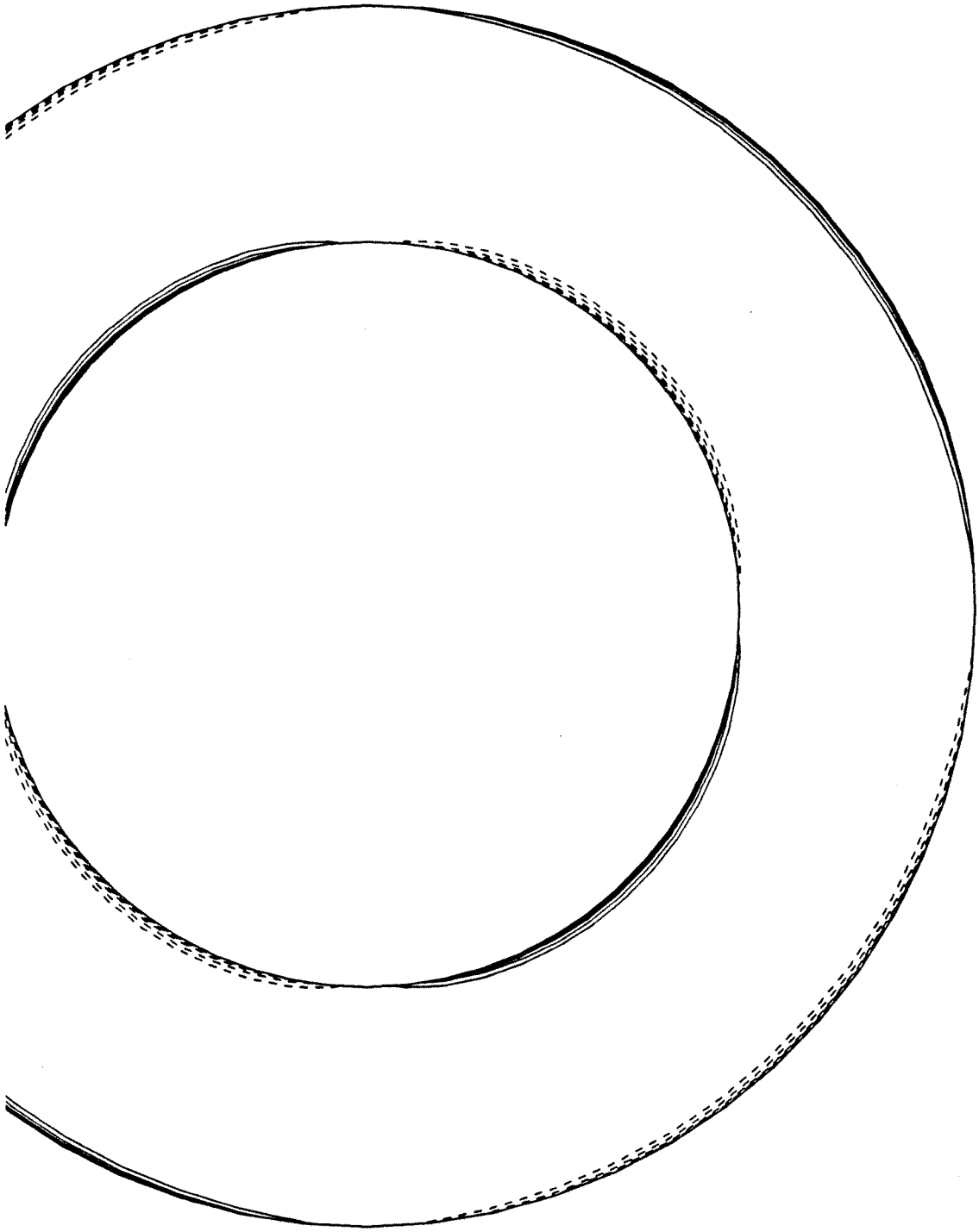

Figure 5.5: Axial Vorticity Contours at Station 6, No Swirl Case

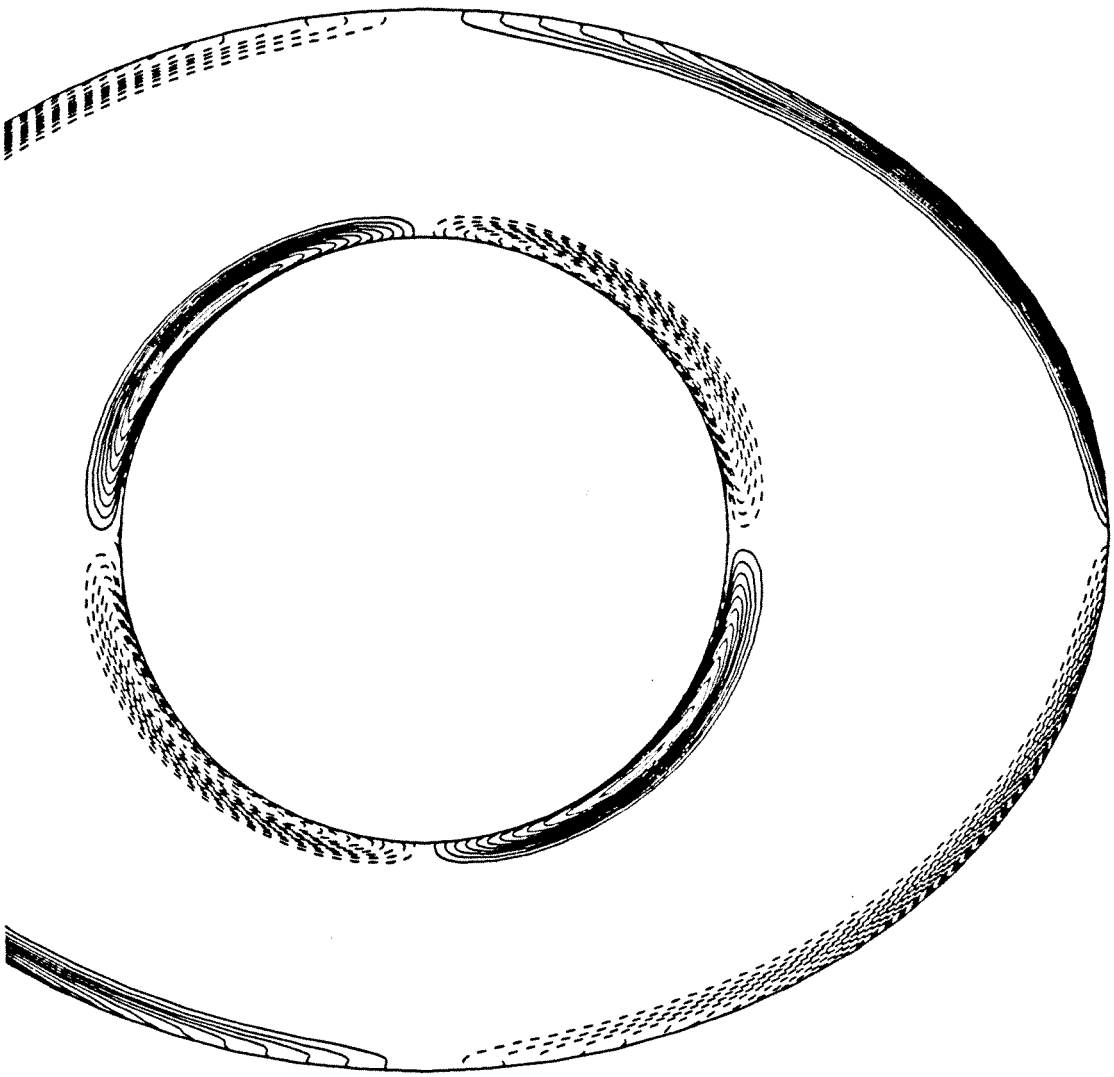

Figure 5.6: Axial Vorticity Contours at Station 16, No Swirl Case

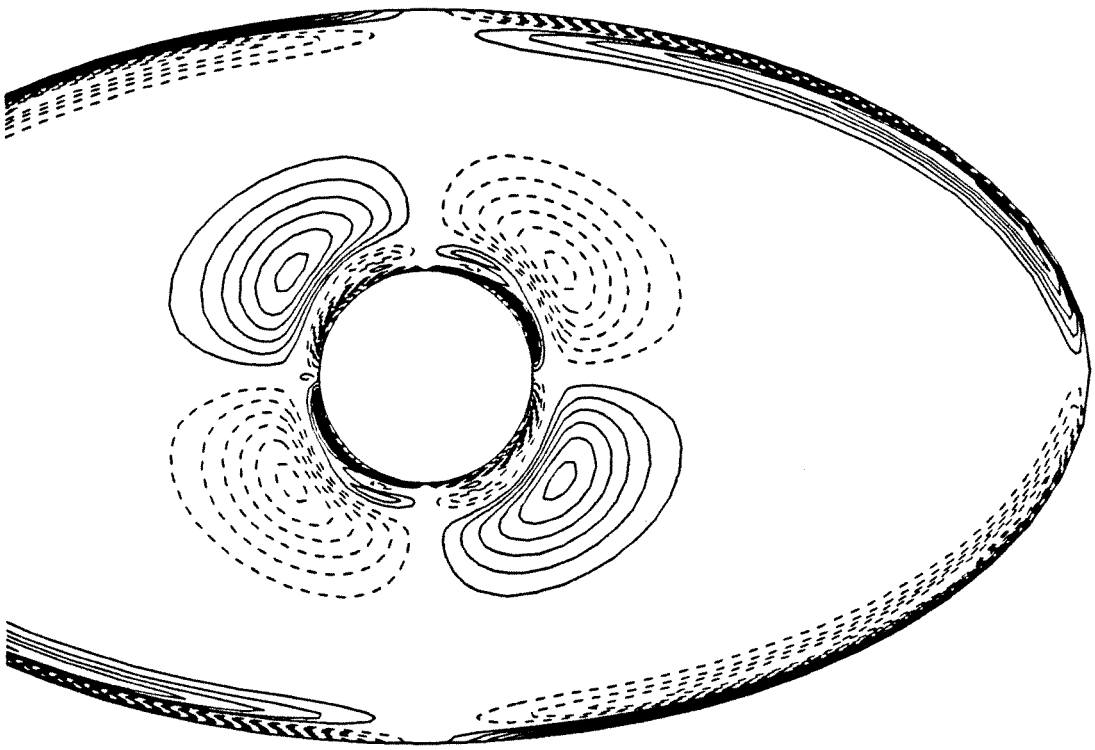

Figure 5.7: Axial Vorticity Contours at Station 20, No Swirl Case

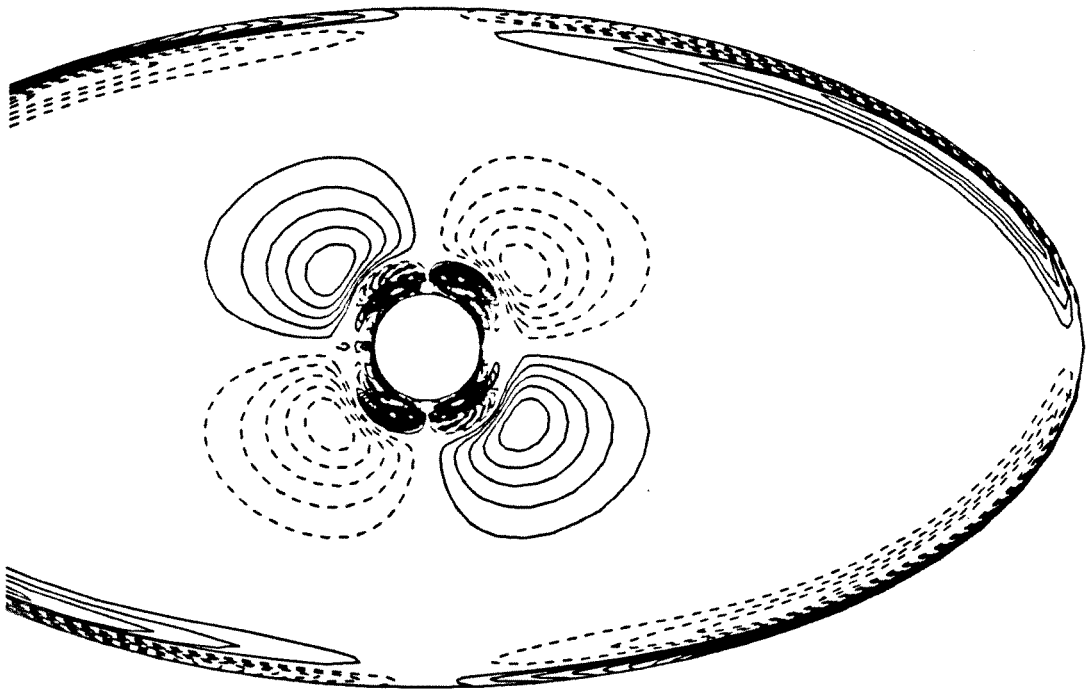

Figure 5.8: Axial Vorticity Contours at Station 21, No Swirl Case

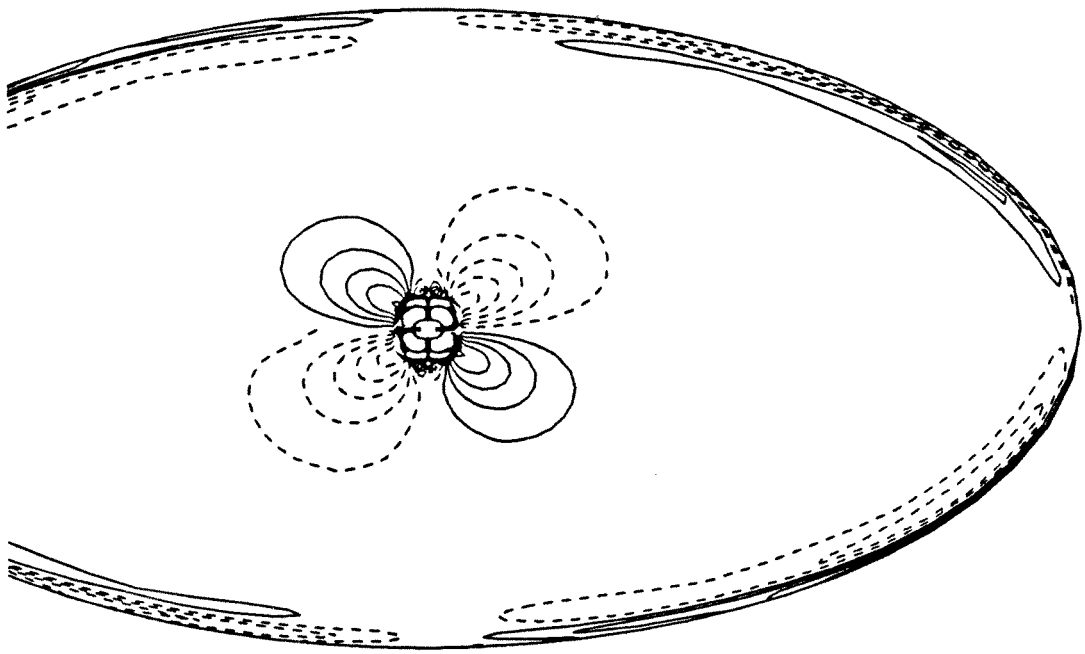

Figure 5.9: Axial Vorticity Contours at Station 22, No Swirl Case

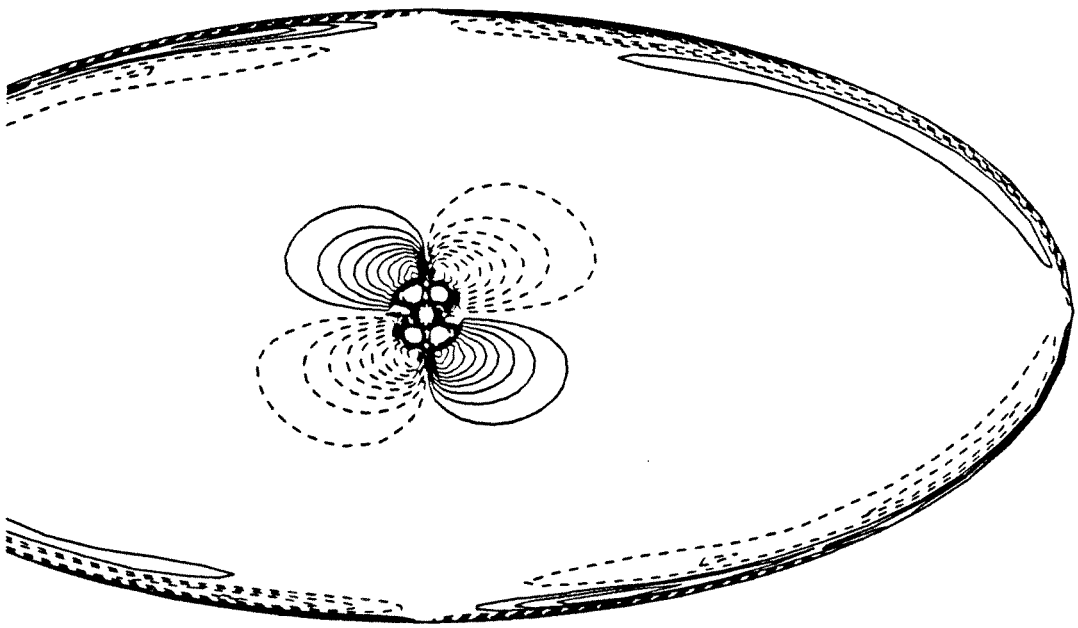

Figure 5.10: Axial Vorticity Contours at Station 23, No Swirl Case

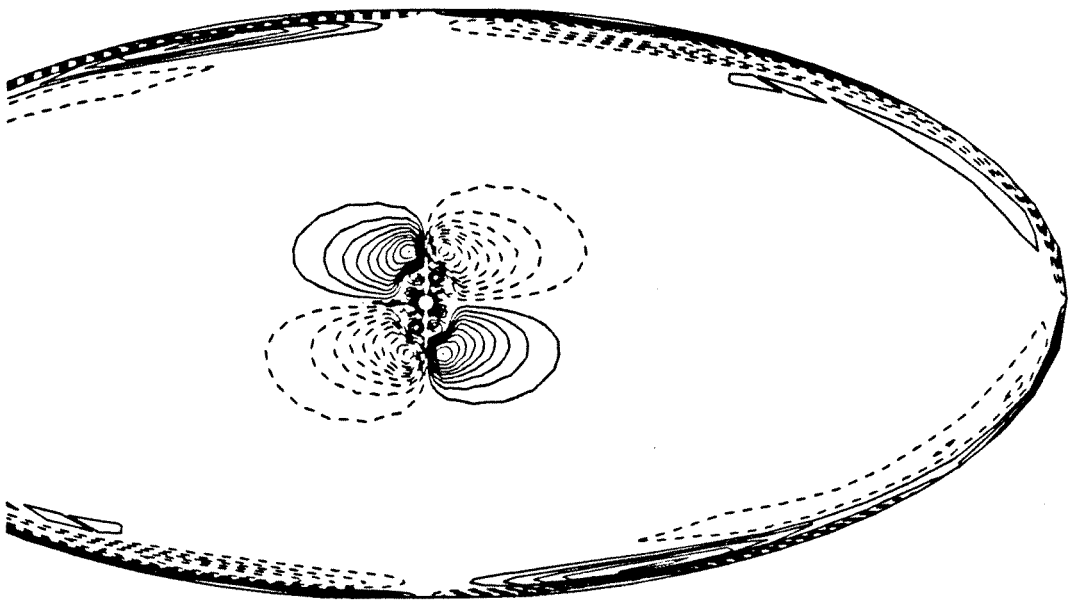

Figure 5.11: Axial Vorticity Contours at Station 24, No Swirl Case

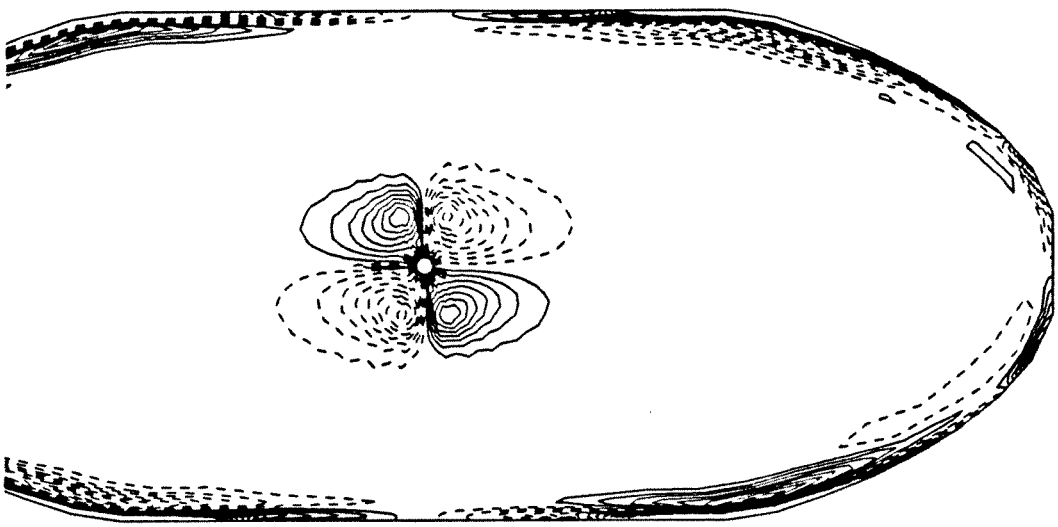

Figure 5.12: Axial Vorticity Contours at Station 26, No Swirl Case

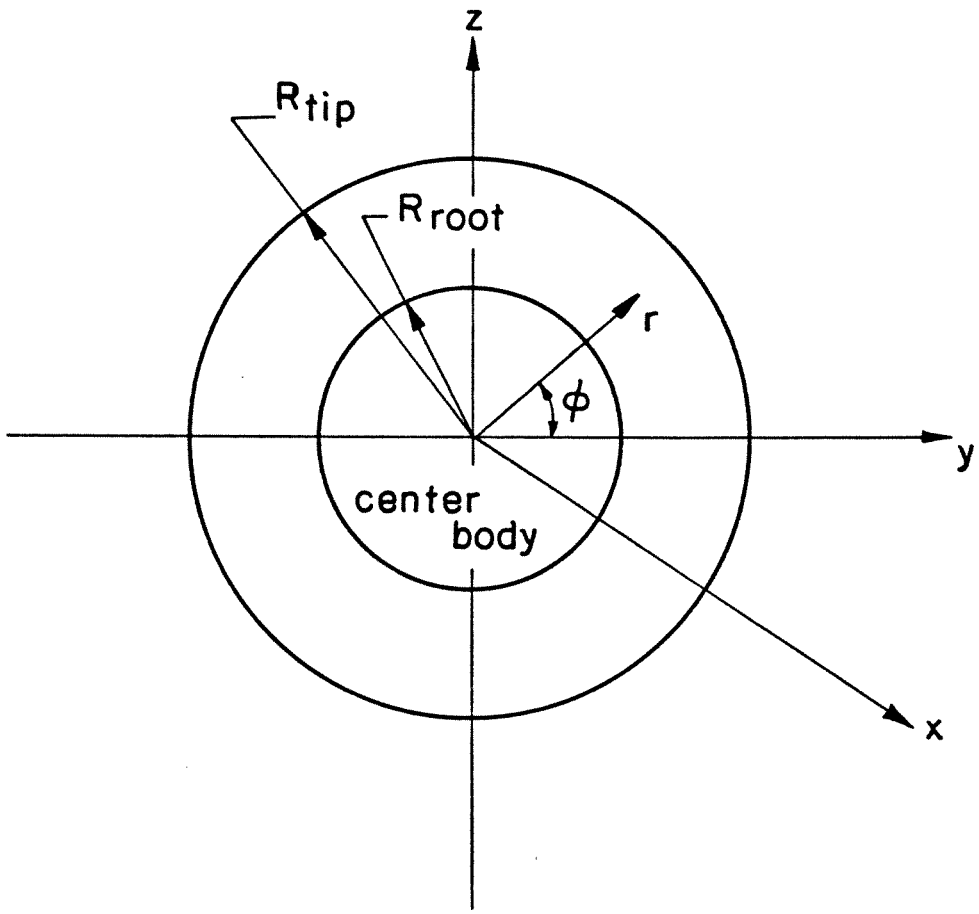

Figure 5.13: Coordinate System at Inlet

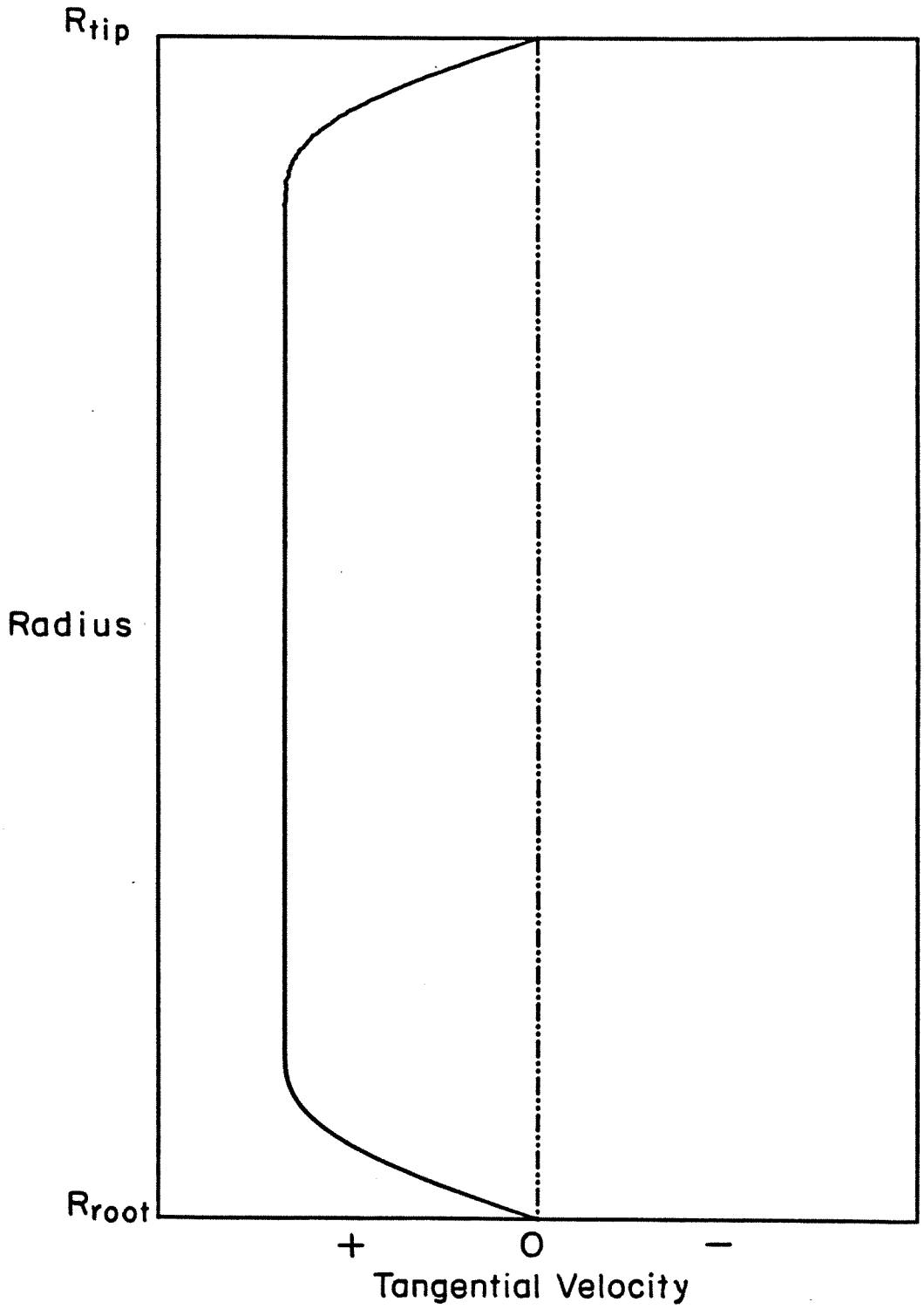

Figure 5.14: Approximate Tangential Velocity Profile

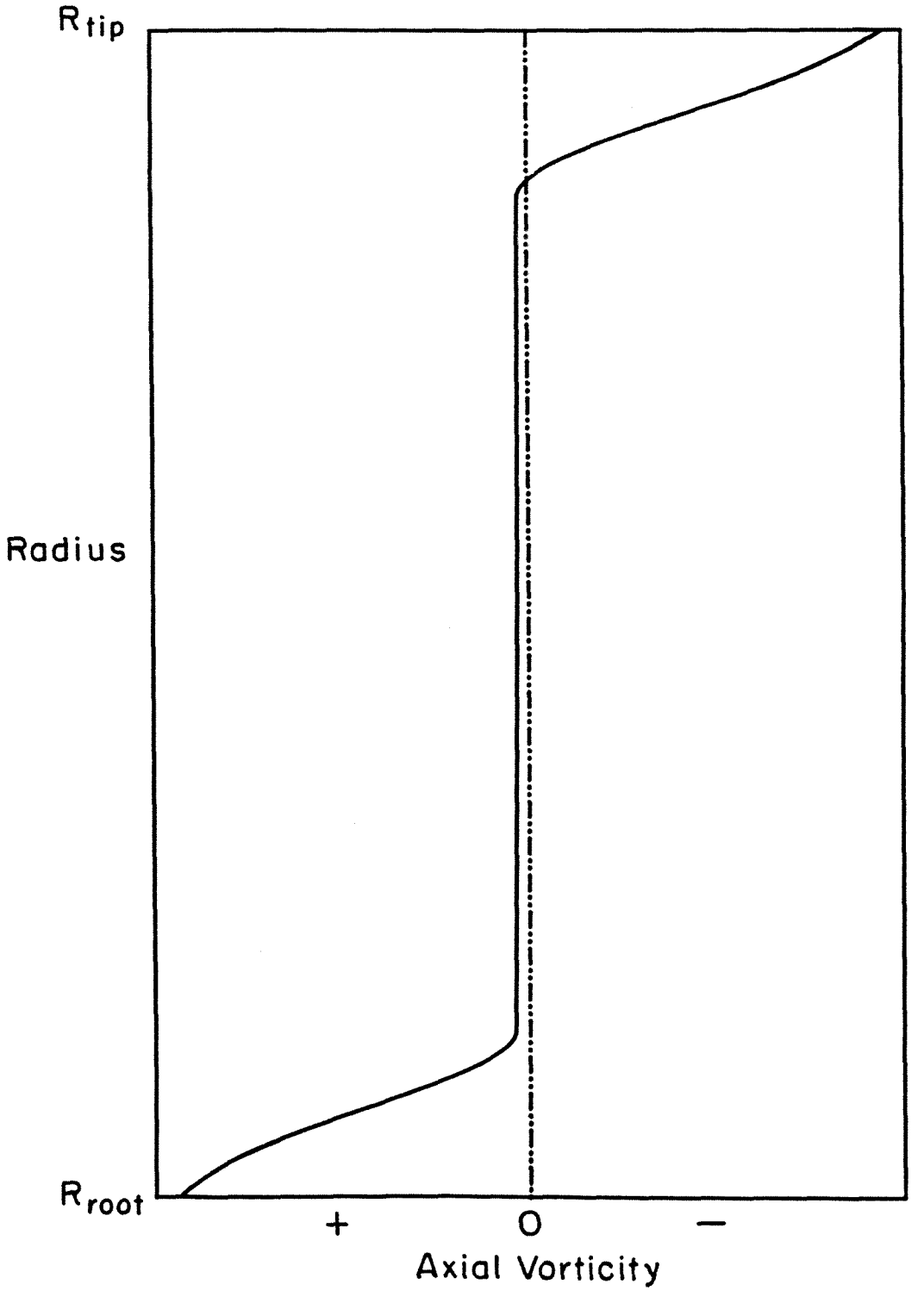

Figure 5.15: Approximate Axial Vorticity Profile

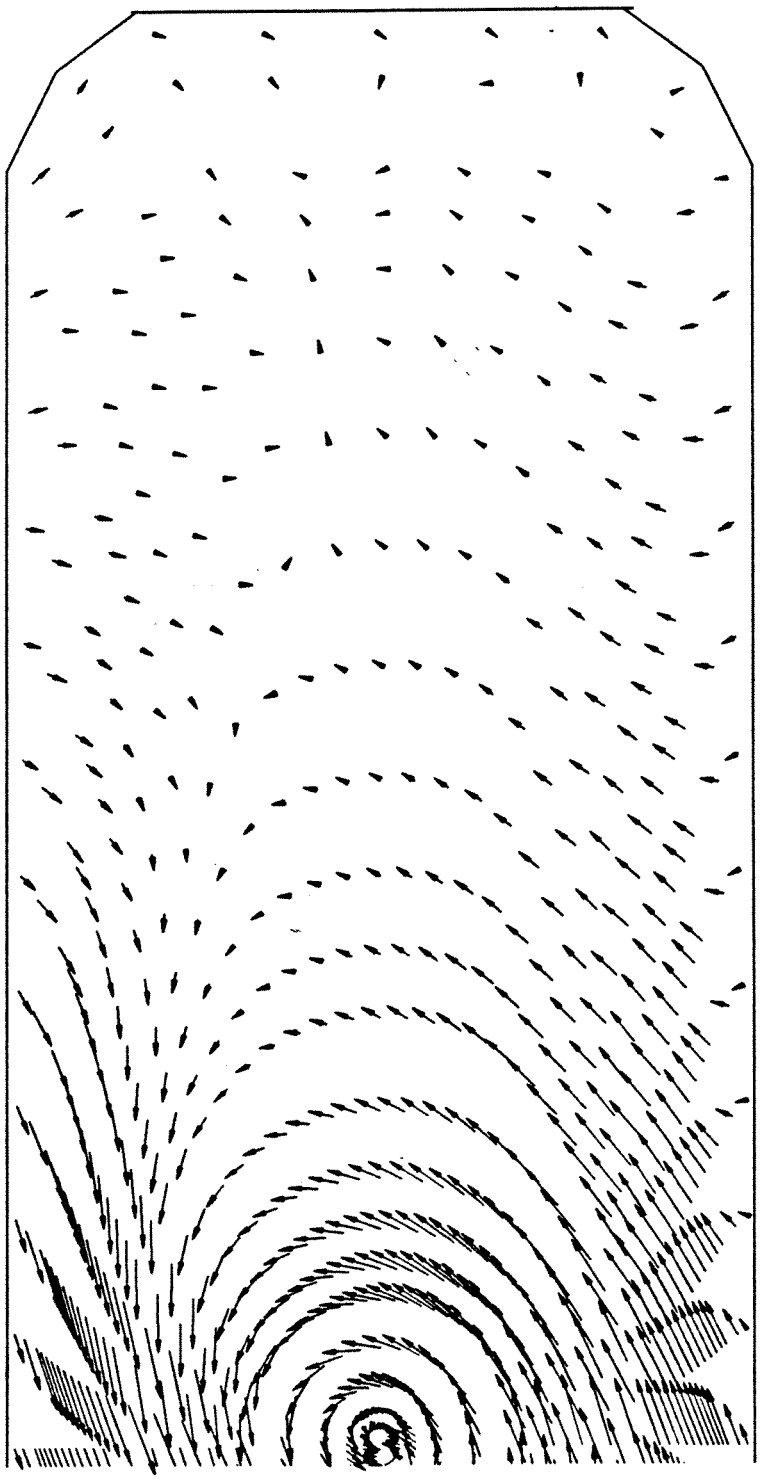

Figure 5.16: Cross–flow Velocity at Station 32, Low Swirl Case

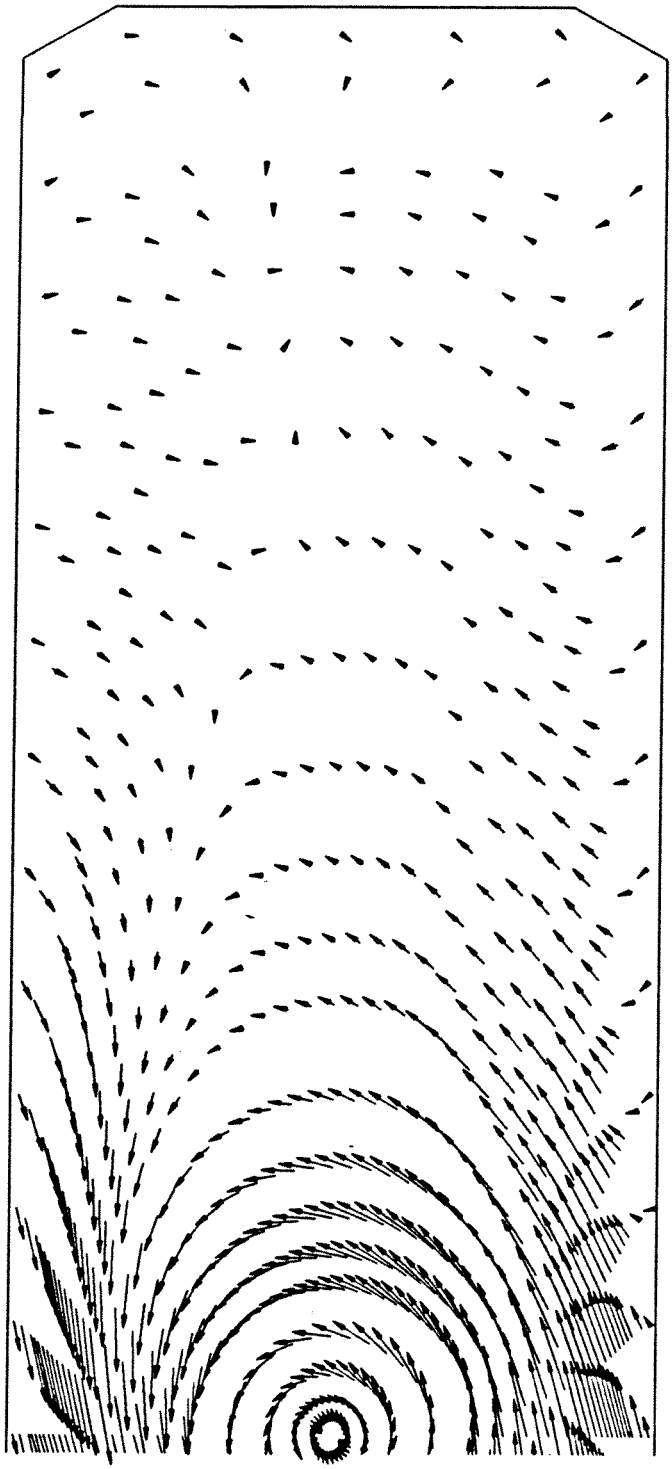

Figure 5.17: Cross–flow Velocity at Station 34, Low Swirl Case

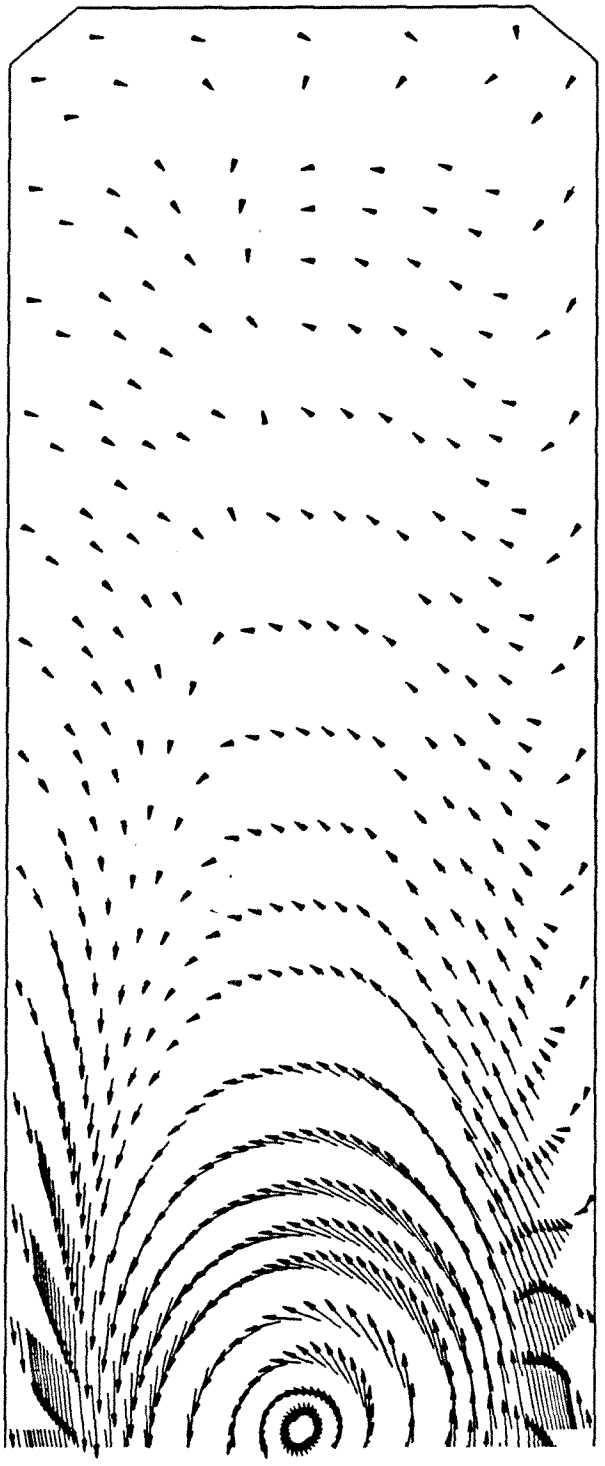

Figure 5.18: Cross-flow Velocity at Station 36, Low Swirl Case

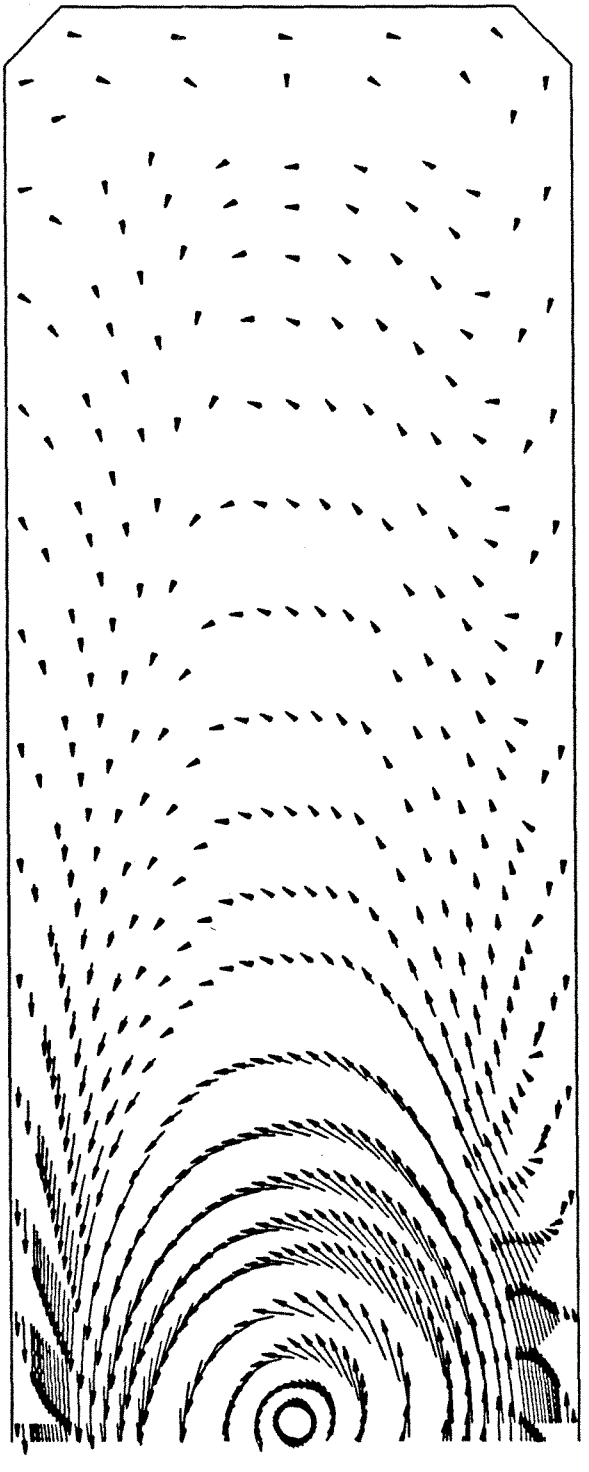

Figure 5.19: Cross–flow Velocity at Station 38, Low Swirl Case

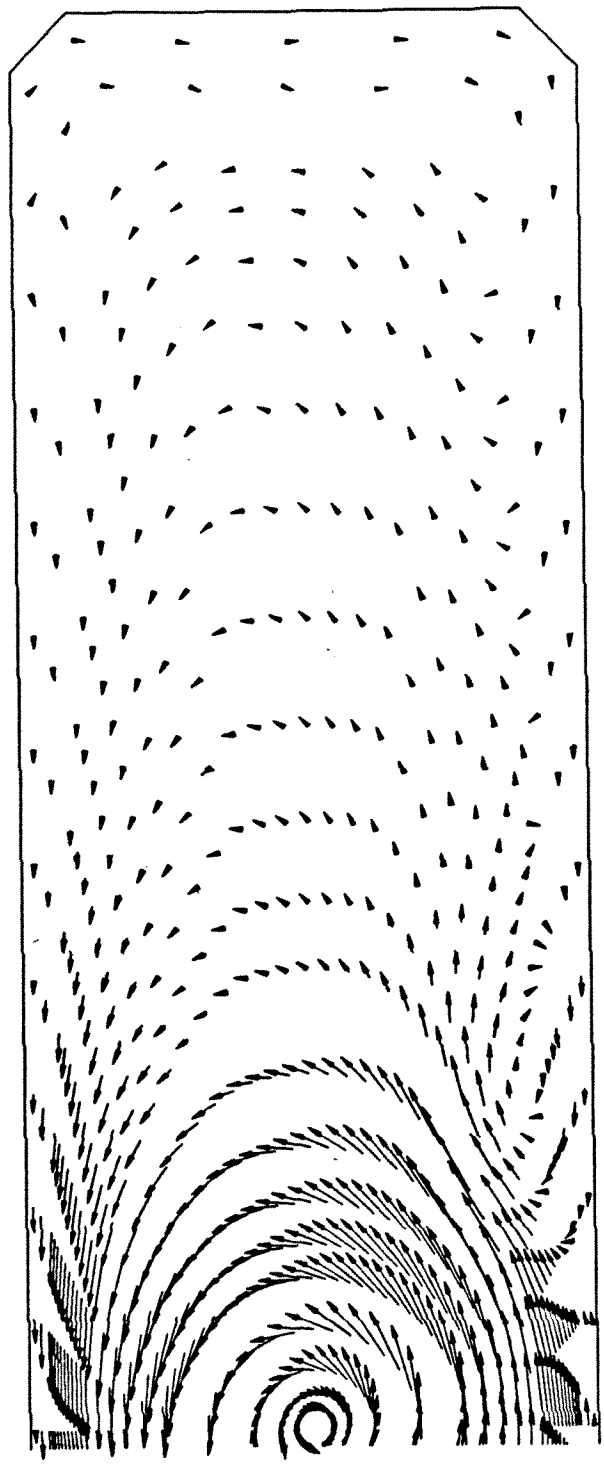

Figure 5.20: Cross–flow Velocity at Station 40, Low Swirl Case

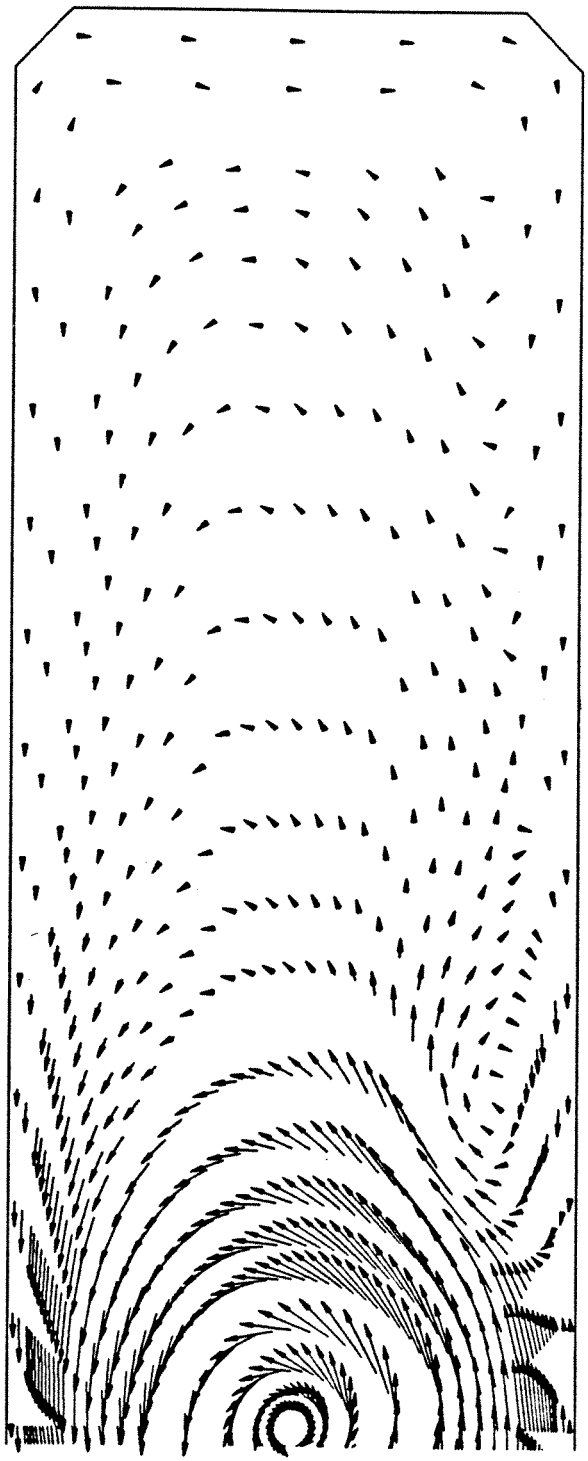

Figure 5.21: Cross–flow Velocity at Station 42, Low Swirl Case

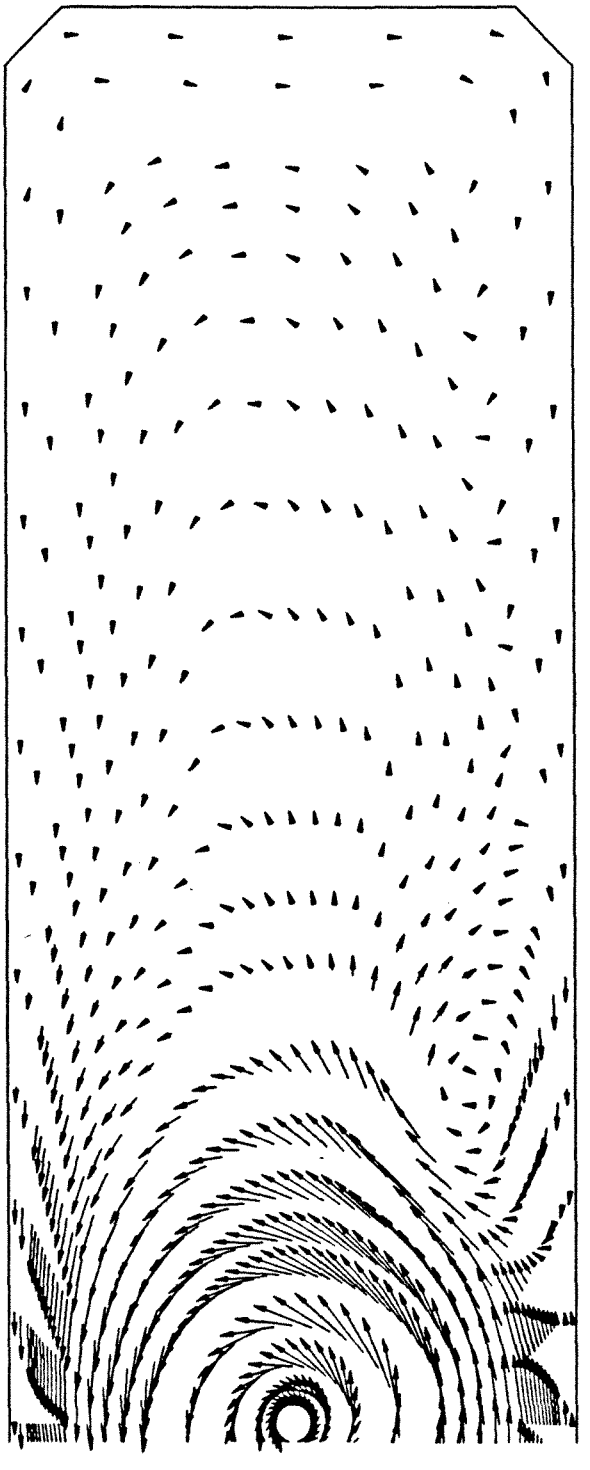

Figure 5.22: Cross–flow Velocity at Station 44, Low Swirl Case

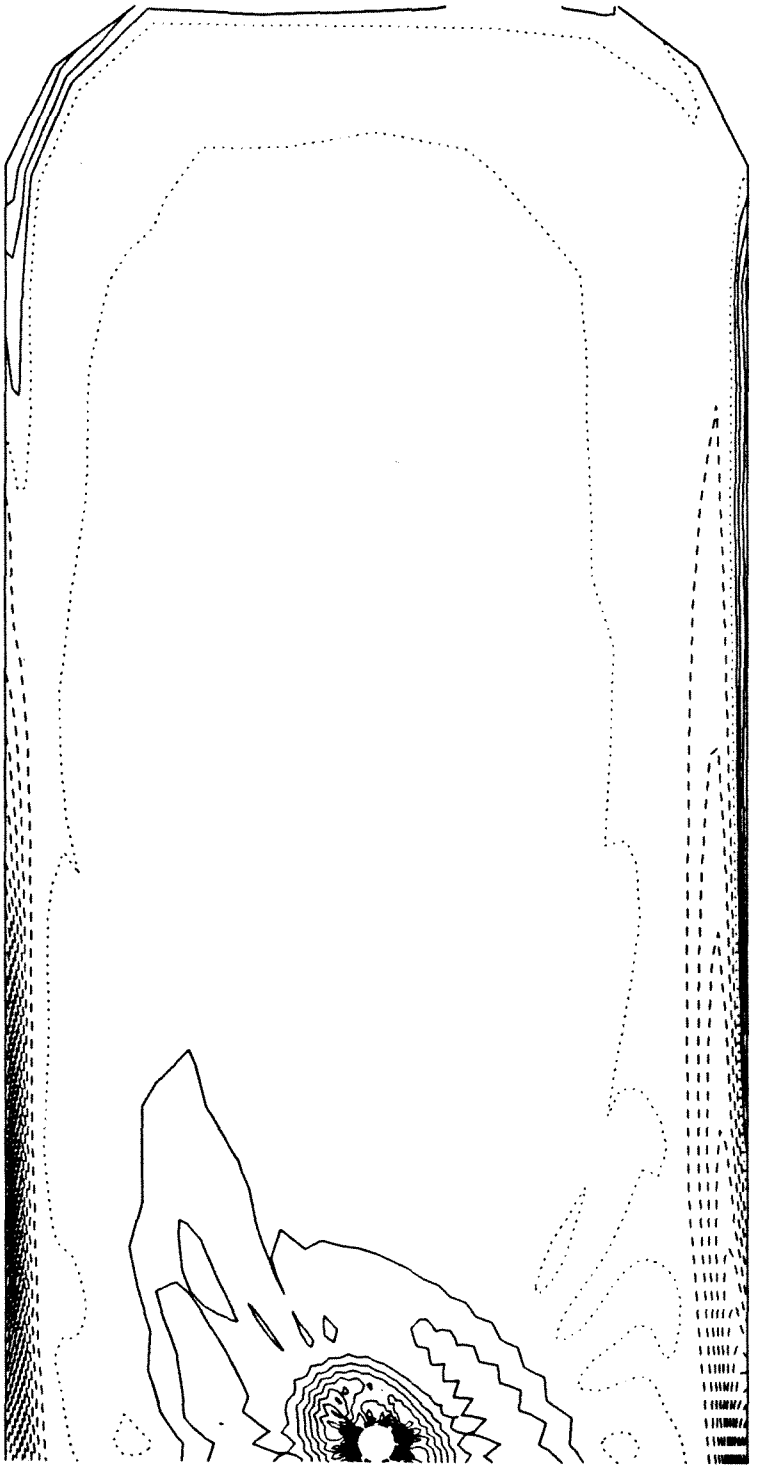

Figure 5.23: Axial Vorticity Contours at Station 32, Low Swirl Case

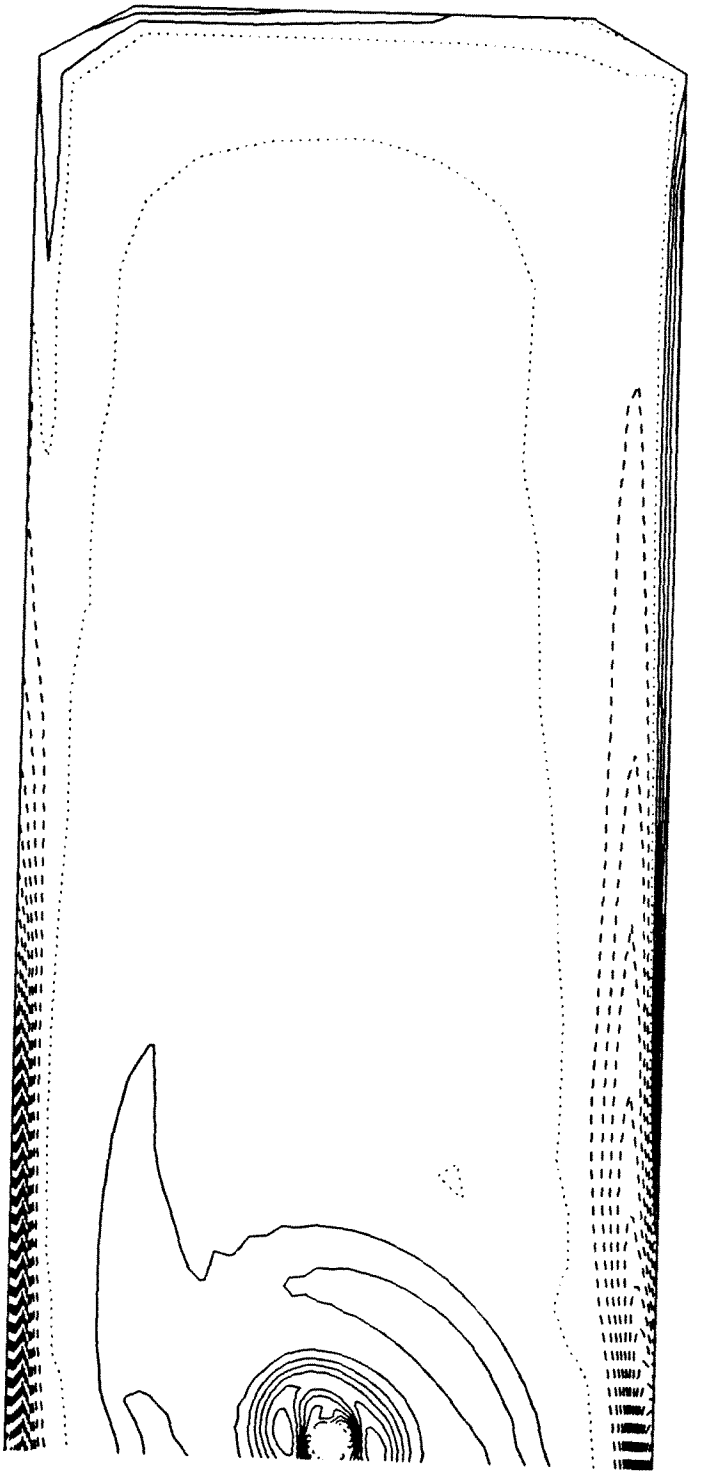

Figure 5.24: Axial Vorticity Contours at Station 34, Low Swirl Case

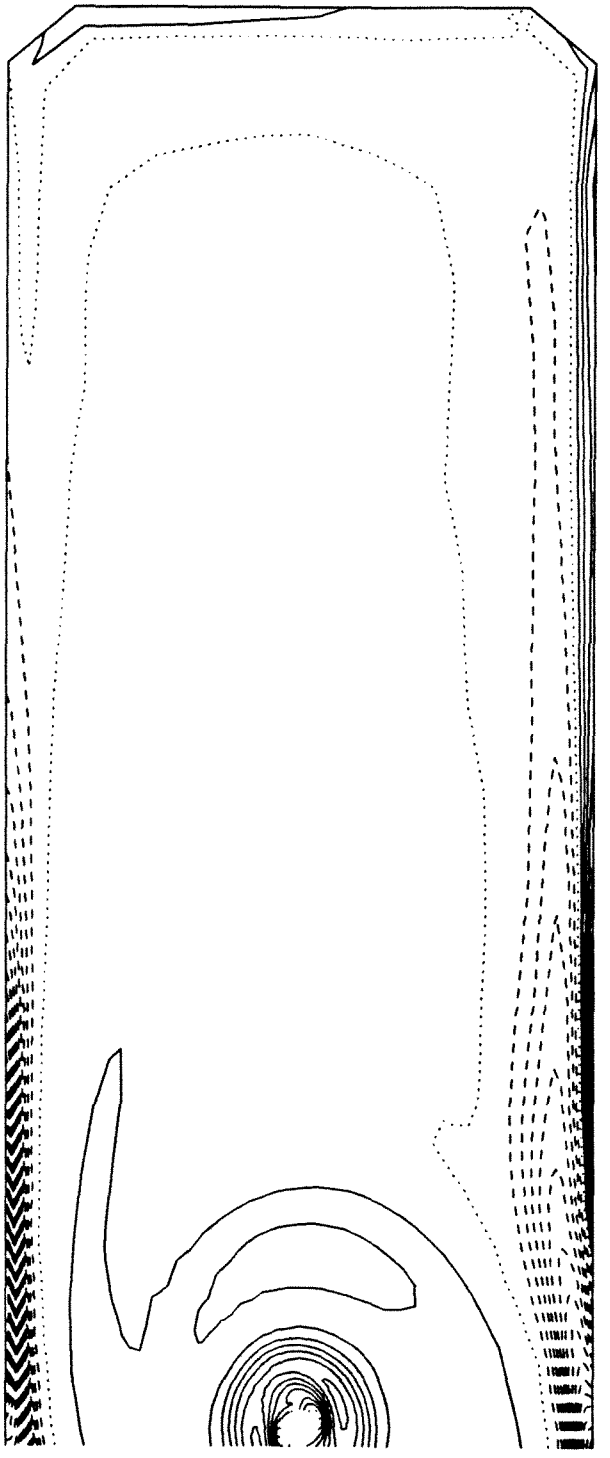

Figure 5.25: Axial Vorticity Contours at Station 36, Low Swirl Case

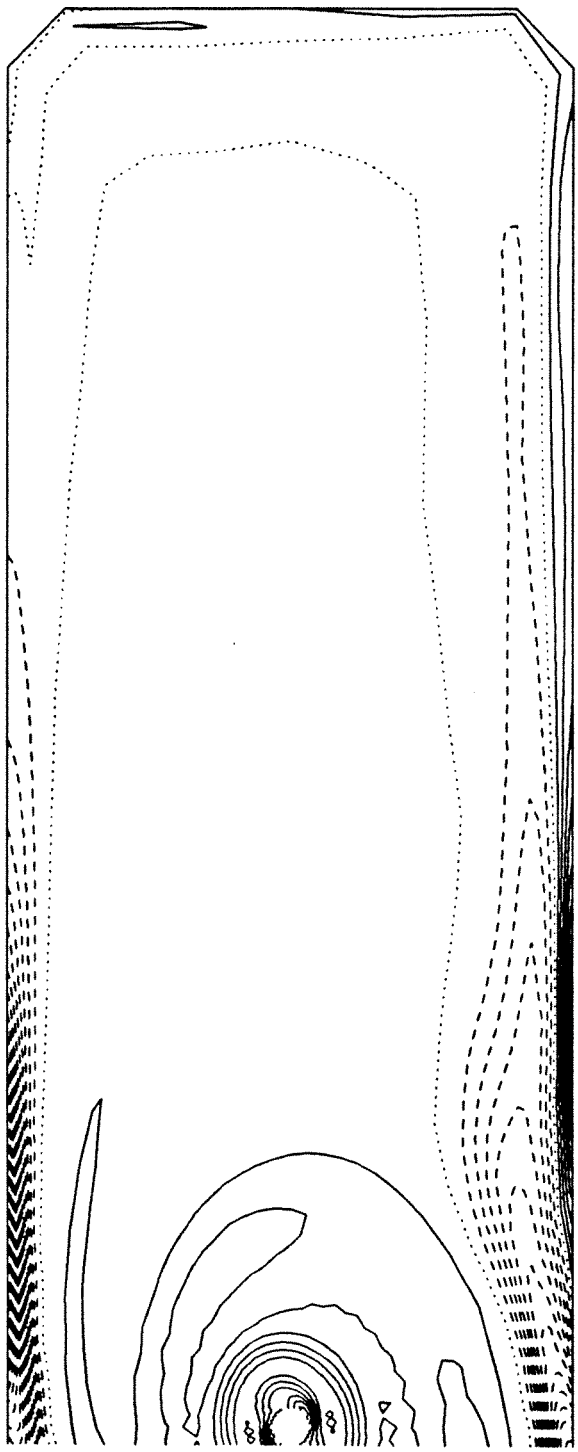

Figure 5.26: Axial Vorticity Contours at Station 38, Low Swirl Case

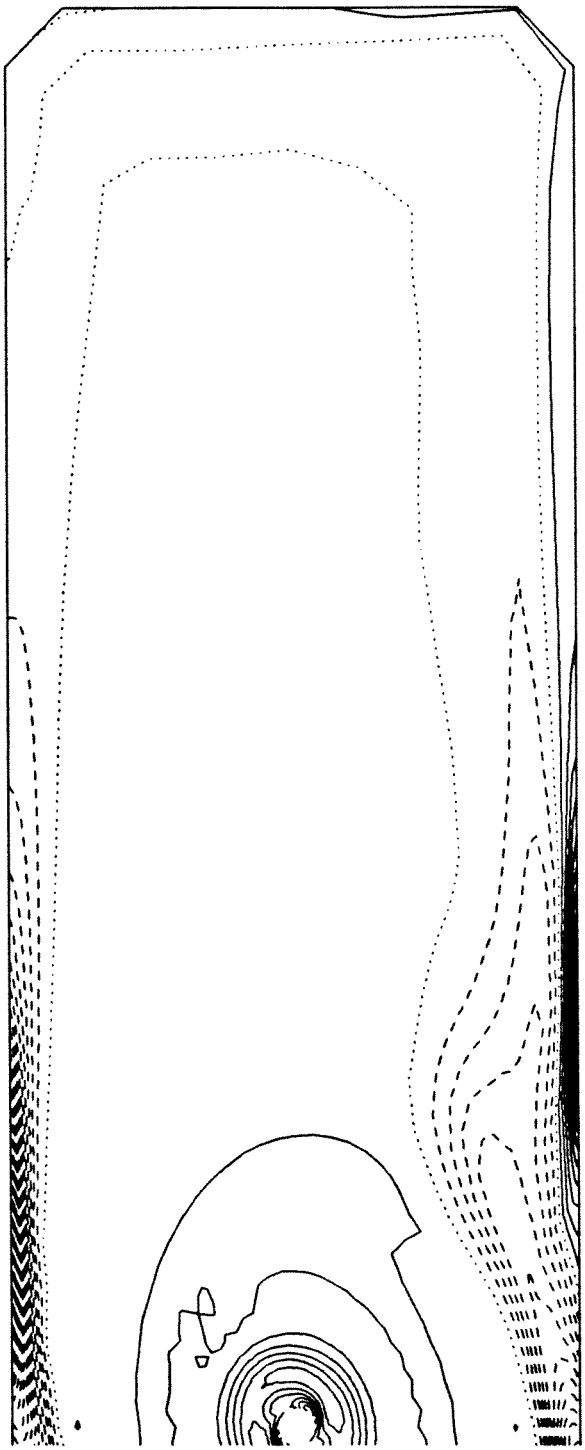

Figure 5.27: Axial Vorticity Contours at Station 40, Low Swirl Case

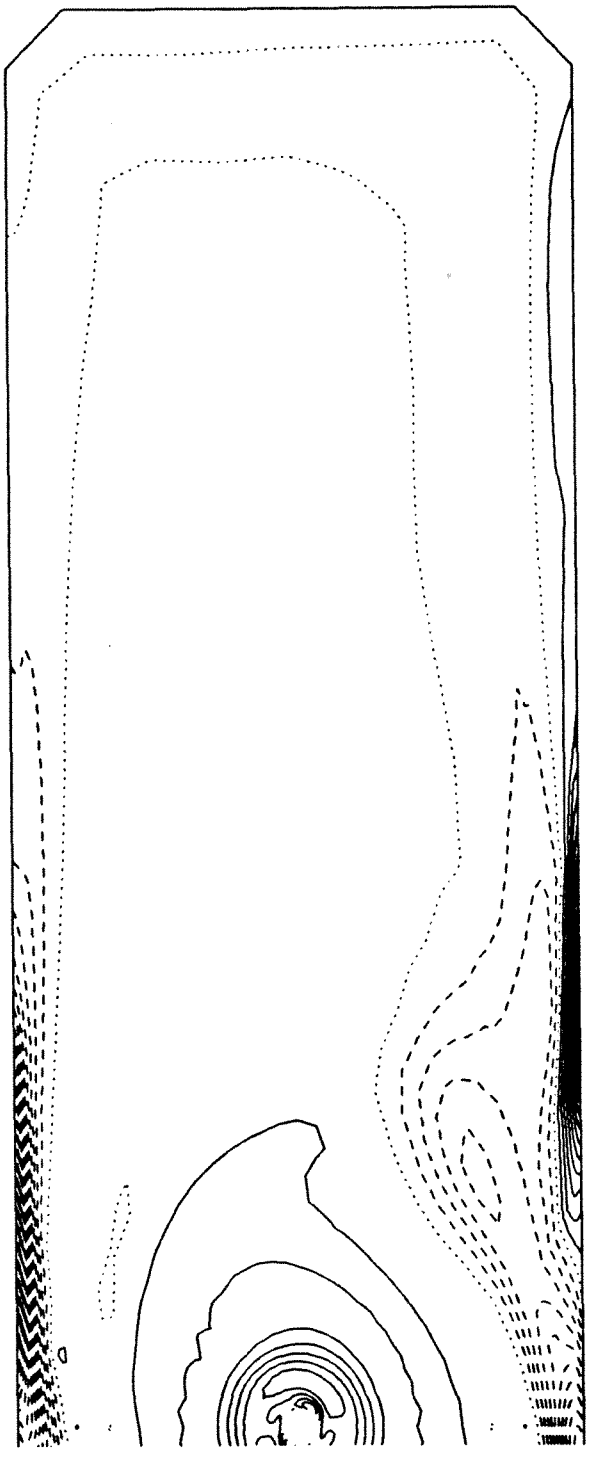

Figure 5.28: Axial Vorticity Contours at Station 42, Low Swirl Case

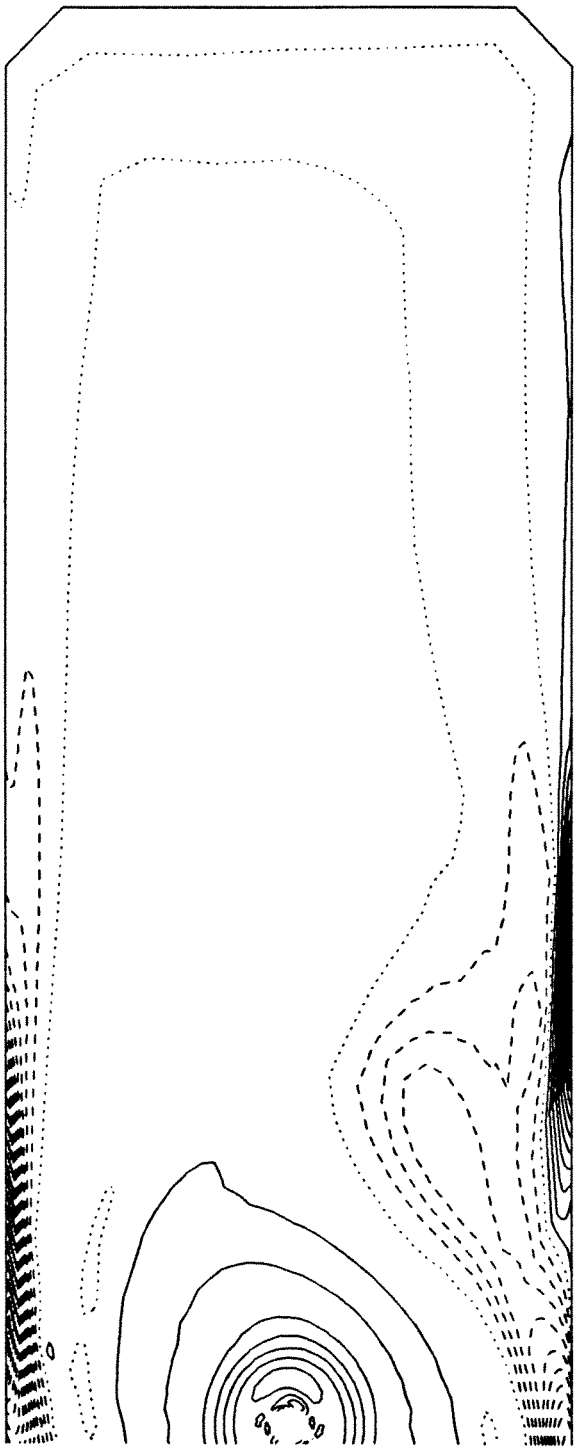

Figure 5.29: Axial Vorticity Contours at Station 44, Low Swirl Case

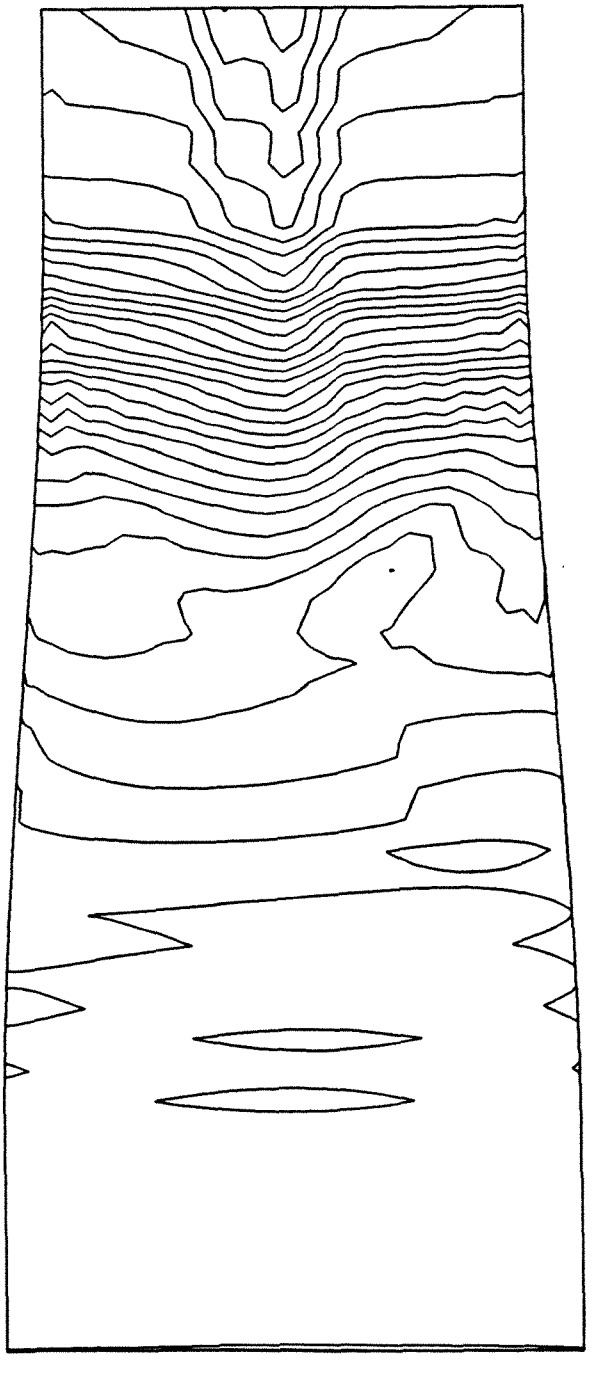

Figure 5.30: Iso–pressure Contours on Outer Wall, Low Swirl Case

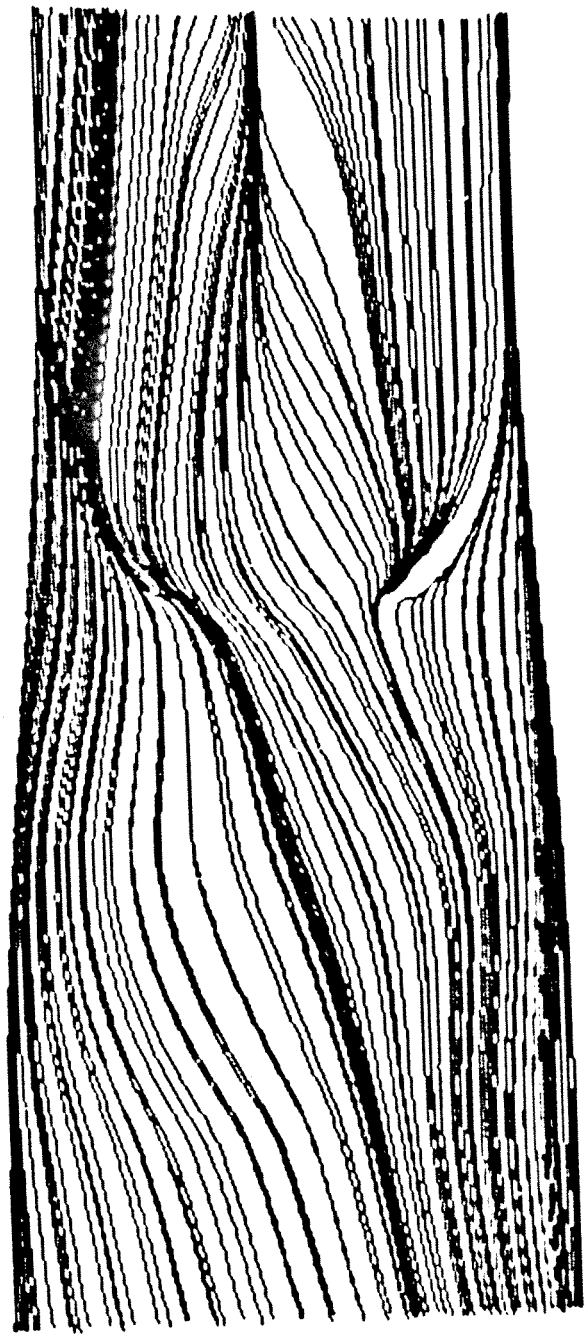

Figure 5.31: Limiting Streamlines on Outer Wall, Low Swirl Case

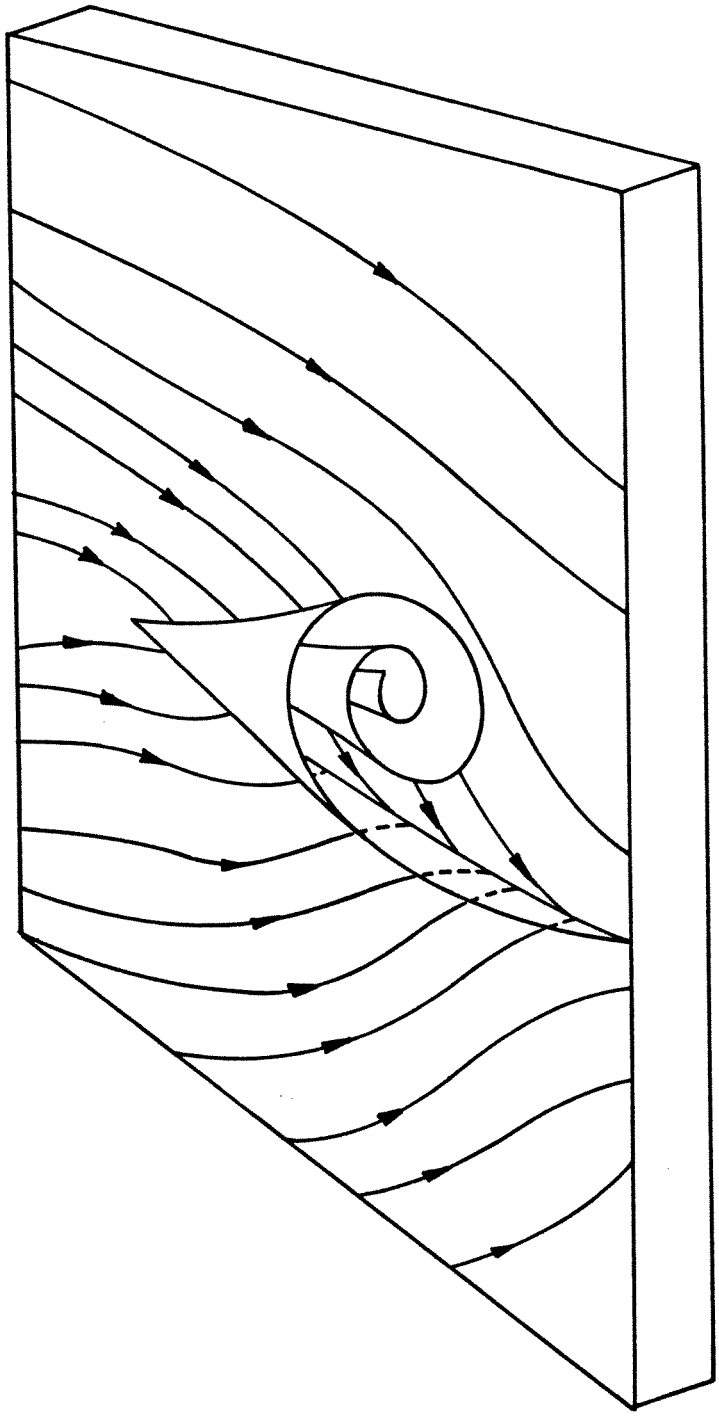

Figure 5.32: Schematic Representation of an Open Negative Surface Streamline Bifurcation

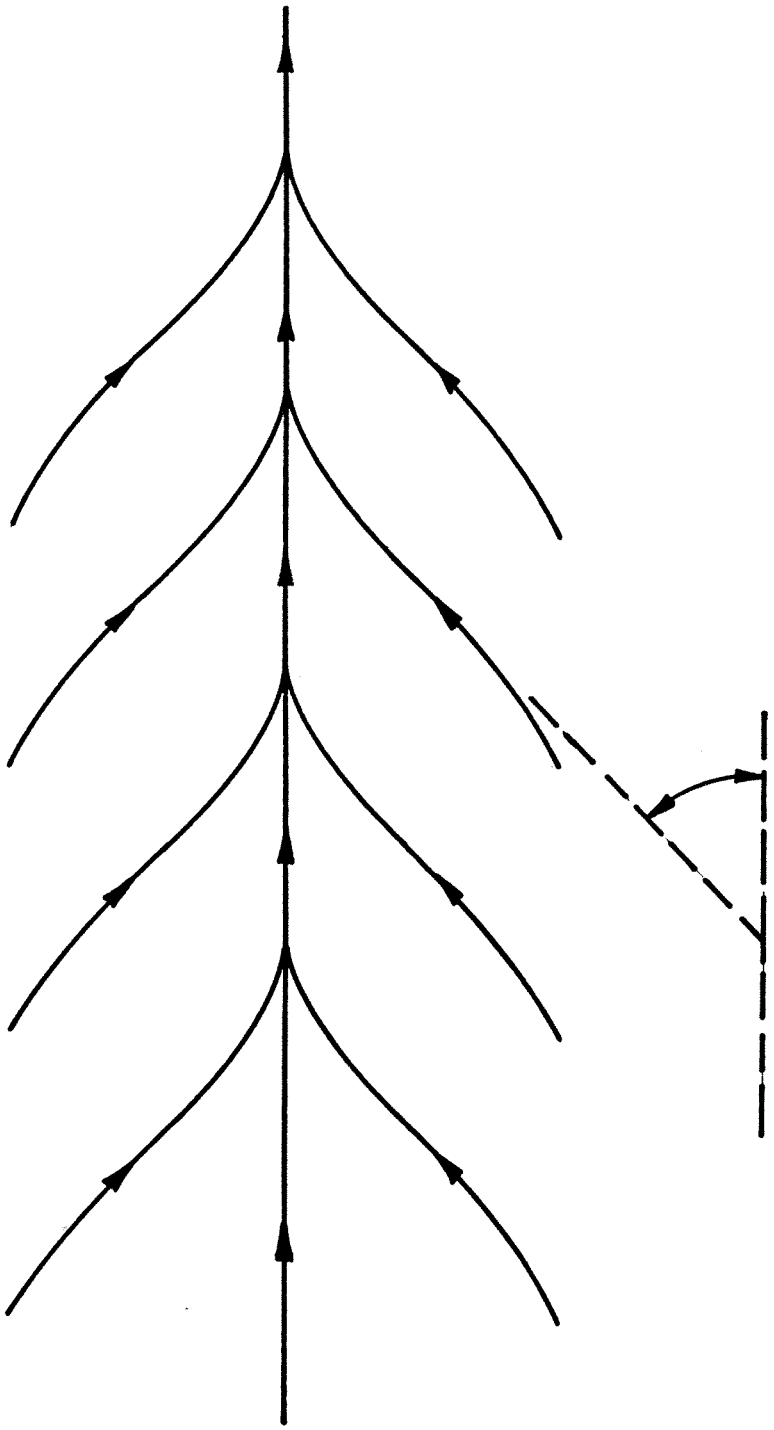

Figure 5.33: Strength of Wall Streamline Convergence

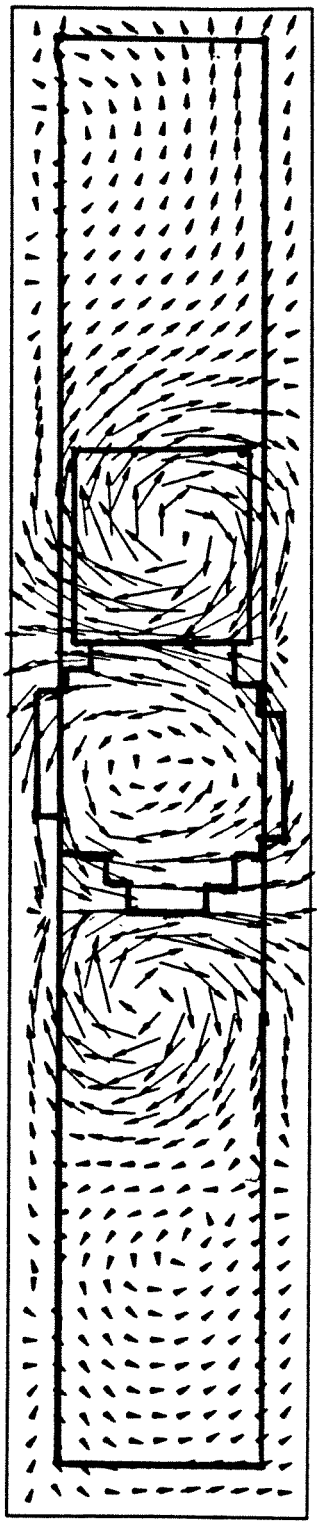

Figure 5.34: Contours of Integration for Circulation Integrals

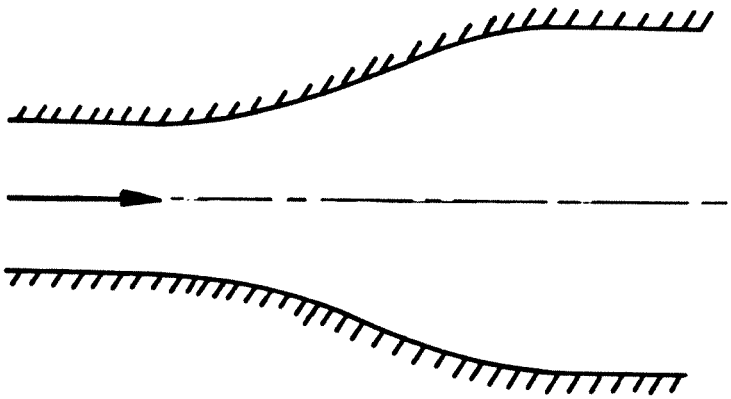

a) Increase in Outer Radius

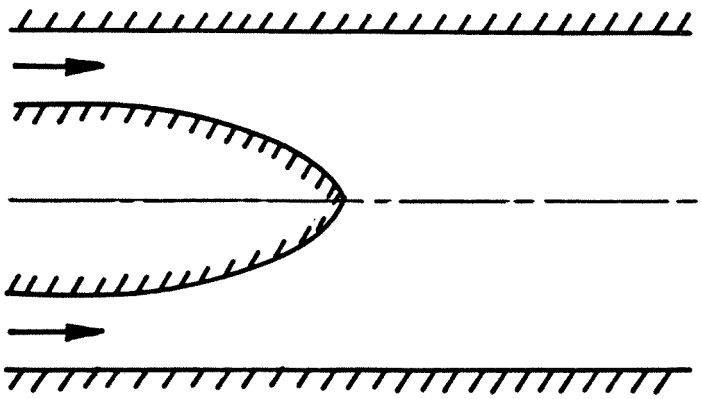

b) Vanishing Inner Radius

Figure 5.35: Axi-symmetric Transition Sections

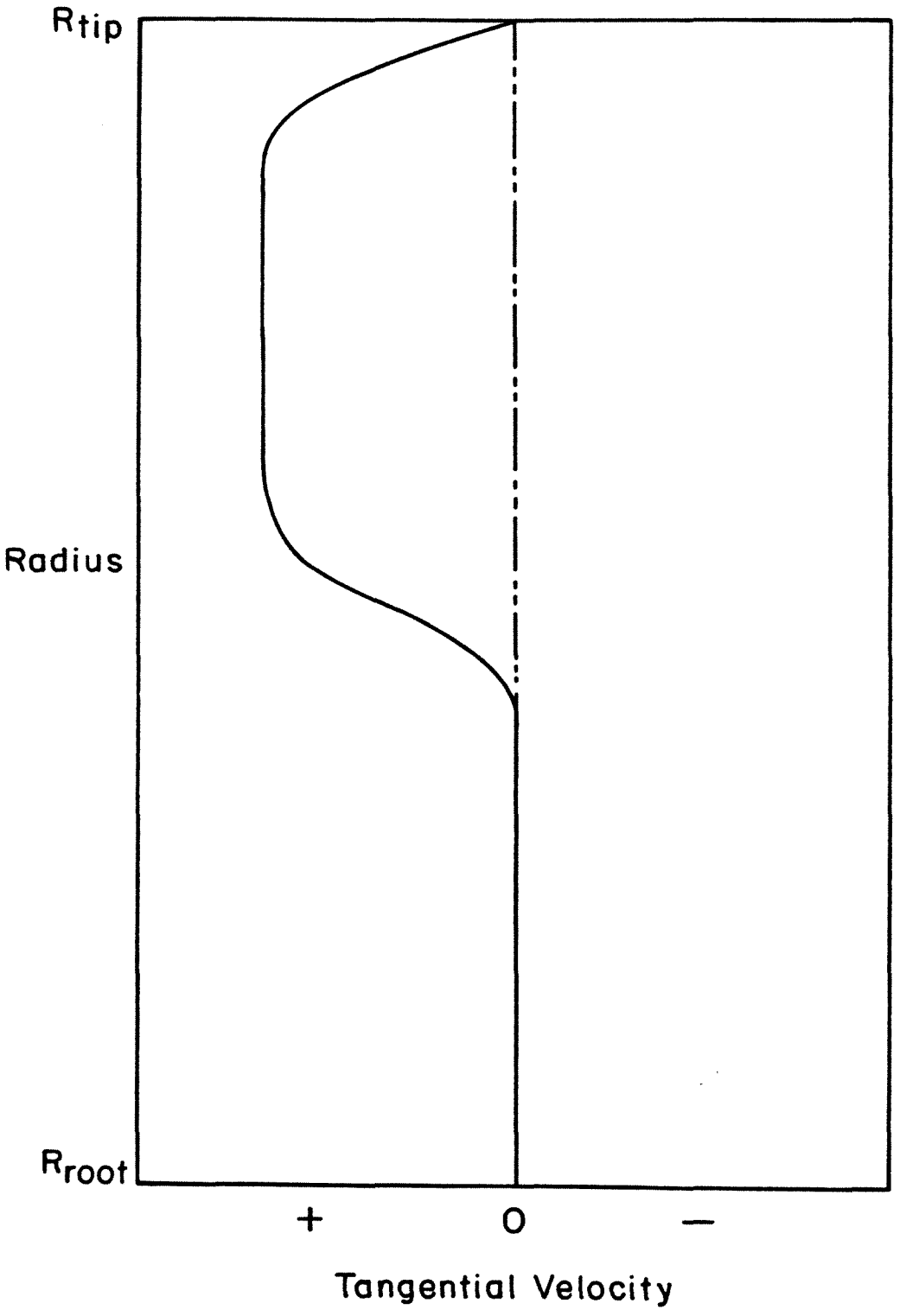

Figure 5.36: Approximate Tangential Velocity Profile

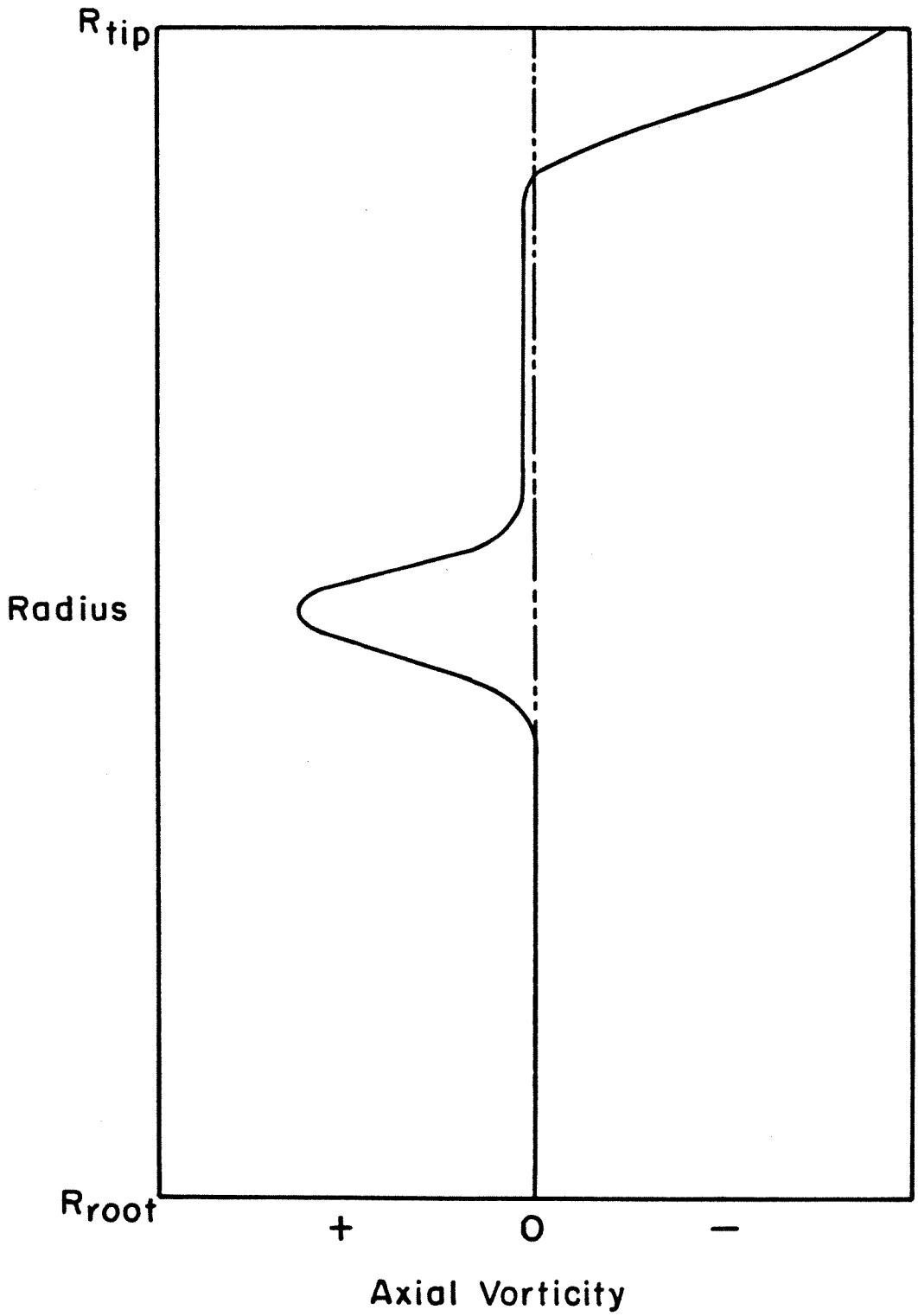

Figure 5.37: Approximate Axial Vorticity Profile

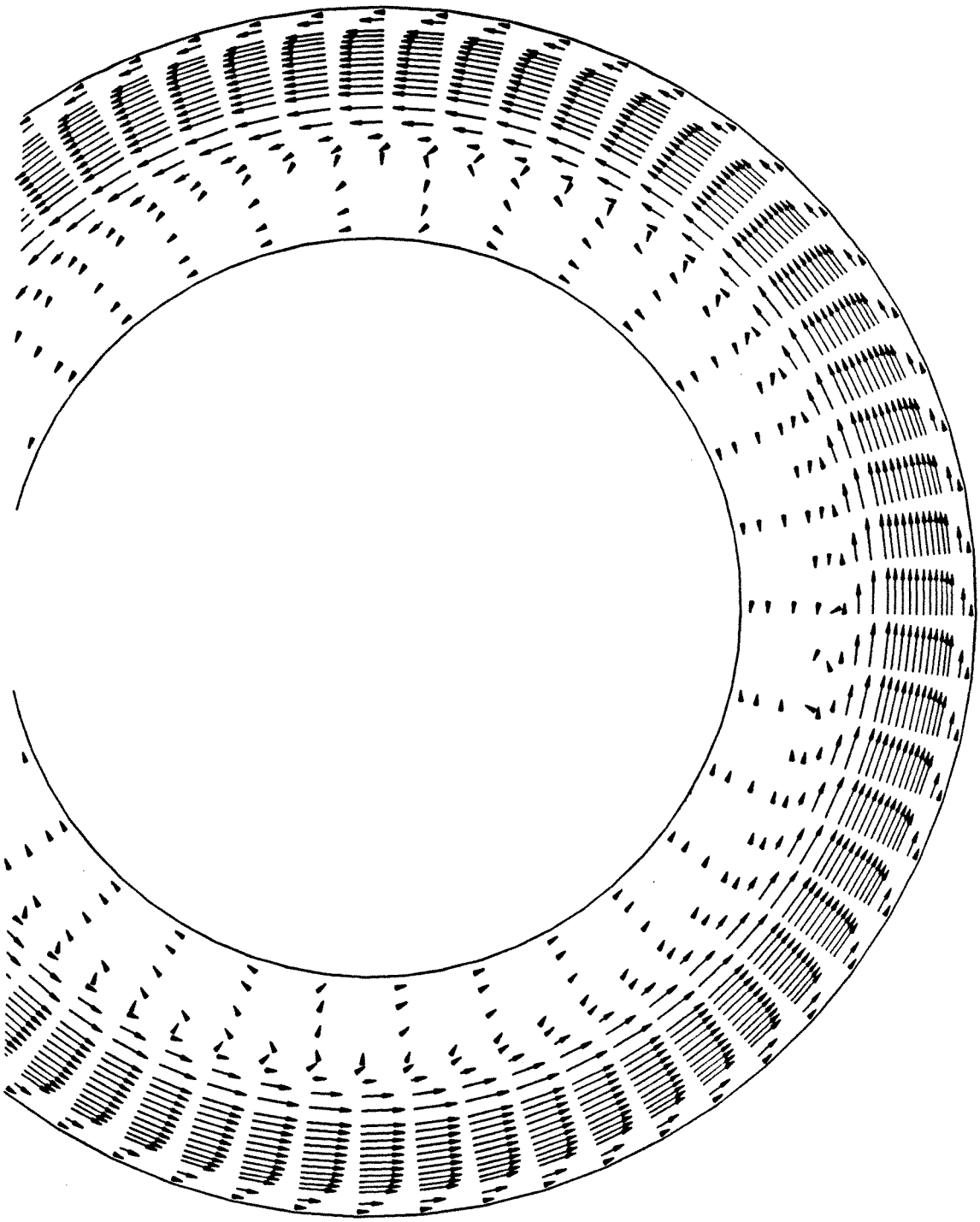

Figure 5.38: Cross-flow Velocity at Station 6, Split Blade Case

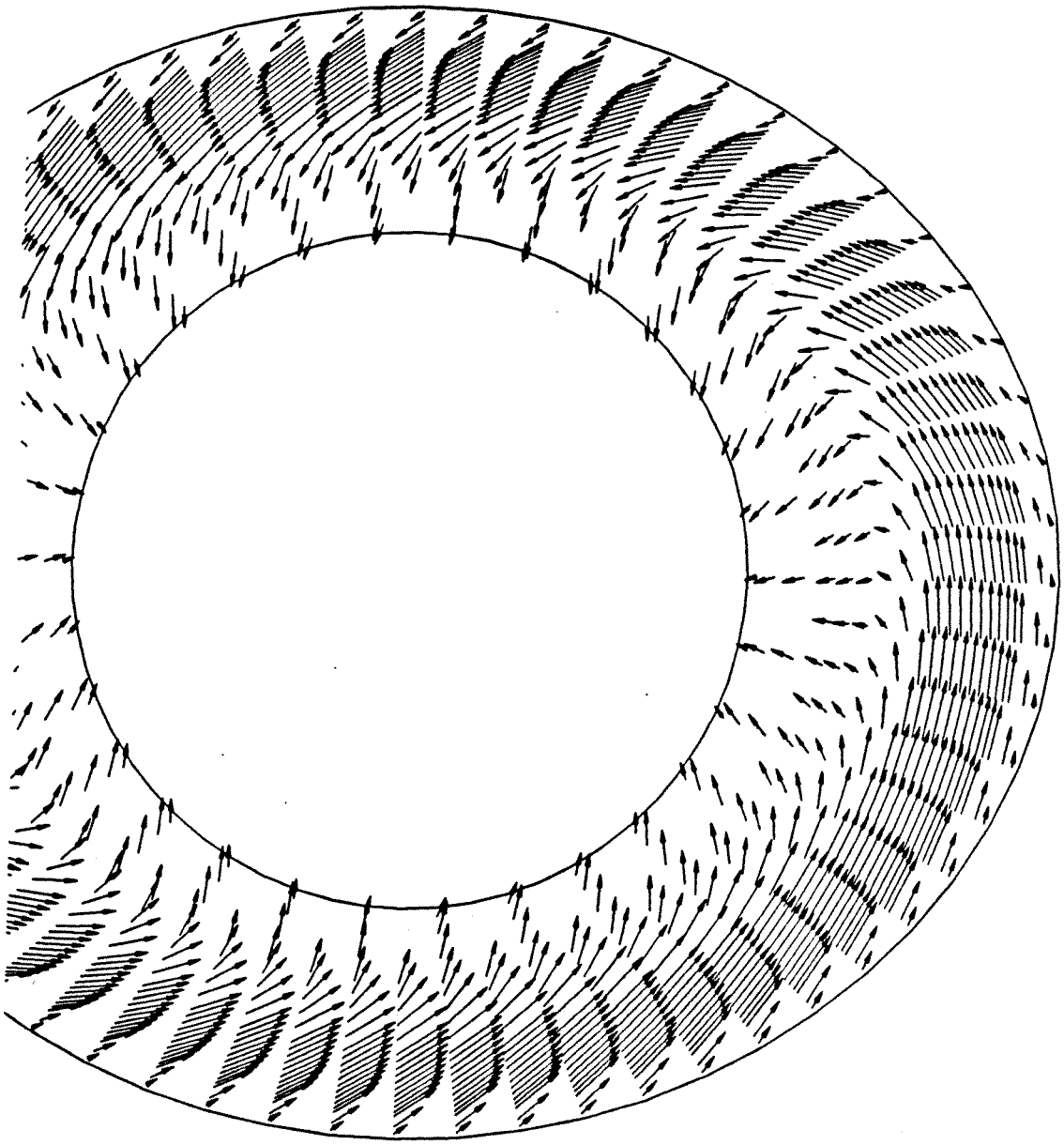

Figure 5.39: Cross–flow Velocity at Station 14, Split Blade Case

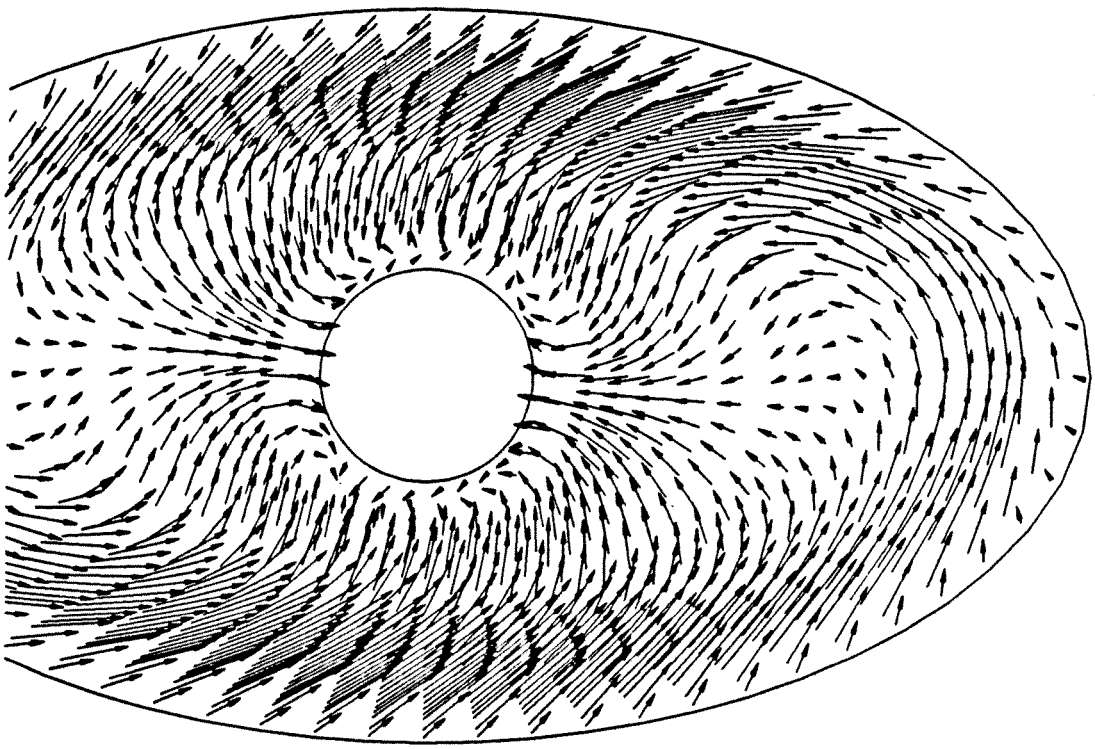

Figure 5.40: Cross–flow Velocity at Station 20, Split Blade Case

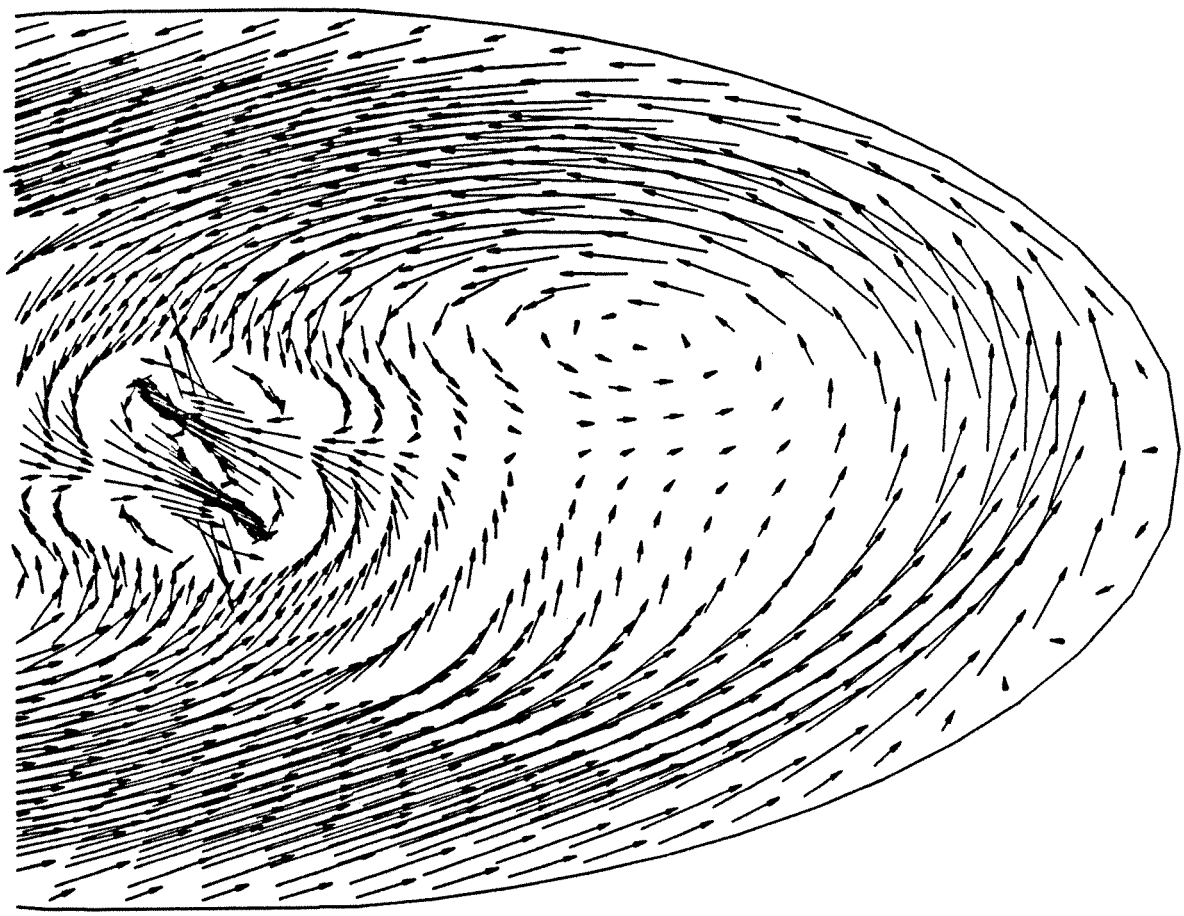

Figure 5.41: Cross–flow Velocity at Station 24, Split Blade Case

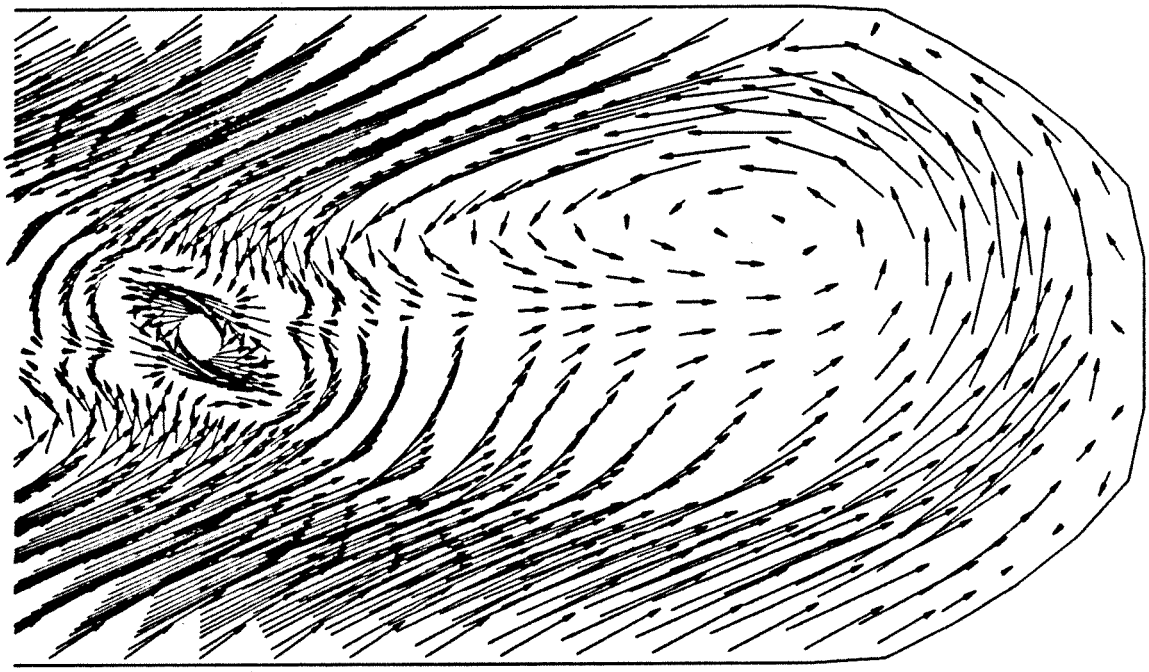

Figure 5.42: Cross-flow Velocity at Station 28, Split Blade Case

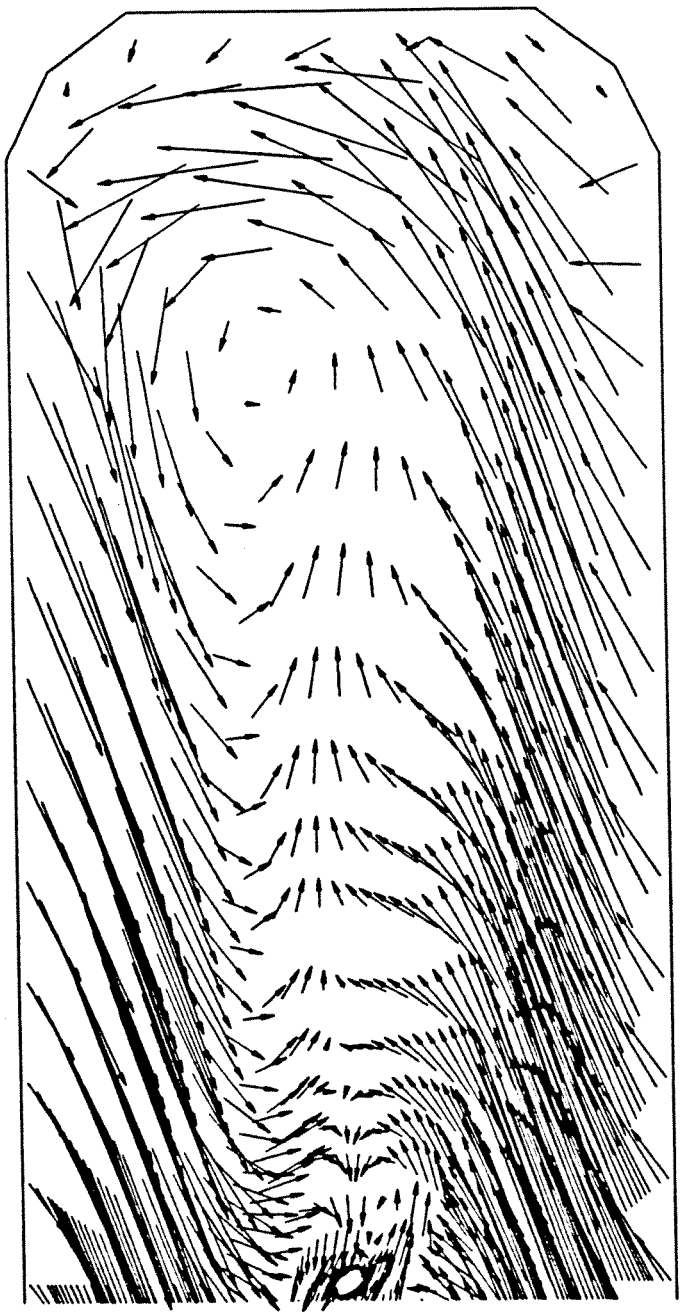

Figure 5.43: Cross-flow Velocity at Station 32, Split Blade Case

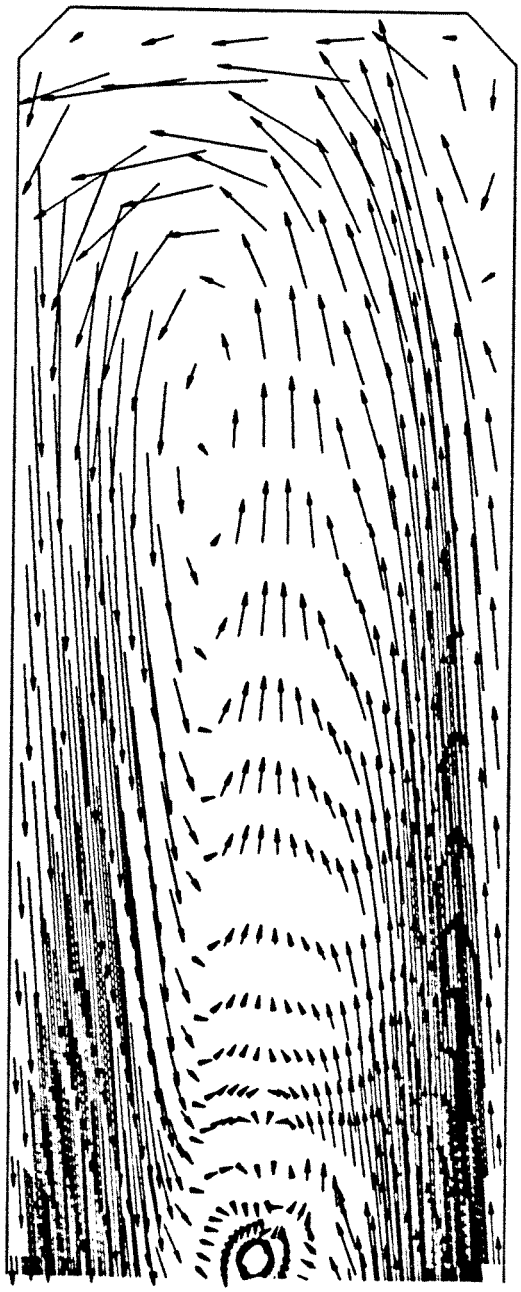

Figure 5.44: Cross–flow Velocity at Station 38, Split Blade Case

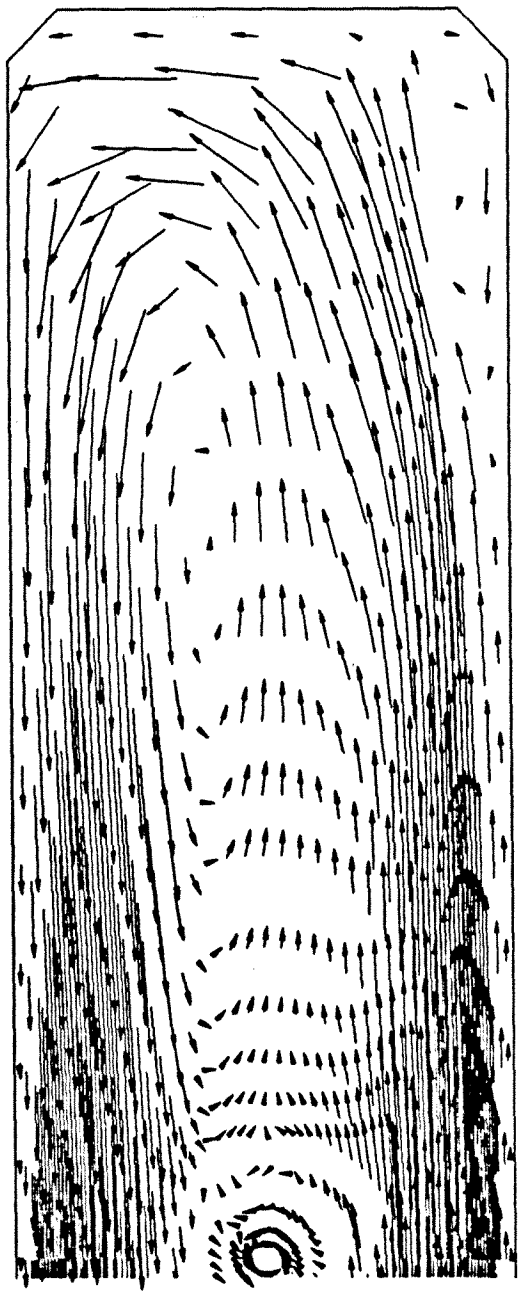

Figure 5.45: Cross-flow Velocity at Station 44, Split Blade Case

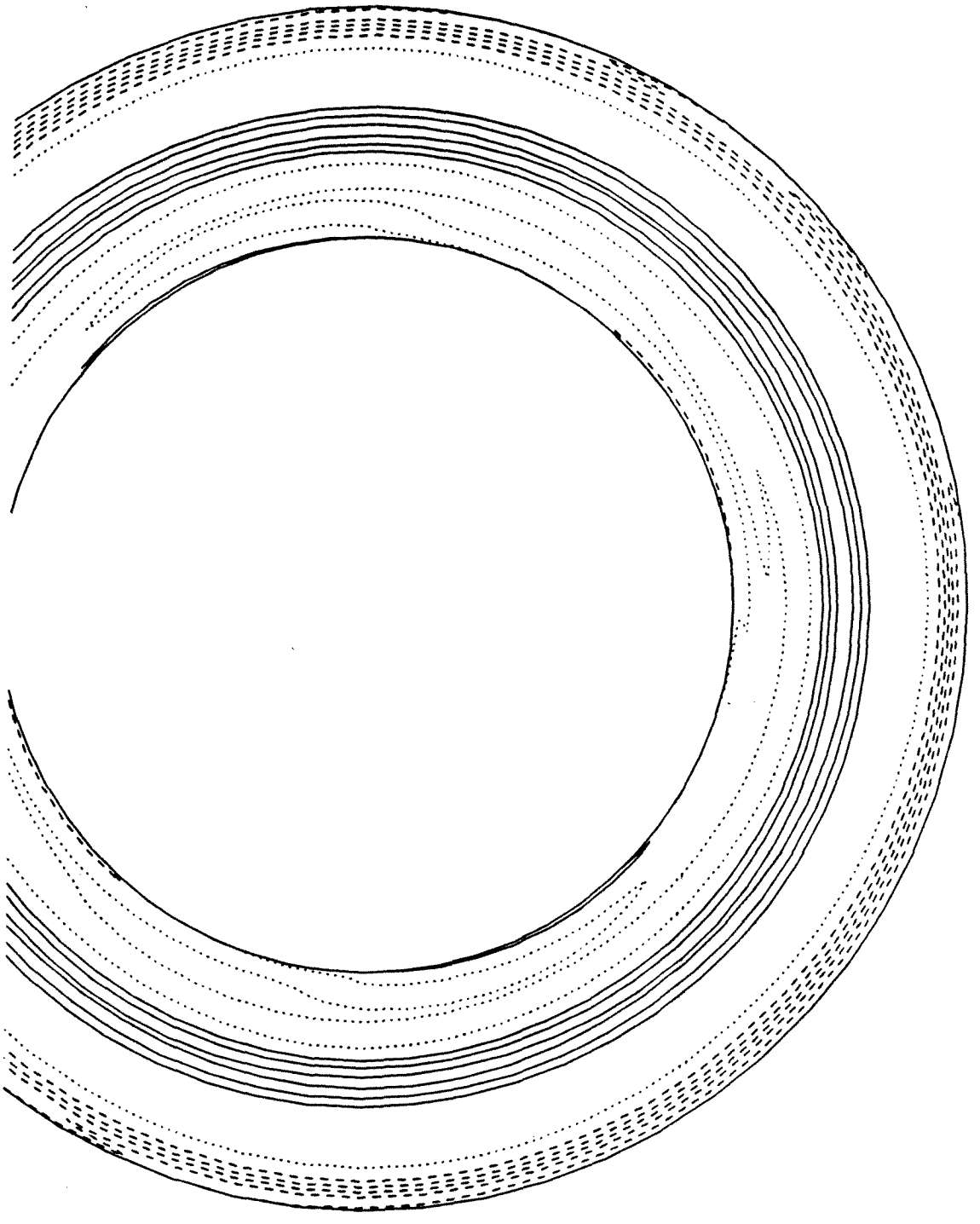

Figure 5.46: Axial Vorticity Contours at Station 6, Split Blade Case

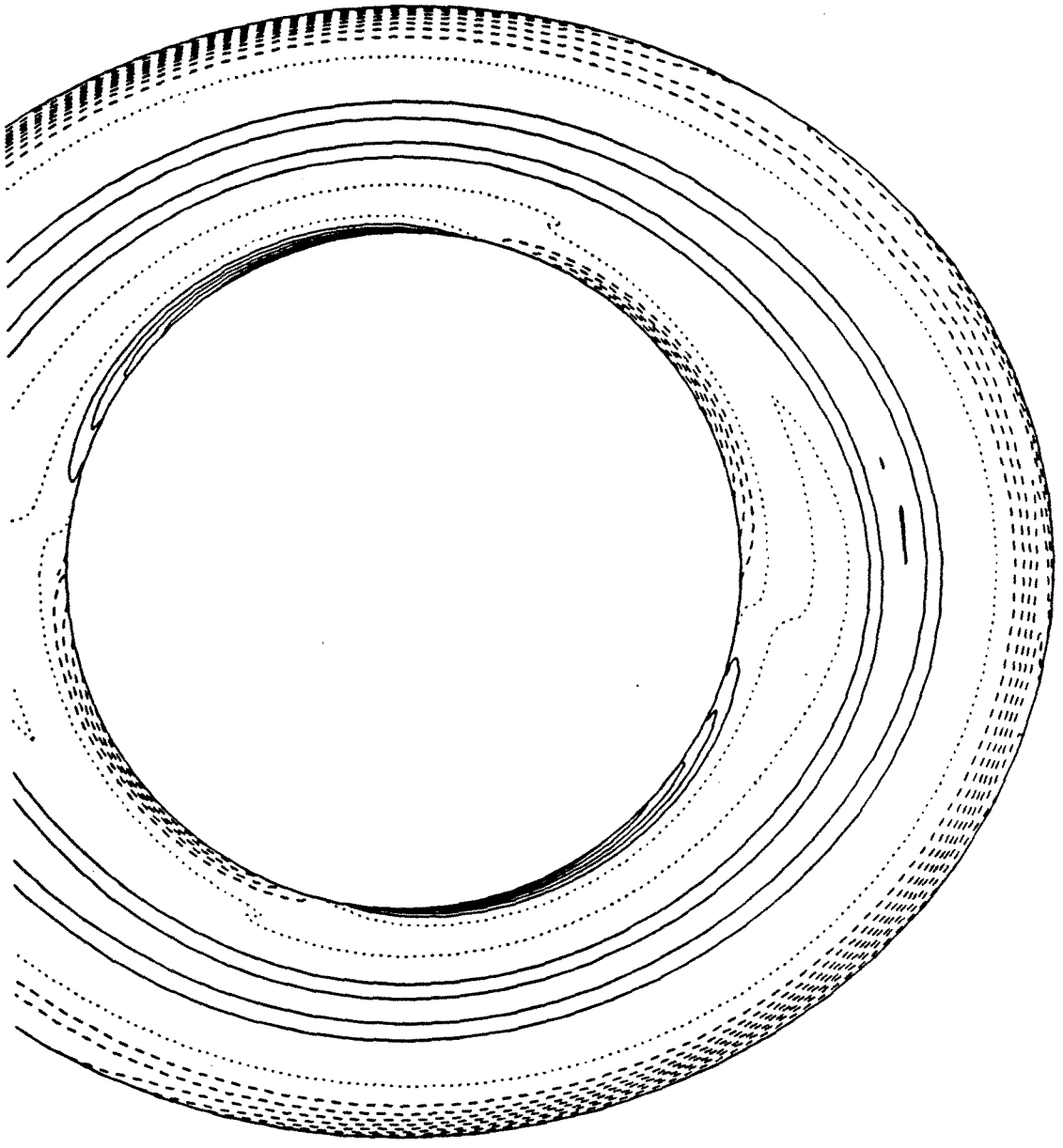

Figure 5.47: Axial Vorticity Contours at Station 14, Split Blade Case

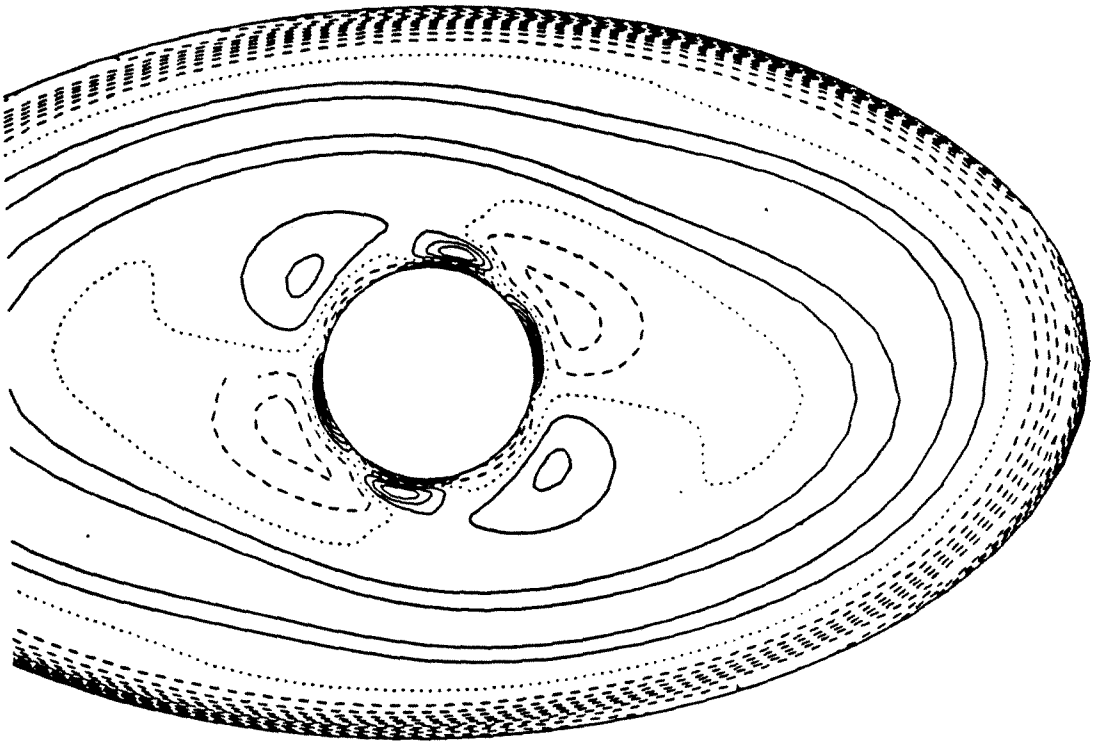

Figure 5.48: Axial Vorticity Contours at Station 20, Split Blade Case

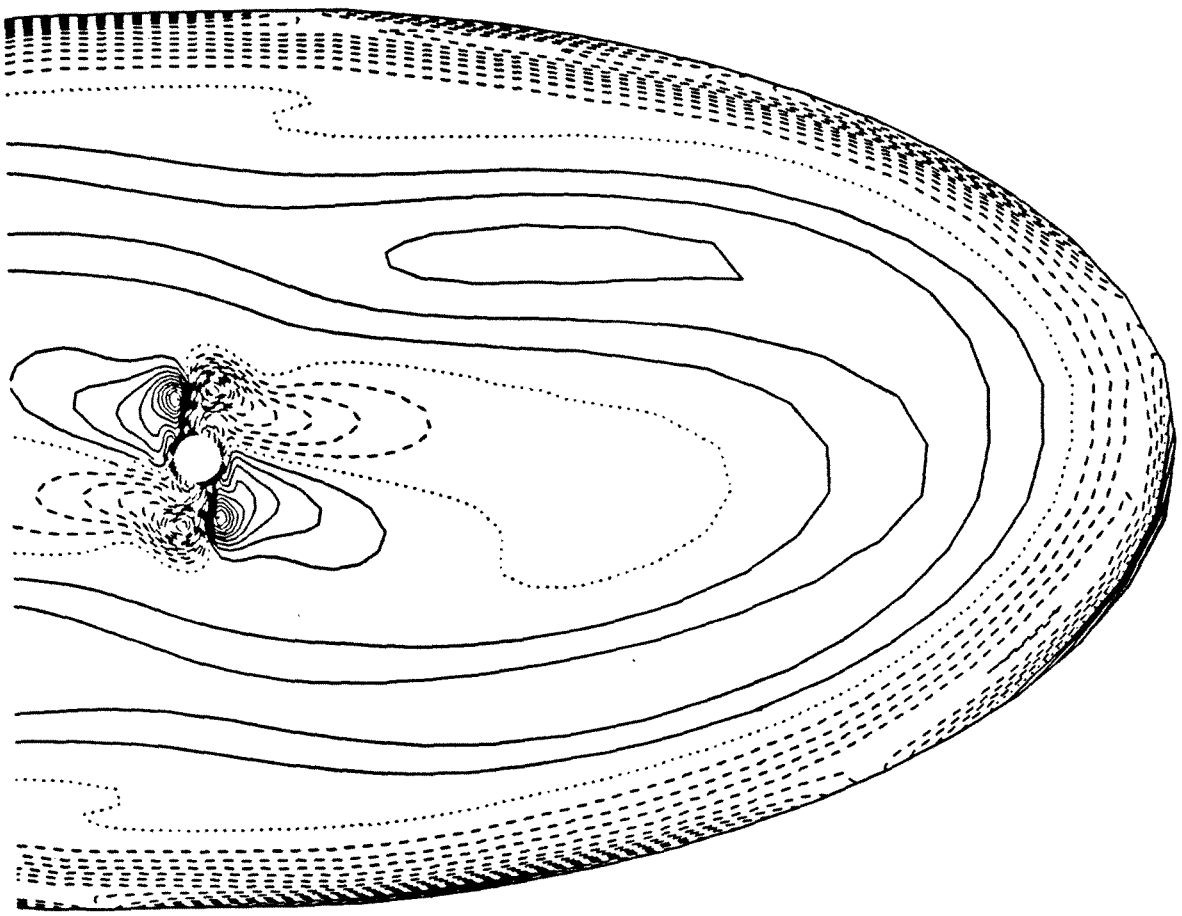

Figure 5.49: Axial Vorticity Contours at Station 24, Split Blade Case

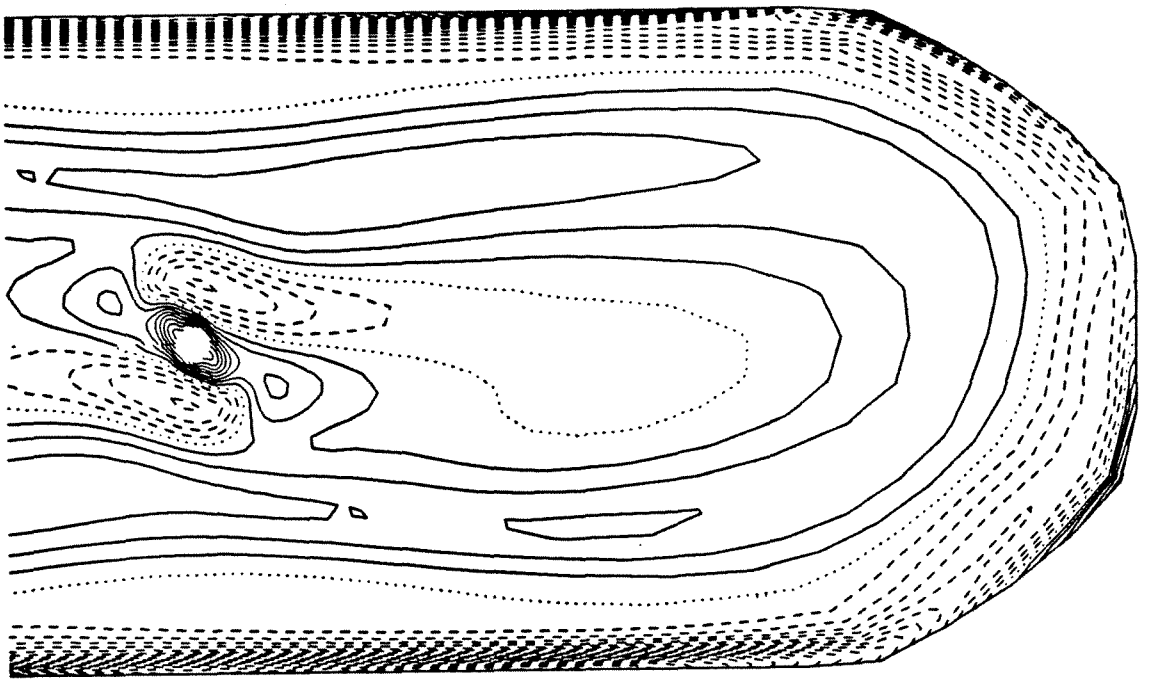

Figure 5.50: Axial Vorticity Contours at Station 28, Split Blade Case

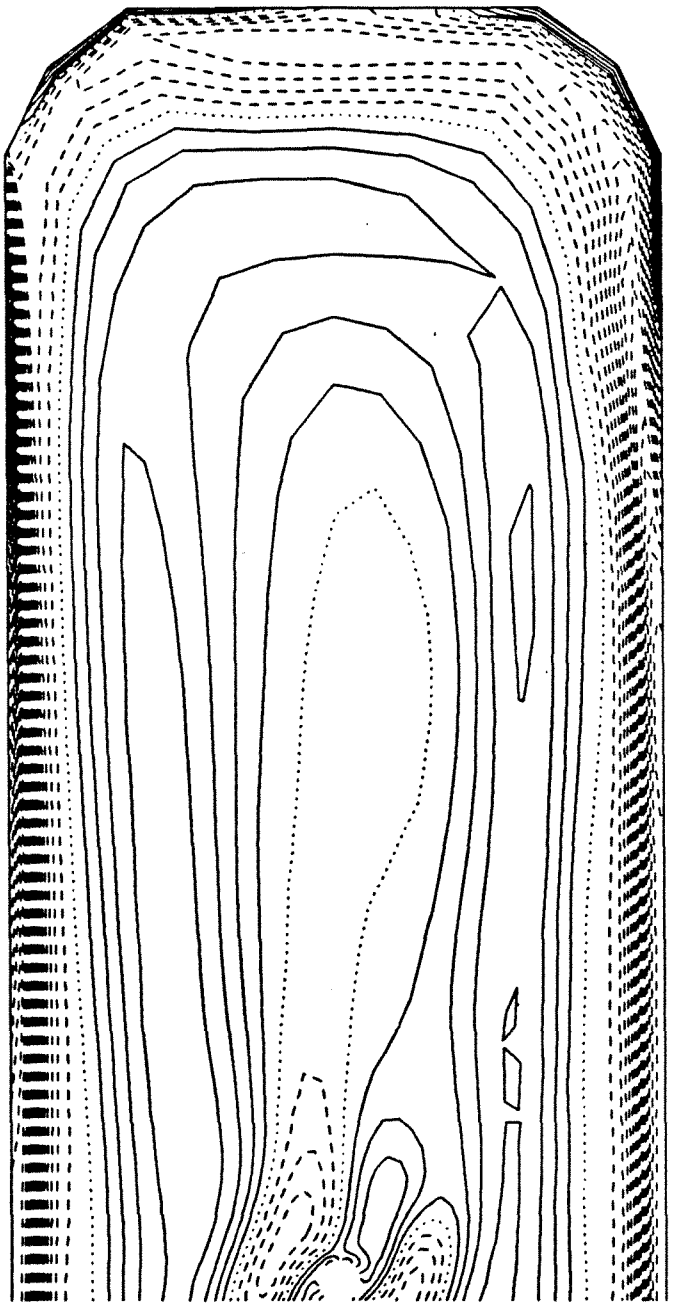

Figure 5.51: Axial Vorticity Contours at Station 32, Split Blade Case

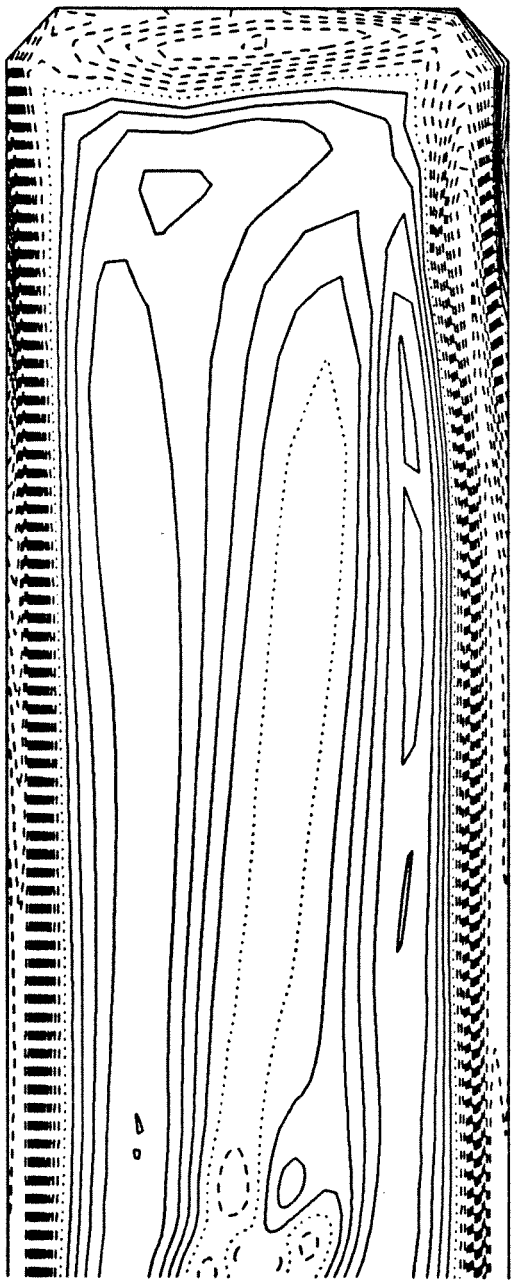

Figure 5.52: Axial Vorticity Contours at Station 38, Split Blade Case

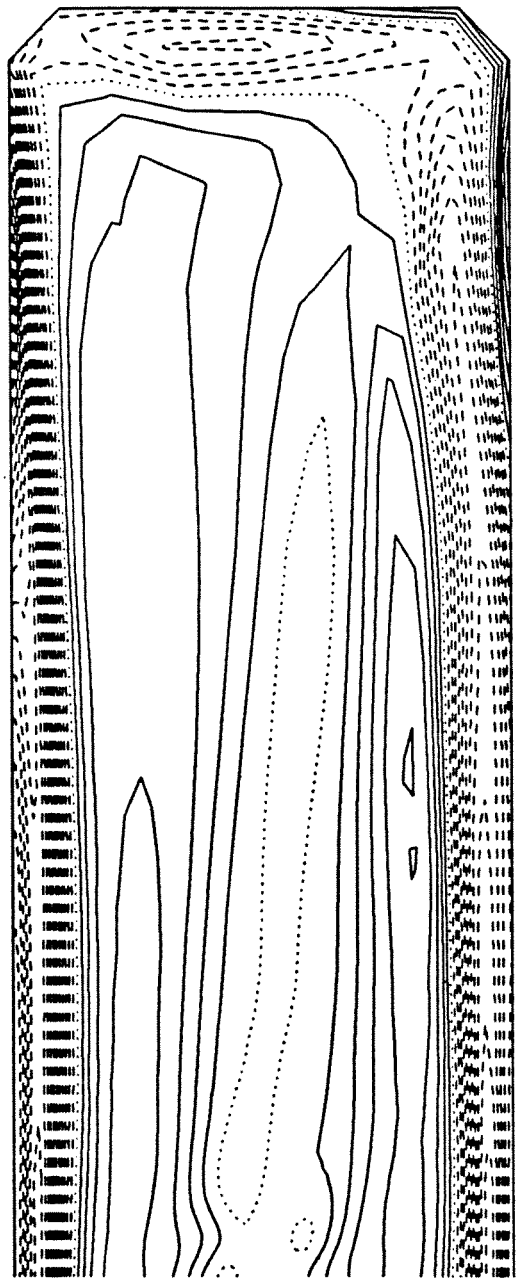

Figure 5.58: Axial Vorticity Contours at Station 44, Split Blade Case

Chapter 6

Conclusions and Concluding Remarks

A controlled investigation was undertaken to determine the effects of swirl on the flowfield that develops in an annular to rectangular transition section. The flow patterns at the exit were found to depend strongly on the distribution of axial vorticity at the annular inlet. The use of a steady laminar incompressible Navier–Stokes algorithm on a digital computer was found to adequately model the qualitative features of the flowfield. The experimental and numerical investigation was conducted with four different inlet conditions.

The no swirl case led to the formation of four weak, streamwise vortices at the exit plane. A careful examination of the developing flowfield showed that this was the result of the formation of streamwise vorticity in the boundary layer on the centerbody and the subsequent separation of this boundary layer into the stream. Because the formation of the streamwise vorticity was a direct result of the shape of the centerbody and outer wall of the flow system, and because this geometry does not model, exactly, the flow system that was the motivation for this work, this case is of interest largely as a baseline for other cases. The numerical results also indicate the formation of a complex three–dimensional separated region on the aft tip of the centerbody. The computational grid was not fine enough in the neighborhood of this separation to examine it in detail.

In the low and high swirl cases the majority of the vorticity was introduced in the neighborhood of the blade root and the blade tip in the boundary layers on the centerbody and outer wall, respectively. The axial vorticity introduced at the blade root was convected along the centerbody to the downstream tip and then along the centerline of the transition section. This resulted in the formation of a strong vortex along the central axis of the duct. The pressure gradient established on the outer wall of the duct, as a result of the strong central vortex, promoted the separation of the boundary layer from the outer wall into the main stream. This separation was evident in the formation of two streamwise vortices, one on each side of the central vortex, which had a sense opposite to the sense of the central vortex. This effect was much more pronounced in the high swirl case, as the pair of vortices formed was much stronger and moved nearly to the center of the height of the rectangular exit. It was argued that the maximum strength of these two vortices could be related to the strength of the central vortex and that the maximum strength was nearly achieved in the high swirl case.

In a fourth test case, a set of blades that introduced swirl into only the outer half of the inlet annulus was used. This, in effect, introduced a cylindrical sheet of streamwise vorticity into the flow at the inlet at a radial position halfway between the centerbody and the outer wall. There was also axial vorticity of the opposite sense introduced into the boundary layer on the outer wall. In this case the separation of the boundary layer on the outer wall did not occur to a significant extent but was apparent in the formation of two small, streamwise vortices in diagonally opposed corners of the rectangular exit cross section. The cylindrical vortex sheet, when convected through the annular to rectangular transition section, was distorted in such a way as to conform to the shape of the outer wall

of the duct. In the regions where the vortex sheet was most distorted, it tended to roll up. The result was the formation of two axial streamwise vortices at the exit plane of the duct.

The effect of swirl on the nearfield mixing of the jet issuing from the rectangular nozzle was not investigated. However, an examination of the vortex patterns leads one to conjecture on the relative effectiveness of these patterns in enhancing the nearfield mixing. The no swirl case is of little practical interest for two reasons. First, the features of the geometry that caused the formation of the four streamwise vortices are not present in the practical problem. Second, the strength of these vortices was very small and their effect on the mixing of the plume will, in all likelihood, be negligible.

The two axial vortices formed when swirl was introduced into only the outer half of the inlet annulus will, in all likelihood, enhance the nearfield mixing of the resulting jet. The combination of shear in the direction normal to the direction in which the jet forms and possibly an increase in large–scale entrainment due to the vortex pattern would serve to reduce the potential core size.

The vortex patterns created in the low and high swirl cases appear to be highly conducive to the mixing of the rectangular jet, particularly in the high swirl case. The adjacent positioning of strong vortices of opposite sense will tend to draw the cold ambient fluid between them. This large–scale mixing will rapidly reduce the size of the potential core region of the jet.

The discussion above, pertaining to mixing of the rectangular jet, is conjecture based on observation of the the flow patterns at the exit of the transition section. In order to accurately determine the mixing field in the region immediately behind the nozzle exit, it is suggested that a separate investigation be

undertaken.

If it is the nozzle designer's intent to create a flowfield that enhances mixing, he, of course, is not limited to the vorticity distributions examined in this investigation. The possibility of varying the vorticity distribution at the annular inlet to the transition section for the purpose of tailoring the vortex pattern at the exit is worth consideration. The distribution of axial vorticity at the inlet could be varied not only in the radial direction, but also in the tangential direction. A non-axi-symmetric distribution of vorticity at the inlet could be used to place vorticity and encourage the formation of axial vortices at any location in the exit. The other possibility for tailoring the flowfield involves contouring the duct shape so as to promote either the separation of the boundary layers on the outer wall or the formation of streamwise vortices from vorticity distributed throughout the flow. The current investigation provides an understanding of the mechanisms by which the streamwise vortices are formed. This understanding is valuable in any effort to tailor the flow, whatever the intended purpose.

References

[1] McLafferty, G. H. and Peterson, J. L., "Results of Tests of a Rectangular Vectoring/Reversing Nozzle on an F100 Engine," in *AIAA/SAE/ASME 19th Joint Propulsion Conference*, June 1983. AIAA–83-1285.

[2] Gowadia, N. S., Bard, W. D., and Wooten, W. H., "YF–17/ADEN System Study," Contractor Report CR-144882, NASA, July 1979.

[3] Wooten, W. H., Blozy, J. T., Speir, D. W., and Lottig, R. A., "Altitude Testing of a Flight Weight, Self Cooled, 2D Thrust Vectoring Exhaust Nozzle," in *Aerospace Congress and Exposition*, October 1984. SAE–841557.

[4] Sforza, P. M., Steiger, M. H., and Trentacoste, N., "Studies on Three–Dimensional Viscous Jets," *AIAA Journal*, vol. 4, no. 5, pp. 800–806, 1966.

[5] Sforza, P. M. and Stasi, W., "Heated Three–Dimensional Turbulent Jets," *Journal of Heat Transfer*, vol. 101, no. 2, pp. 353–358, 1979.

[6] Decher, R., "Infrared Emissions from Turbofans with High Aspect Ratio Nozzles," *Journal of Aircraft*, vol. 18, pp. 1025–1031, December 1981.

[7] Chu, C., Der Jr., J., Ortiz, V. M., and Widynski, T. C., "Effect of Swirl on the Potential Core of Two–Dimensional Ejector Nozzles," *Journal of Aircraft*, pp. 191–192, February 1983.

[8] Der Jr., J., Chu, C., Hunt, B. L., and Lorincz, D. J., "Evolution of Swirl in a Two–Dimensional–Nozzle Flow," *Journal of Aircraft*, vol. 19, pp. 347–349, April 1982.

[9] Chu, C., Der Jr., J., and Wun, W., "A Simple 2D Nozzle Plume for IR Analysis," in *AIAA Aircraft Systems Meeting*, August 1980. AIAA–80-1808.

[10] Chu, C. and Der Jr., J., "Modeling of 2D Nozzle Plume for IR Signature Predictions Under Static Conditions," in *AIAA Aircraft Systems Meeting*, August 1980. AIAA–80-1808.

[11] Horlock, J. H. and Lakshminarayana, B., "Secondary Flows: Theory, Experiment, and Application in Turbomachinery Aerodynamics," *Annual Review of Fluid Mechanics*, vol. 5, pp. 247–279, 1973.

[12] Squire, H. B. and Winter, K. G., "The Secondary Flow in a Cascade of Airfoils in a Nonuniform Stream," *Journal of the Aeronautical Sciences*, vol. 18, pp. 271–277, April 1951.

[13] Hawthorne, W. R., "Secondary Circulation In Fuid Flow," *Proceedings of the Royal Society of London*, vol. 206, pp. 374–386, May 1951.

[14] Lighthill, M. J., "Drift," *Journal of Fluid Mechanics*, vol. 1, pp. 31–53, 1956.

[15] Nosenchuck, D. M., *Passive and Active Control of Boundary Layer Transition.* PhD thesis, California Institute of Technology, Pasadena, California, 1982.

[16] King, L. V., "On the Convection of Heat from Small Cylinders in a Stream of Fluid: Determination of the Convection Constants of Small Platinum Wires

with Application to Hot–Wire Anemometry," *Proc. R. Soc. Lond.*, vol. 47, pp. 563–570, 1914.

[17] Perry, A. E., *Hot-wire Anemometry.* New York: Oxford University Press, 1982.

[18] Kwak, D., Chang, J. L. C., Shanks, S. P., and Chakravarthy, S. R., "An Incompressible Navier–Stokes Flow Solver in Three–Dimensional Curvilinear Coordinate System Using Primitive Variables," in *AIAA 22th Aerospace Sciences Meetin*, January 1984. AIAA–84-0253.

[19] Chorin, A. J., "A Numerical Method for Solving Incompressible Viscous Flow Problems," *Journal of Computational Physics*, vol. 2, pp. 12–26, 1967.

[20] Beam, R. M. and Warming, R. F., "An Implicit Finite Difference Algorithm For Hyperbolic Systems in Conservation Law Form," *Journal of Computational Physics*, vol. 22, pp. 87–110, September 1976.

[21] Chang, J. L. C., Kwak, D., Dao, S. C., and Rosen, R., "A Three–Dimensional Incompressible Flow Simulation Method and its Application to the Space Shuttle Main Engine, Part I — Laminar Flow," in *AIAA 23rd Aerospace Sciences Meeting*, January 1985. AIAA–85-0175.

[22] Chang, J. L. C., Kwak, D., Dao, S. C., and Rosen, R., "A Three–Dimensional Incompressible Flow Simulation Method and its Application to the Space Shuttle Main Engine, Part II — Turbulent Flow," in *AIAA 18th Fluid Dynamics and Plasmadynamics and Laser Conference*, July 1985. AIAA–85–1670.

[23] Chang, J. L. C. and Kwak, D., "On the Method of Pseudo Compressibility for Numerically Solving Incompressible Flows," in *AIAA 22nd Aerospace Sciences Meeting*, January 1984. AIAA–84-0252.

[24] Sorenson, R. L., "A Computer Program To Generate Two-dimensional Grids About Airfoils and Other Shapes By the Use of Poissoin's Equation," Tech. Rep. NASA TM-81198, 1981.

[25] Hornung, H. and Perry, E., "Some Aspects of Three-Dimensional Separation, Part I:Streamsurface Bifurcations," *Z. Flugwiss. Weltraumforsch.*, vol. 8, no. 2, pp. 77–87, 1984.

[26] Perry, E. and Hornung, H., "Some Aspects of Three-Dimensional Separation, Part II:Vortex Skeletons," *Z. Flugwiss. Weltraumforsch.*, vol. 8, no. 3, pp. 155–160, 1984.

[27] Lighthill, M. J., "Introduction. Boundary Layer Theory," in *Laminar Boundary Layers*, (Rosenhead, L., ed.), ch. 2, 1963.

[28] Batchelor, G. K., *An Introduction to Fluid Dynamics*, pp. 543–555. New York: Cambridge University Press, 1967.

[29] Chigier, N. A. and Chervinsky, A., "Experimental Investigation of Swirling Vortex Motion in Jets," *Journal of Applied Mechanics*, pp. 443–451, June 1967.

Appendix A

Uncertainty Estimate

As stated in chapter 3 the assumption that the flow is steady, for the purpose of velocity decompositon, introduces some uncertainty into the results. In order to account for the effect of the velocity fluctuations the equations for the velocity decomposition must be time averaged. Because the velocities were determined from two non–simultaneous sets of cross–wire probe measurements, the correlations necessary for an exact decomposition are not available. The velocity measurements were used to establish the existence of vortex patterns in the cross–flow velocity field. Therefore, the uncertainty in the results is best described as the uncertainty in the angle (α) of the cross–flow velocity vector;

$$\alpha = \arctan \frac{w}{u}$$

where w and v are the vertical and horizontal velocities, respectively. For the configuration used in this investigation these velocities are related to the velocities measured by the cross–wire probe as follows;

$$V_1(t)^2 = w^2 + \frac{1}{2}(u+v)^2$$

$$V_2(t)^2 = w^2 + \frac{1}{2}(u-v)^2$$

$$V_3(t)^2 = v^2 + \frac{1}{2}(u+w)^2$$

$$V_4(t)^2 = v^2 + \frac{1}{2}(u - w)^2.$$

The angle α can then be expressed as;

$$\alpha = \arctan \frac{V_3^2 - V_4^2}{V_1^2 - V_2^2}.$$

This relation holds only for the instantaneous values of V_i. To aid in time averaging these relations we express each velocity as the sum of the mean velocity $\overline{V}$ and the instantaneous fluctuation velocity V'. Define $\widehat{V_i}$ as;

$$\widehat{V_1} = [\overline{w}^2 + \frac{1}{2}(\overline{u} + \overline{v})^2]^{\frac{1}{2}}.$$

Then the time averaged α can be written;

$$\overline{\alpha} = \arctan \frac{\widehat{V_3}^2 - \widehat{V_4}^2}{\widehat{V_1}^2 - \widehat{V_2}^2}.$$

To obtain an estimate for the uncertainty we evaluate;

$$\overline{V_1^2} - \widehat{V_1}^2 = \overline{w'^2} + \frac{1}{2}(\overline{u'^2} + \overline{v'^2}) + \overline{u'v'}$$

$$\overline{V_2^2} - \widehat{V_2}^2 = \overline{w'^2} + \frac{1}{2}(\overline{u'^2} + \overline{v'^2}) - \overline{u'v'}$$

Subtracting gives;

$$\widehat{V_1}^2 - \widehat{V_2}^2 = \overline{V_1^2} - \overline{V_2^2} - 2\overline{u'v'}$$

A similar expression can be obtained using V_3 and V_4. The angle $(\overline{\alpha})$ can be written;

$$\overline{\alpha} = \arctan \frac{\overline{V_3^2} - \overline{V_4^2} - 2\overline{u'w'}}{\overline{V_1^2} - \overline{V_2^2} - 2\overline{u'v'}}.$$

Since we know from the experimental results the $\overline{V_i^2}$ but we do not know the correlations $\overline{u'v'}$ and $\overline{u'w'}$ we can calculate α assuming the correlations negligible and then estimate the uncertainty due to this assumption. The correlation coefficient C is commonly defined as;

$$C = \frac{|\overline{u'v'}|}{\sqrt{\overline{u'^2}\,\overline{v'^2}}}.$$

For a conservative estimate of the magnitude of $\overline{u'v'}$ we choose $C = 0.5$ and approximate the denominator of the above expression as the maximum of the $\overline{V_i'^2}$. So we calculate $\tilde{\alpha}$;

$$\tilde{\alpha} = \arctan \frac{\overline{V_3^2} - \overline{V_4^2}}{\overline{V_1^2} - \overline{V_2^2}}.$$

Then the uncertainty in $\tilde{\alpha}$ is given by;

$$\text{uncertainty} = \tilde{\alpha} - \arctan \frac{\overline{V_3^2} - \overline{V_4^2} + |2\overline{u'w'}|}{\overline{V_1^2} - \overline{V_2^2} - |2\overline{u'v'}|}.$$

These uncertainties were computed for all four experimental cases and are shown in Figures A.1–A.4.

Finally, a comparison between the angles as computed for the purpose of plotting the cross–flow velocity vectors and $\tilde{\alpha}$ is necessary to demonstrate that both relations give nearly equal results. For the purpose of plotting the the cross-flow velocity vectors the angle was computed as follows;

$$\check{\alpha} = \arctan \frac{\overline{V_3}^2 - \overline{V_4}^2}{\overline{V_1}^2 - \overline{V_2}^2}.$$

Figures A.5–A.8 show Δ for all four experimental cases, where;

$$\Delta = |\tilde{\alpha} - \check{\alpha}|.$$

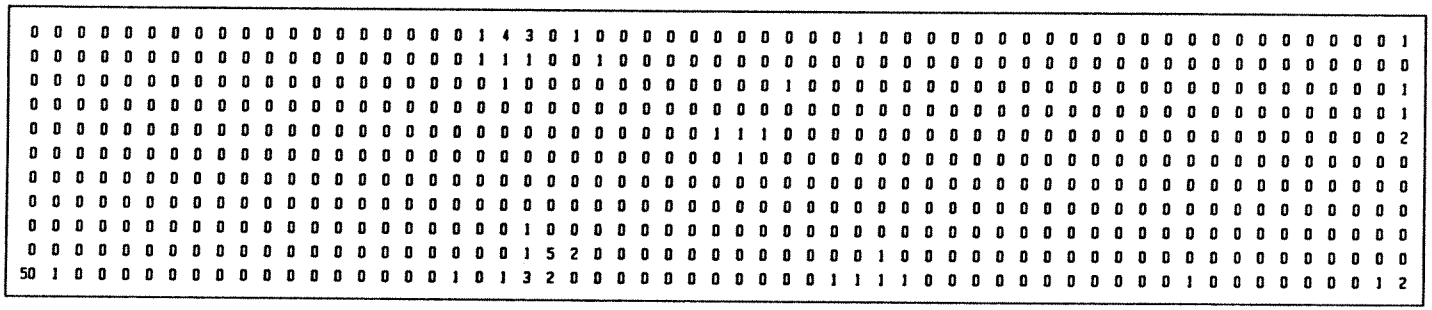

Figure A.1: Uncertainty (in Degrees) of $\hat{\alpha}$, No Swirl Case

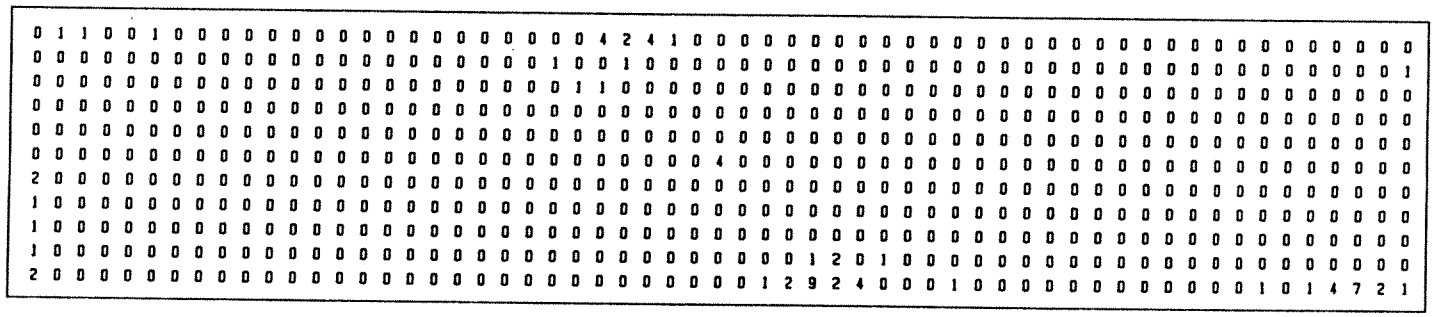

Figure A.2: Uncertainty (in Degrees) of $\hat{\alpha}$, Low Swirl Case

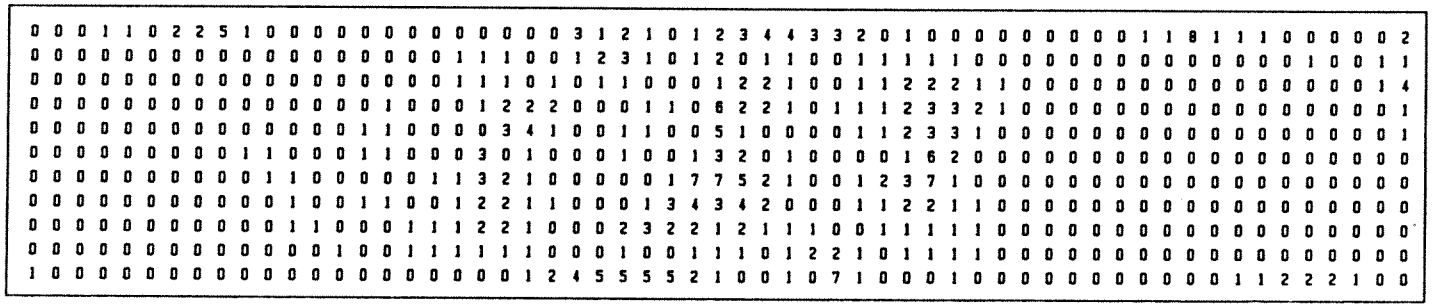

Figure A.3: Uncertainty (in Degrees) of $\hat{\alpha}$, High Swirl Case

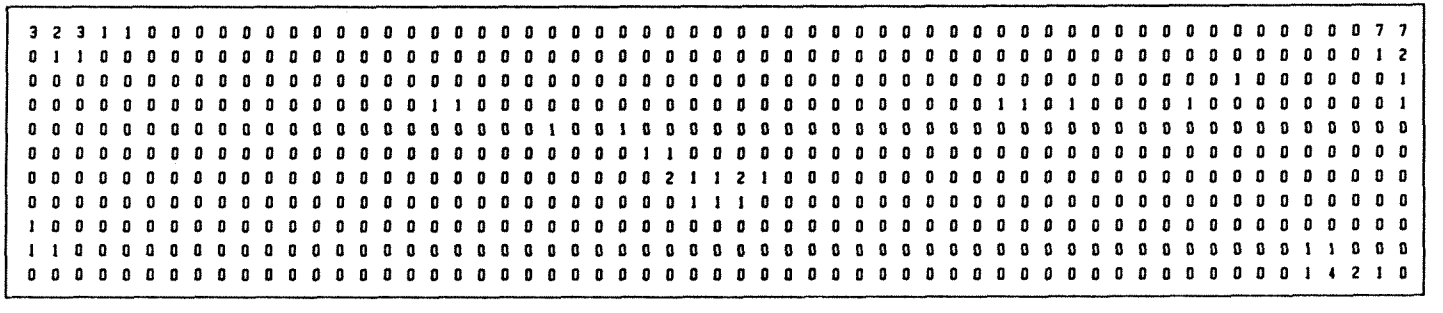

Figure A.4: Uncertainty (in Degrees) of $\hat{\alpha}$, Half Height Blade Case

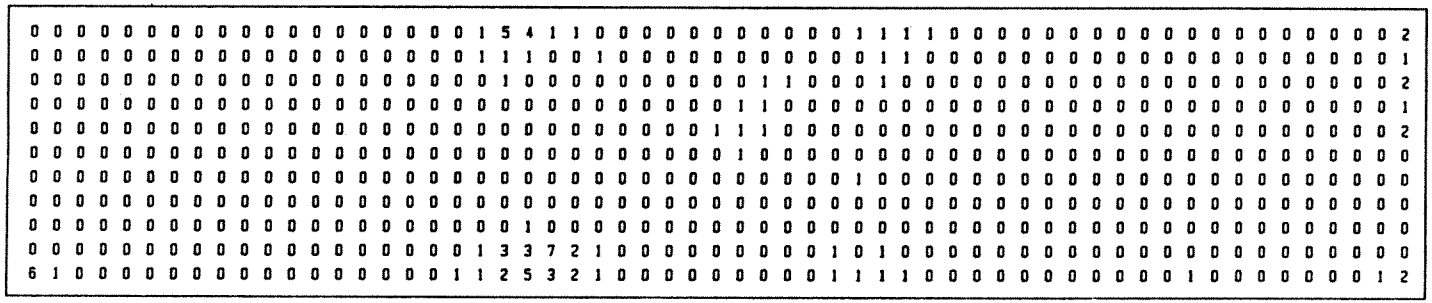

Figure A.5: Δ (in Degrees), No Swirl Case

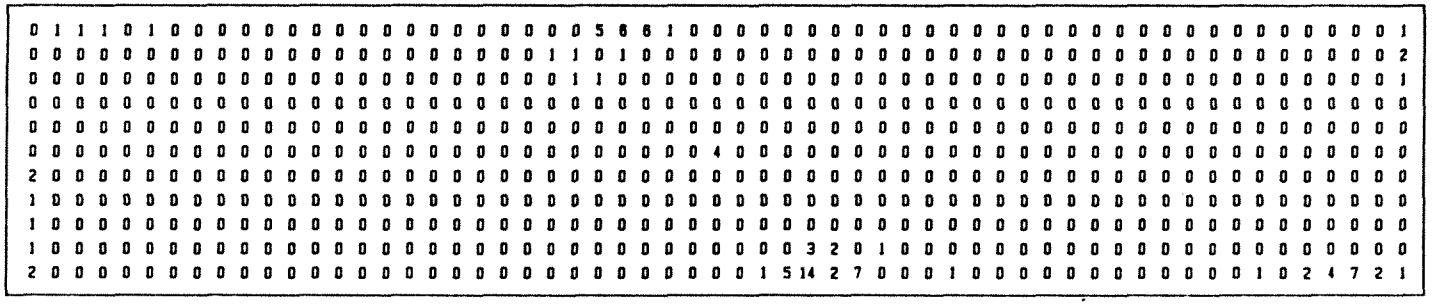

Figure A.6: Δ (in Degrees), Low Swirl Case

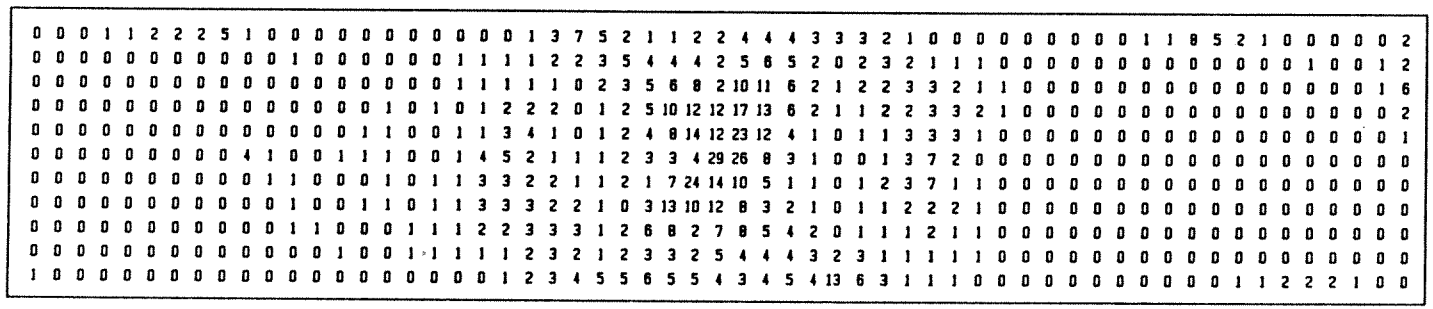

Figure A.7: Δ (in Degrees), High Swirl Case

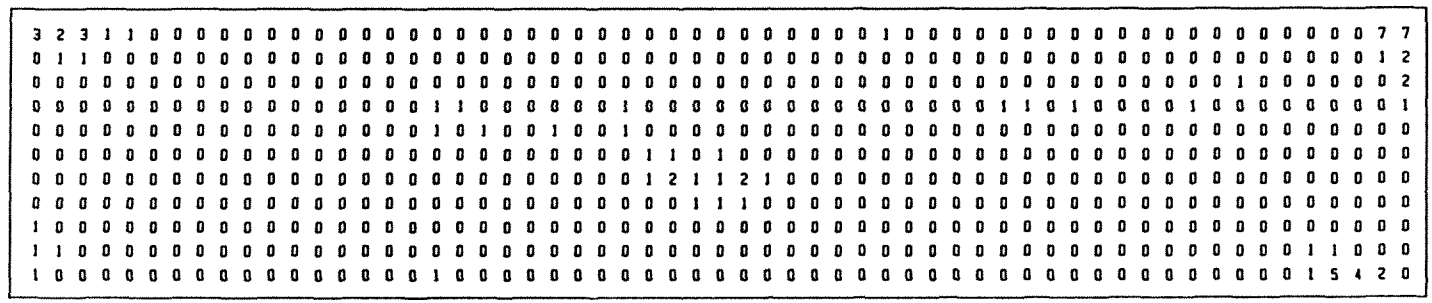

Figure A.8: Δ (in Degrees), Half Height Blade Case